Optical spectroscopy of high-lying excitons in low-dimensional semiconductors

DISSERTATION ZUR ERLANGUNG DES DOKTORGRADES
DER NATURWISSENSCHAFTEN (DR. RER. NAT.)
DER FAKULTÄT FÜR PHYSIK
DER UNIVERSITÄT REGENSBURG

vorgelegt von

Jonas Maria Bauer
aus Regensburg
im Jahr 2025

Promotionsgesuch eingereicht am: 05.11.2025
Die Arbeit wurde angeleitet von: Prof. Dr. John M. Lupton

Contents

CHAPTER 1

Introduction

And God said, "Let there be light," and there was light. And God saw that the light was good.

Genesis 1:3-4 [1]

From ancient creation stories on, light has always been a source of fascination and inspiration for humanity. In a biblical sense, light is the beginning of everything. It has been associated with knowledge, enlightenment and the divine [2–4]. In modern science, light is not seen metaphorically as a myth but plays a crucial role in our understanding of the universe, from the study of distant galaxies [5] to the exploration of the tiniest particles [6].

The interaction between light and matter is a fundamental aspect in modern physics, especially in the field of condensed matter physics, offering a powerful tool to investigate the quantum nature of the material [7]. Ranging from early studies of atomic spectra [8] to the development of state-of-the-

art LEDs, lasers, computer chips, detectors, light-harvesting devices and quantum optics [9–11], light-matter interaction has revealed the behavior of electrons, phonons and other quasiparticles in solids, and certainly will play a crucial role in future computational devices, for example, in the field of quantum computing, using the spin of the carrier, or optical computers [12–21].

Among the most intriguing manifestations of light-matter interaction are excitons, bound electron-hole pairs that are generated when a material absorbs a photon [22–25]. Excitonic properties can be widely tuned and provide a versatile platform for optoelectronic devices [26, 27]. In order to use excitons in applications, they require high mobility and large binding energies, i.e., stability at room temperature. Inorganic materials like GaAs exhibit high mobility but low binding energies [28, 29], while organic materials show high binding energies but low mobility [30–32]. Two-dimensional transition metal dichalcogenides (TMDCs) provide a good compromise between these two. The material's properties are highly influenced by their reduced dimensionality, leading to high binding energies while keeping high mobility [33–38].

The successful demonstration of monolayer graphene started the research on atomically thin layers and made it a vibrant field of study [39–43]. While layered materials, fabricated by means of molecular beam epitaxy, have been studied for a long time [44–46], restrictions concerning the material combinations remain. The isolation of two-dimensional materials breaks this limitation and opens endless combinations, independent of the lattice constant [47–50]. The materials can be fabricated and tailored to the desired properties by easy mechanical exfoliation, using commercially available Scotch tape [51–57]. This low barrier of entry makes the field accessible to many research groups.

The possibility of fabricating structures of different materials, without restrictions on the twist angle, led to the discovery of moiré excitons [58–64].

The rapid increase in sample quality and extensive studies led to fascinating discoveries like Wigner crystals [65–68]. Twisted structures of monolayers, obtaining large moiré cells, can serve as a platform to investigate correlated many-body physics and unconventional superconductivity [69–81]. By bringing two different semiconducting materials in close proximity, interlayer excitons can be formed, where electrons and holes are spatially separated in different layers. Due to the alignment of Fermi energies at the interfaces of the materials, their electronic bands exhibit a shift. Depending on the position of the Fermi energy interlayer excitons can form in different types of band alignment. As the charge carrier wavefunctions have reduced overlap, the lifetime of interlayer excitons usually exceeds the lifetime of intralayer excitons [82–91].

Due to their low-dimensional nature, TMDCs are highly sensitive to their dielectric environment, which can be used to control their properties [92–97], or to sense physical quantities in materials which are in close proximity [98].

This thesis explores a newly discovered unique class of excitons, originating from states far above the band gap of semiconducting TMDCs, referred to as high-lying excitons (HX). Traces of these excitons are investigated by linear and nonlinear spectroscopy. A bright s-like species is investigated by means of upconversion photoluminescence (UPL). Additionally, a dark p-like HX is measured with nonlinear processes. The thesis is structured as follows: In chapter 2 the theoretical foundations of low-dimensional materials and excitonic complexes are introduced, followed by a brief overview of nonlinear optical spectroscopy techniques. This includes the parametric and non-parametric regimes of nonlinear optics, where the latter is described by density-matrix formalism. Next, a review of the already established physical properties of HXs is given. The influence of excitonic resonances on optical properties is highlighted, with a focus on the power-law exponent of second-harmonic generation and the influence of spectral phase on quantum interference phenomena.

In chapter 3 the experimental setup and measurement techniques used in this work are introduced. This includes a description of photoluminescence (PL) measurements, UPL measurements, nonlinear optical experiments using one laser wavelength to investigate the second-harmonic generation (SHG), and nonlinear optical experiments using two different colored lasers, investigating sum-frequency generation (SFG) and four-wave mixing (FWM). Finally, a setup to control and measure the chirp introduced to one laser pulse is presented.

Next, the experimental results are presented in chapter 4. The first part focuses on the energetic landscape of HXs. This includes the investigation of the influence of chirped laser excitations on the nonlinear optical response of WSe_2. In order to display HXs as a general feature of semiconducting TMDC monolayers, we investigate their traces by various optical spectroscopy techniques in different materials.

The second part investigates the temporal dynamics of HXs. The lifetime of p-like HX in WSe_2 is investigated by means of SFG and FWM. Additionally, the temporal dynamics of s-like HX in WSe_2 are measured using a streak camera.

Finally, a conclusion is drawn in chapter 5 and future perspectives are discussed. An appendix with additional information is provided at the end of this thesis.

CHAPTER 2

Theoretical foundations

Over the last years, layered materials have gained a lot of attention in the scientific community. The ability to reduce the dimensionality of materials down to a single layer, has led to a new field of research, as the properties of materials change drastically with the number of layers [40]. The most prominent example is the semimetal graphene, a single layer of carbon atoms arranged in a honeycomb lattice. The material shows extraordinary properties like high electrical conductivity, high thermal conductivity and high mechanical strength [39, 40, 42]. Over the last 20 years a diverse family of layered materials has been discovered. Including insulators like hexagonal boron nitride (hBN), superconductors like niobium diselenide ($NbSe_2$), metals like titanium disulfide (TiS_2) [99], magnetic materials like chromium triiodide (CrI_3) [100], topological insulators like Bi_2Te_3 [99],and semiconductors like black phosphorous (BP) [101] or transition metal dichalcogenides (TMDCs) [102]. Many different approaches to fabricate layered materials have been developed, including chemical deposition techniques or dry mechanical exfoliation. The latter uses the intriguing property of weak van-der-Waals (vdW) interactions

between layers of the material, that are formed by covalent bonds, making it possible to separate the layers from each other by finite forces. While two-dimensional materials themselves already show interesting properties, nearly unlimited possibilities can be explored by stacking different materials on top of each other and using the vdW force to form heterostructures and create new materials with tailored properties [48, 103–108].

In this work, we investigate the physical properties of semiconducting TMDCs. Therefore, some of their key properties will be discussed in the following sections.

2.1 Transition metal dichalcogenides

The electrical, optical and mechanical properties of bulk TMDCs have been extensively studied since the 1960s, when their layered character was already known and used [109–112]. The synthesis of few-layer TMDCs sparked a new research area in the field, making it particularly interesting because of their semiconducting properties. In order to understand physical effects in this material class, the general crystal structure, the electronic band structure and the resulting excitonic species will be discussed in the following sections.

2.1.1 Crystal structure

Semiconducting TMDCs are characterized by their layered structure. Each layer consists of one transition metal from group 6 of the periodic table, generally referred to as M, sandwiched between two layers of chalcogen atoms from group 16 of the periodic table, generally referred to as X. The general formula is MX_2. A side view of the atomic arrangement within one layer is shown in fig. 2.1**a**, with transition metals shown in black and chalcogen atoms shown in yellow. The layer of transition metal atoms is shifted with respect to the chalcogen atoms, forming a trigonal prismatic orientation, as schematically depicted in fig. 2.1**b**. The top view of a TMDC monolayer

reveals a triangular lattice with a basis of two atoms per unit cell, resulting in a hexagonal honeycomb structure of the crystal. The most common semiconducting TMDCs are composed of M=Mo, W and X=S, Se, Te [110, 113]. Artificial stacks of these compounds will also be analyzed in section 4.1.2 of this work.

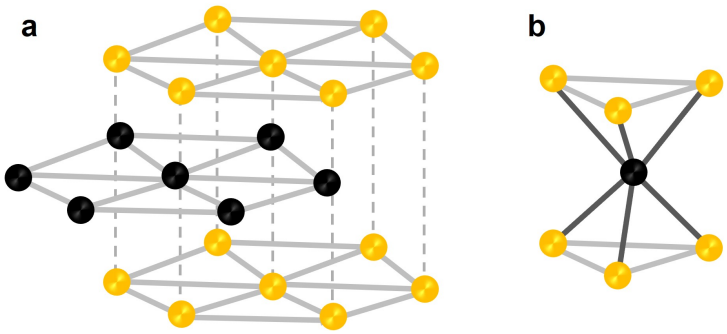

Figure 2.1: Schematic drawing of the crystal structure of an MX_2 TMDC layer. Transition metals M are shown in black and chalcogen atoms X are shown in yellow. The in-plane covalent bonds are shown in light gray. **a** Orthographic side view of the atomic arrangement within one layer. The transition metal atoms are sandwiched between two layers of chalcogen atoms. **b** Orthographic side view of a trigonal prismatic coordination of the chalcogen atoms around the transition metal atoms.

Multilayers of TMDC can be found in different crystal phases. The most common phase is the hexagonal 2H phase, depicted in fig. 2.2**a**. Two neighboring layers are rotated by 60° with respect to each other, resulting in a spatial alignment of transition atoms of one layer with chalcogen atoms of the other layer. Consequently, multilayers show repeating alignment every two layers. This stacking is commonly referred to as *natural* stacking, AB-stacking or 60° stacking and is commercially available for most semiconducting TMDCs. Additionally, for materials like MoS_2, a trigonal prismatic 3R phase can be found. In this phase, the individual layers are not rotated with respect to each other, resulting in a pattern that repeats every three layers, as shown in fig. 2.2**b**. This phase is commonly referred to as ABC-stacking or 0° stack-

ing. The 3R phase of WSe_2 is also synthetically accessible by physical vapor deposition (PVD) techniques.

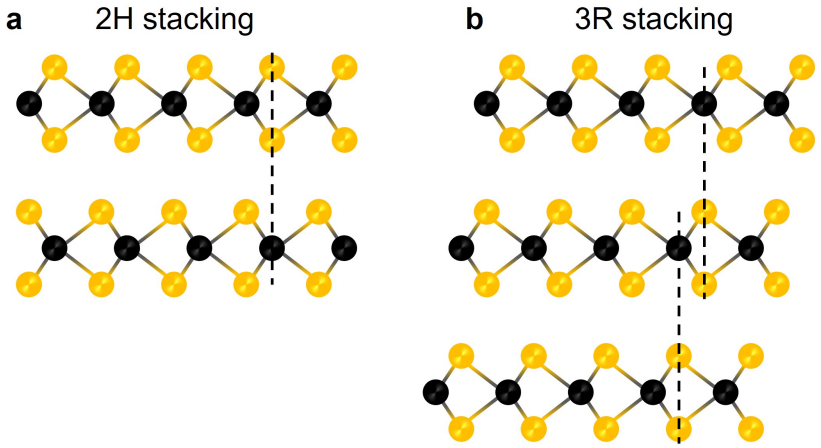

Figure 2.2: Schematic side view of two different crystal stackings of TMDC multilayers. Transition metals are shown in black and chalcogen atoms are shown in yellow. **a** The layers are rotated by 60° with respect to each other in the 2H phase. Chalcogen atoms of one layer overlay with transition metal atoms of the other layer. **b** Representation of the 3R phase. The layers are not rotated with respect to each other. Chalcogen atoms of one layer overlay with transition metal atoms of the neighboring layer. The structure repeats every three layers.

Furthermore, materials like NbS_2 can be found in the 2H phase or in the 3R phase. While the material shows superconducting properties in the 2H phase, the 3R phase is metallic [114]. This shows that the right choice of phase is crucial for the investigation of certain physical properties.

Beside the fabrication of few-layers by means of chemical techniques [40, 52, 109, 115–123] or mechanical exfoliation of bulk crystals [112, 124–126], the posibility of stacking monolayers with defined twist angle enables the fabrication of artificial phases, that do not occur naturally.

As the real-space lattice shows hexagonal symmetry, the first Brillouin zone, as shown in fig. 2.3, is also hexagonal [127]. The high-symmetry points

are labeled. As a result of the two-atom basis, the points in the corners of the Brillouin zone have a rotational symmetry of 120°, making neighboring corners inequivalent. They are labeled alternately as K and K′ points. The point between two neighboring K and K′ points, the middle of one edge of the first Brillouin zone, is referred to as the M point. The center of the Brillouin zone is known as the Γ point. Additionally, the region between Γ and K, labeled as Q, is of particular interest [128].

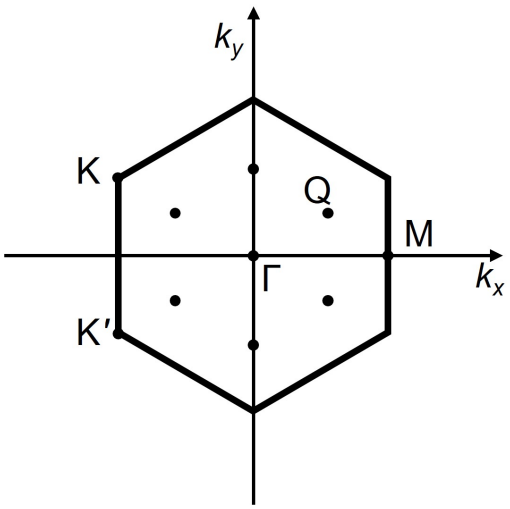

Figure 2.3: Schematic drawing of the first Brillouin zone of the hexagonal lattice of a TMDC. The high symmetry points are labeled. As a result of the two atomic basis, the corners of the first Brillouin zone are inequivalent.

2.1.2 Electronic band structure

In order to investigate and understand optical or electronic effects in semiconducting materials, one needs to consider the material's electronic band structure. For many-body systems, it is not possible to solve the Schrödinger equation analytically [129]. Therefore, one has to use approximations and numerical methods to calculate the band structure. The most common method is density functional theory (DFT) [130, 131]. Here, the ground state of an

N-particle system with a wavefunction, depending on $3N$ coordinates, is replaced by the density of electrons $\rho(\vec{r})$ in the ground state. The properties of the system can be derived as functionals of the density. As a consequence the many-body problem is reduced to a single-particle problem, where the electrons are treated as non-interacting particles in an effective potential which accounts for external effects of the electron-electron interaction. By finding good approximations for the effective potential, the band structure of a material can be calculated.

As a representative for all semiconducting TMDC materials, the band structures of bulk, quadrilayer, bilayer and monolayer MoS_2 are compared in fig. 2.4 [132]. The maximum of the valence band (VB) for the bulk case is calculated to be at the Γ point. Together with the minimum of the conduction band (CB) near the Q valley this results in an indirect bandgap [132, 133]. This behavior also persists for quadrilayer and bilayer of MoS_2. However, the energy of the gap is increased for decreasing layer number. This is achieved by a reduction of the energy of the VB maximum, as well as an increase of the energy of the CB minimum.

In the monolayer case, the minimum of the CB is at the K point, while the maximum of the VB is also located at the K point, resulting in a direct bandgap semiconductor. The shift of energy levels at the Q valley and Γ point is a result of orbital contributions. The states at these points arise from linear combinations of d-orbitals around the Mo atoms and antibonding p_z-orbitals from the S atoms. The involvement of S atoms on the outer side of the material sheet makes these states sensitive to the environment of the material, e.g., adjacent layers. In contrast to the layer-sensitive states, the states at the K point solely arise from strongly localized d-orbitals around the Mo atoms, which are shielded by the S atoms. This makes states at the K point less sensitive to the environment of the material [132, 134–136].

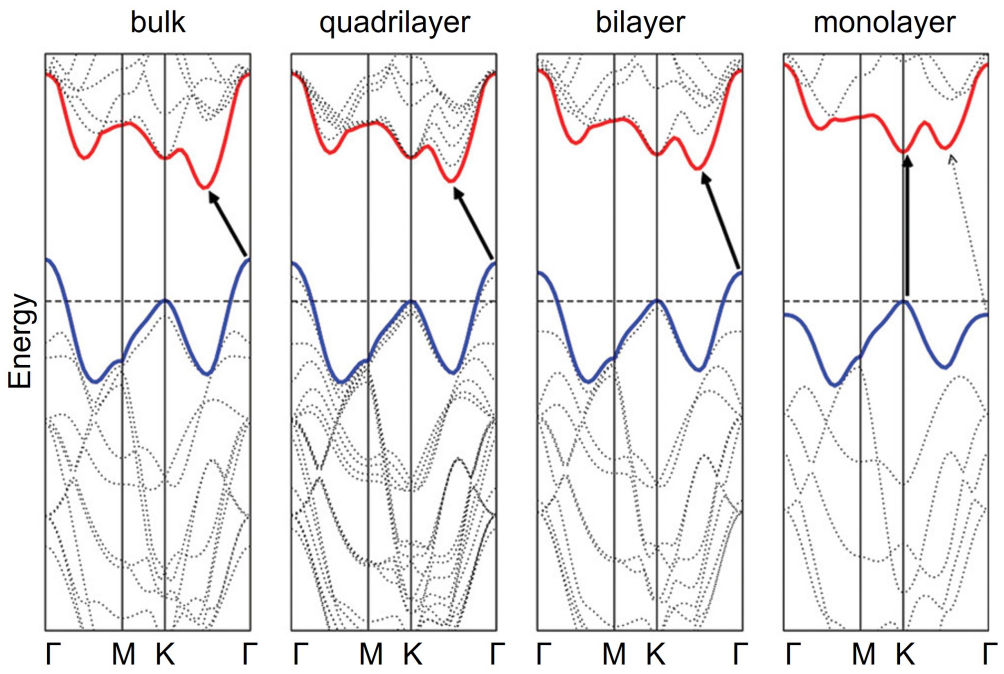

Figure 2.4: Calculated band structure of MoS_2 bulk, quadrilayer, bilayer and monolayer. The transition from the Γ point to the Q valley is the lowest energy transition for bulk, quadrilayer and bilayer. Its energy is increased by lowering the layer number. In the monolayer case, the direct transition at the K point is the lowest energy transition. Adapted from Ref. [132].

2.1.3 Linear optics of excitons in semiconductors

Light emission in a solid occurs when excited electrons recombine with holes, accompanied by the emission of a photon. Prior to recombination, electrons can be promoted to higher energy states either by applying an external voltage, known as electroluminescence or by optical excitation, refered to as PL. In a semiconductor, PL is initiated when a suitable optical field excites an electron from the VB to the CB, leaving behind a hole. The excited electron-hole pair subsequently relaxes non-radiatively to the band extrema via phonon interactions before recombining radiatively.

Quasiparticles such as excitons play a central role in the excitation and recombination process. The optical bandgap, defined by the measured photon energy in PL, E_{PL}, is given by the bandgap energy, E_{G}, reduced by the exciton binding energy, E^{B}:

$$E_{\mathrm{PL}} = E_{\mathrm{G}} - E^{\mathrm{B}}. \tag{2.1}$$

Excitonic properties are highly influenced by the dimensionality of the material. This effect will be discussed in the following section.

2.1.4 Properties of excitonic species and the effect of reduced dimensionality

Commonly, excitons are distinguished into two different types: If the wave function of the exciton is localized in one unit cell, for example in organic crystals, one speaks of Frenkel excitons [137]. In contrast to conventional semiconductors where the exciton can be spread over the area of many lattice cells forming so-called Wannier excitons [138], which can be described in the effective mass approximation. Here, the curvature of the band is correlated with the mass of the electron and the hole. The effective mass m^*, represented as tensor, can be written as

$$\left(\frac{1}{m^*}\right)_{\mathrm{ij}} = \frac{1}{\hbar}\frac{\partial^2 E(k)}{\partial k_{\mathrm{i}} \partial k_{\mathrm{j}}}, \tag{2.2}$$

with reduced Planck's constant $\hbar$ and the curvature of the band $\frac{\partial^2 E(k)}{\partial k_{\mathrm{i}} \partial k_{\mathrm{j}}}$. Assuming a Coulomb interaction of parabolic bands in a direct semiconductor, the two-particle system can be described by a two-particle hydrogen atom model, which leads to energies of bound states n for 3D excitons

$$E^{\mathrm{3D}}(n) = -\frac{\mu}{m_0}\frac{1}{\epsilon_{\mathrm{r}}^2}\frac{R_{\mathrm{H}}}{n^2} = -\frac{R_{\mathrm{X}}}{n^2}, \tag{2.3}$$

where the Rydberg constant $R_\mathrm{H} = 13.6\,\mathrm{eV}$ is scaled by the dielectric constant ϵ_r, the electron mass m_0 and the reduced mass $\frac{1}{\mu} = \frac{1}{m_\mathrm{e}^*} + \frac{1}{m_\mathrm{h}^*}$, with effective electron mass m_e^* and effective hole mass m_h^*, to get the excitonic Rydberg constant R_X. Excitons are only stable if their binding energy is larger than the thermal energy of phonons, which is determined by Boltzmann's constant k_B and the temperature T, leading to a value at room temperature of around $k_\mathrm{B}T \approx 25\,\mathrm{meV}$. In conventional three-dimensional semiconductors, the binding energy of excitons is typically in the range of a few 10 meV, making them unstable at room temperature [139].

When reducing the dimensionality of the material to two dimensions, the binding energy has to be modified [38, 140].

$$E^\mathrm{2D}(n) = -\frac{\mu}{m_0}\frac{1}{\epsilon_\mathrm{r}^2}\frac{R_\mathrm{H}}{\left(n-\frac{1}{2}\right)^2} = -\frac{R_\mathrm{X}}{\left(n-\frac{1}{2}\right)^2} \tag{2.4}$$

Consequently, the binding energy of the first excited state $n = 1$, corresponding to the lowest energy exciton, is increased by a factor of 4 compared to the three-dimensional case.

Furthermore, due to the low dimensionality, the exciton exhibits confinement and a lack of dielectric screening as shown in fig. 2.5. This effect further increases the binding energy of excitons, depicted by the red arrow, to several 100 meV, making them stable at room temperature [33, 38, 141–144]. The dielectric environment can be adjusted by using a few layers of hexagonal boron nitride (hBN) as a cover of the TMDC layer on top and on bottom. The insulating hBN with a bandgap in the deep UV [145] provides a homogenous dielectric environment, which improves the optical properties by reducing the width of absorption and emission lines in optical spectroscopy [146–152].

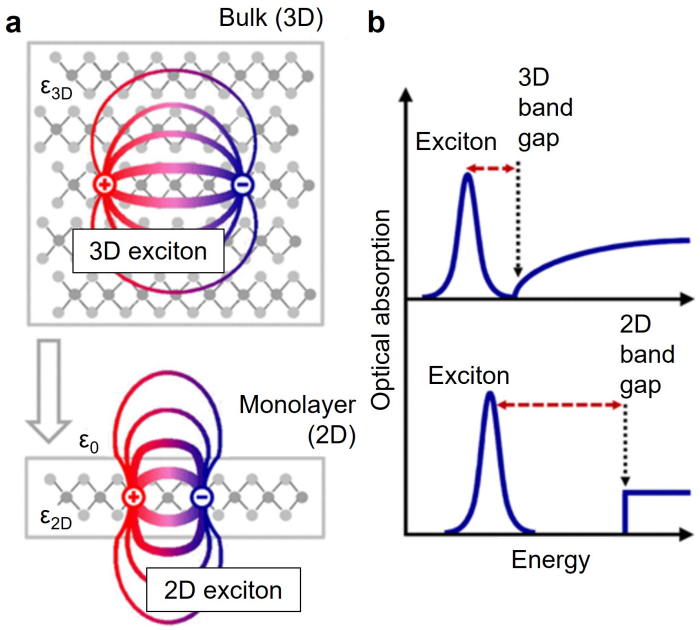

Figure 2.5: Confinement effect of excitons in 2D materials. **a** The electric field lines of an electron-hole pair in a 3D semiconductor exhibit a constant dielectric environment, in contrast to the electric field lines of the electron-hole pair in two dimensions. The change of dielectric environment increases the binding energy of the exciton. This effect is known as reduced dielectric screening. **b** The energy of the exciton in two dimensions is increased with respect to excitons in three dimensions. The binding energy depicted as red arrows is also increased when reducing the dimensionality of the material. Adapted from Ref. [38].

2.1.5 Band edge exciton species

In monolayer TMDCs, the band structure is characterized by a direct bandgap at the K point. The most simple two-particle system, created under optical excitation of one electron from the VB to the CB, is the A-exciton (AX) which is formed at the K point [153–155].

It is possible to create quasiparticles consisting of more than two particles, by doping the system, which adds holes or electrons. Three-particle systems with one hole and two electrons are described as negative trions and can

exist in two different configurations: The charge carriers forming the singlet (X_S^-) exciton are located at the same K point, in contrast to the triplet configuration (X_T^-) where they reside in both K and K′ valleys. Quasiparticles with one electron and two holes are referred to as positive trions (X^+). The binding energy of trions is increased by roughly 30 meV compared to the binding energy of excitons [156].

The described excitonic species so far are referred to as bright excitons, as the transition to the ground state is spin and momentum allowed and therefore recombines radiatively. In contrast, spin-forbidden or momentum-forbidden excitons also play a crucial role in monolayers.

Due to strong spin-orbit coupling in TMDC monolayers, the spin of the electron is intrinsically coupled to the valley degree of freedom. This links the spin of an electron in the highest VB to the spin of an electron in the lowest CB [157, 158]. The band spins are flipped for the K and K′ valleys [159–162]. While the spins of the CB and VB in one valley have opposite direction for W-based materials, they have the same orientation in Mo-based materials, as depicted in fig. 2.6 [153, 155, 163–165].

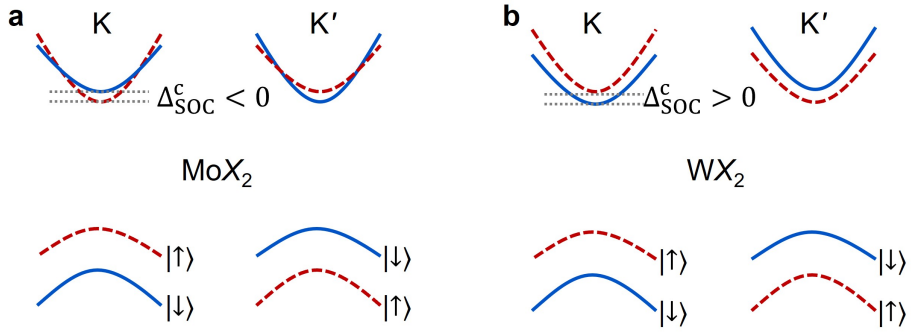

Figure 2.6: Spin-valley coupling in **a** Mo- and **b** W-based TMDCs. The spin of the electron, indicated by color, in the CB is connected to the spin of the electron in the VB. The spins are flipped for the K and K′ valleys. For Mo-based materials, the spins of the CB and VB in one valley have the same orientation, while they have opposite directions in W-based materials. Adapted from Ref. [165].

Theoretical calculations show that contributions to the splitting of spin states in a monolayer of MoS_2 almost cancel out if Coulomb interactions are taken into account [166].

Spin-forbidden excitons, also referred to as dark excitons, are formed by transitions that require a spin flip of the electron in order to recombine. Therefore, they are not radiatively coupled to the ground state and should not contribute to PL. However, they can still be seen in temperature-dependent measurements [167–170], measurements in transverse magnetic fields [171–173] or with out-of-plane dipole moments [174, 175].

Spin-forbidden dark excitons can be formed from a single electron-hole pair (X_D). Their excitonic Rydberg series can be measured by optical means [173]. Spin-forbidden trions with three particles can be either positive (X_D^+), or negative (X_D^-). The exciton-trion separation is smaller for dark excitons than for bright states [176, 177].

Furthermore, it is possible to create more complex quasiparticles, consisting of more than three particles, like biexcitons (XX_D), which are composed of one bright exciton and one dark exciton.

The electrostatic doping of a two-dimensional semiconductor can be controlled by an insulated gate structure, where the gate-voltage-dependent PL of monolayer WSe_2 in fig. 2.7 shows the different excitonic species, depending on the doping in the system. Positive gate voltages induce additional electrons in the material, while negative gate voltages induce additional holes [73, 178–180].

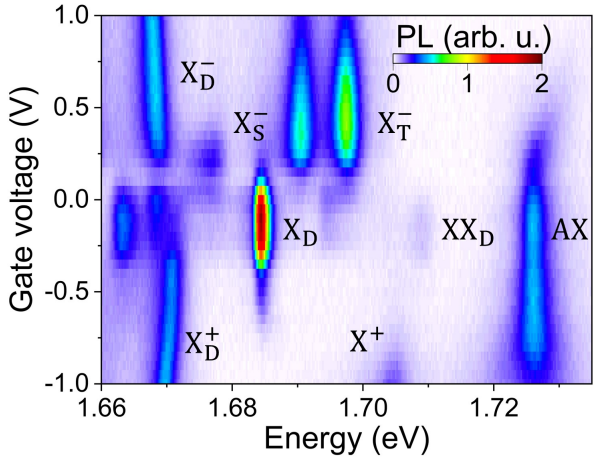

Figure 2.7: Gate-voltage-dependent photoluminescence of monolayer WSe_2 excited using a 488 nm laser at a photon energy of 2.54 eV, above the bandgap. The different excitonic species are labelled as discussed and are observed, depending on the doping in the system. Adapted from Ref. [181].

2.1.6 Radiative lifetimes of excitonic complexes

In order to investigate the temporal dynamics of excitons in TMDC monolayer it is crucial to understand their radiative lifetimes. The radiative recombination rate γ of excitons is proportional to the overlap of electron and hole wavefunction, i.e., finding electron and hole in one unit cell, and is associated with a lower limit in excitonic linewidth. Excitons in two-dimensional TMDC materials exhibit a relatively small Bohr radius on the order of a few nm due to their lack of dielectric screening [38, 182], resulting in fast recombination rates of several meV. This translates to lifetimes $T = \frac{\hbar}{\gamma}$ on the order of 0.1 ps to 1 ps [153, 162, 182–186]. The lifetime is strongly increased for spin- or momentum-dark excitons and reaches values of several hundreds of ps [123, 187]. Even longer lifetimes are measured in heterostructures as they form interlayer excitons with lifetimes up to hundreds of ns [83, 91, 188]. The linewidth, and therefore the lifetime of excitons, can be influenced by exciton

density and temperature. Here, increased exciton-exciton interaction results in a reduced excitonic lifetime for increased exciton densities. The lifetime is also reduced with increasing temperature due to exciton-phonon interaction, as seen in fig. 2.8 [184].

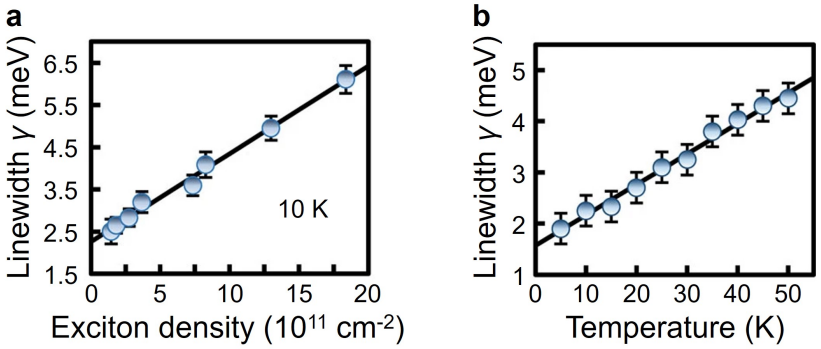

Figure 2.8: Radiative linewidth of excitons in TMDC monolayers for **a** different exciton densities and **b** different temperatures. Adapted from Ref. [184].

2.2 Nonlinear optics

If an electromagnetic wave $\boldsymbol{E}(\mathrm{t})$ interacts weakly with matter, its bound electrons are influenced by the field and a polarization $\boldsymbol{P}(t)$ of the material is generated, which can be written as

$$\boldsymbol{P}(\mathrm{t}) = \epsilon_0 \chi^{(1)} \boldsymbol{E}(\mathrm{t}) \tag{2.5}$$

with the permittivity of free space ϵ_0 and the first-order susceptibility $\chi^{(1)}$ [189].

If the interaction of the electromagnetic wave with the material is increased, nonlinear effects must be considered.

The description of nonlinear optical effects can be separated into two cases. In the *parametric* regime the underlying quantum system of the material is not influenced by the electric field. In the *non-parametric* regime,

the quantum states change their properties under the influence of an electric field. This enables the transfer of energy, momentum, or angular momentum between the material and the electric field. Both processes will be described in the following.

2.2.1 Parametric regime

Following descriptions are based on Ref. [189]. In order to describe nonlinear effects in the framework of parametric excitation, one expands the linear field dependence of the polarization in a Taylor series as

$$\boldsymbol{P}(\mathrm{t}) = \epsilon_0 \left(\chi^{(1)} \boldsymbol{E}(\mathrm{t}) + \chi^{(2)} \boldsymbol{E}^2(\mathrm{t}) + \chi^{(3)} \boldsymbol{E}^3(\mathrm{t}) + \dots \right) \tag{2.6}$$

where $\chi^{(2)}$ and $\chi^{(3)}$ represent the second- and third-order susceptibility, respectively. To investigate second-order processes, one needs to calculate the components of the $\boldsymbol{E}^2$ term. We assume that an electric field, consisting of two different frequency components ω_1 and ω_2 and corresponding amplitudes E_1 and E_2, can be written as

$$E(\mathrm{t}) = E_1 \exp(-i\omega_1 t) + E_2 \exp(-i\omega_2 t) + c.c. \tag{2.7}$$

Any vectorial properties are neglected for simplicity. The second-order polarization is calculated as

$$\begin{aligned} P^{(2)}(\mathrm{t}) = \epsilon_0 \chi^{(2)} E(\mathrm{t})^2 = \epsilon_0 \chi^{(2)} [& E_1^2 \exp(-2i\omega_1 t) + E_2^2 \exp(-2i\omega_2 t) + \\ & E_1 E_2 \exp(-i\left(\omega_1 + \omega_2\right) t) + E_1 E_2^* \exp(-i\left(\omega_1 - \omega_2\right) t) + c.c.] \\ & + 2\epsilon_0 \chi^{(2)} \left[E_1 E_1^* + E_2 E_2^* \right]. \end{aligned} \tag{2.8}$$

For convenience the polarization can be written in the form of the following summation

$$P^{(2)}(\mathrm{t}) = \sum_n P(\omega_\mathrm{n}) \exp(-i\omega_n t). \tag{2.9}$$

The nonlinear polarization can be separated into the corresponding frequency components

$$\begin{aligned} P(2\omega_1) &= \epsilon_0 \chi^{(2)} E_1^2 && \text{(SHG)} \\ P(2\omega_2) &= \epsilon_0 \chi^{(2)} E_2^2 && \text{(SHG)} \\ P(\omega_1 + \omega_2) &= \epsilon_0 \chi^{(2)} E_1 E_2 && \text{(SFG)} \\ P(\omega_1 - \omega_2) &= \epsilon_0 \chi^{(2)} E_1 E_2^* && \text{(DFG)} \\ P(0) &= 2\epsilon_0 \chi^{(2)} \left(E_1 E_1^* + E_2 E_2^*\right) && \text{(OR).} \end{aligned} \tag{2.10}$$

Each frequency component of the polarization describes a second-order physical process, such as second-harmonic generation (SHG), sum-frequency generation (SFG), difference-frequency generation (DFG) and optical rectification (OR). A comparable calculation can be done for the third-order susceptibility, which can be written as

$$P^{(3)}(\mathrm{t}) = \epsilon_0 \chi^{(3)} E(\mathrm{t})^3. \tag{2.11}$$

Here, we only consider selected terms of the third-order polarization, including third-harmonic generation (THG) and four-wave mixing (FWM)

$$\begin{aligned} P(3\omega_1) &= \epsilon_0 \chi^{(3)} E_1^3 && \text{(THG)} \\ P(3\omega_2) &= \epsilon_0 \chi^{(3)} E_2^3 && \text{(THG)} \\ P(2\omega_1 - \omega_2) &= 3\epsilon_0 \chi^{(3)} E_1^2 E_2^* && \text{(FWM).} \end{aligned} \tag{2.12}$$

For complete descriptions, see Ref. [189]. The nonlinear polarization is nonzero only if higher-order susceptibilities χ^n for $n \geq 2$ are nonzero. For nonzero $\chi^{(2)}$, broken inversion symmetry is required, while nonzero $\chi^{(3)}$ can be found in both centrosymmetric and non-centrosymmetric materials.

This description is only valid in a parametric regime, where the quantum states of the material are not modified by the electric field and the initial quantum state is equal to the final state: population from the ground state

is only transferred to virtual states for a very short time that is on the order of $\frac{\hbar}{\delta E}$ where δE is the energy difference between the nearest real state and the virtual state [189].

2.2.2 Non-parametric regime

Generally speaking, the nonlinear susceptibility tensor, obtained from the classical anharmonic oscillator model, is a complex entity. Comparable to the refractive index, the nonlinear susceptibility of lossless media can be described solely by the real part, which is the benchmark of parametric nonlinear optics.

In contrast, the non-parametric regime can only be described by the full complex tensor. As the imaginary part of the susceptibility is related to the absorption of the material, real energy states of the material must be considered within the non-parametric regime. Furthermore, the photon energy does not need to be conserved in this regime. Therefore, descriptions according to eq. (2.5) are not valid anymore, and a more sophisticated model is required [189]. For this, the time-dependent polarization of the system is calculated by the density-matrix formalism, which is presented in the following chapter.

2.3 Density-matrix formalism

During this work, not only experimental data was obtained. We performed simulations of the nonlinear signals by using a density-matrix approach, which is a powerful tool to describe the interaction of light with matter, especially in the context of quantum optics and nonlinear optical processes [189]. However, the simulated results only provide hints on the underlying physics, leaving space for interpretation of the results.

The underlying formalism is described in the following. The density-

matrix formalism is based on the concept of a density operator $\hat{\rho}$,

$$\hat{\rho} = \sum_i p_i \left|\psi_i\right\rangle \left\langle\psi_i\right| \tag{2.13}$$

where p_i describes the probability of finding the system in state $|\psi_i\rangle$. The time evolution of the density operator is described by the Lindblad equation

$$\frac{d}{dt}\hat{\rho} = \frac{1}{i\hbar}[\hat{H}, \hat{\rho}] - \frac{1}{2}\{\hat{\Gamma}, \hat{\rho}\} + \hat{\Lambda}. \tag{2.14}$$

The diagonal components of the Hamiltonian are given by the energies of the states $\mathcal{E}_i$

$$H_{ii} = \mathcal{E}_i. \tag{2.15}$$

The off-diagonal components of the Hamiltonian describe the coupling between the states, which is given by the electric field of the laser pulse $E(\mathrm{t})$ and the transition dipole moment μ_{ij} between two states

$$H_{ij} = -E(\mathrm{t})\mu_{ij} \qquad (i \neq j). \tag{2.16}$$

Relaxation processes are described by a decay matrix $\hat{\Gamma}$ with only nonzero elements on the diagonal, which are connected with the lifetimes of the states Γ_i

$$\hat{\Gamma}_{ij} = \Gamma_i \qquad (i > 1). \tag{2.17}$$

Repopulation of the ground state is included by the repopulation matrix $\hat{\Lambda}$, which has one nonzero element

$$\hat{\Lambda}_{11} = \sum_{i>1} \Gamma_i \rho_{ii}. \tag{2.18}$$

The model system is excited with a pulsed laser field, described by a Gaussian-

shaped electric field

$$E(\mathrm{t}) = E_0 \cdot \exp\left(-i\omega_0 t - 2\ln 2\left(\frac{t-t_0}{\Delta t_{\mathrm{fwhm}}}\right)^2\right) \tag{2.19}$$

with amplitude E_0, center frequency ω_0, center time t_0 and full width at half maximum Δt_{fwhm}.

The time-dependent polarization of the system is calculated by

$$P(\mathrm{t}) \sim \sum_{ij} \mu_{ij}\rho_{ij}(\mathrm{t}). \tag{2.20}$$

A Fourier transform of the time-dependent polarization gives the frequency-dependent polarization $P(\omega)$, which can be interpreted as a spectrum generated by the system.

Having established the theoretical background of excitonic species in TMDCs, basic concepts of nonlinear optics and the density-matrix formalism, we can turn to novel excitonic species in TMDCs, where high-lying states with energies above the bandgap influence the optical response of the material system.

2.4 High-lying excitons

This chapter aims to review the current scientific understanding concerning HX in TMDCs. This overview provides the necessary foundation for understanding the fundamental properties of HX and prepares the ground for the experimental results presented in this work.

The first indication of the existence of excitons formed by energy states far above the bandgap in TMDCs was reported in 2019 [190], in a study examining the SHG signal of a monolayer WSe_2 at cryogenic temperatures. Under typical circumstances, the SHG signal, produced by pulsed laser excitation, exhibits a comparable Gaussian spectral profile to the incident laser,

since it represents the transform limited convolution of two Gaussian-shaped laser spectra. Under certain specific conditions, however, the SHG spectrum displays a more complex structure. As shown in fig. 2.9**a**, the SHG spectrum features a spectral bifurcation, also referred to as spectral anticrossing. Both experimental data and simulated spectra show a pronounced dip that appears at a specific energy within the SHG spectrum. This characteristic energy is assigned to the transition energy of state $|3\rangle$ to the ground state, denoted as E_3. The fig. 2.9**b** illustrates the process proposed in the original work to explain the observed SHG splitting. The system is described as a

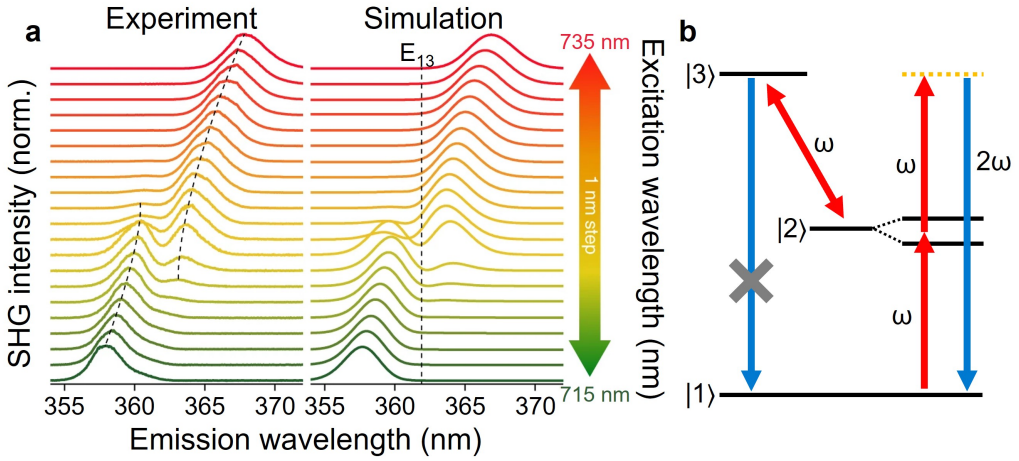

Figure 2.9: First observation of spectral bifurcation in the SHG signal of a monolayer WSe_2. **a** Comparison between wavelength-dependent SHG spectra obtained experimentally and through simulation. A dip is observed at the same energy in both cases and is attributed to the transition from the ground state to a HX. **b** Schematic of the underlying process. Strong electric field couples $|2\rangle$ and $|3\rangle$. The SHG dip arises from interference between the two excitation pathways, $|1\rangle \rightarrow |2\rangle$ and $|3\rangle \rightarrow |2\rangle$. Adapted from Ref. [190].

ladder-type three-level configuration, consisting of the ground state $|1\rangle$, the first excited state $|2\rangle$, the AX, and a third state $|3\rangle$, corresponding to the HX. Strong electric-field-driven coupling between $|2\rangle$ and $|3\rangle$ results in the formation of dressed states, analogous to those observed in electromagnetically

induced transparency (EIT) [191–199]. The dip in SHG signal arises from the interference between two excitation pathways, $|1\rangle \rightarrow |2\rangle$ and $|3\rangle \rightarrow |2\rangle$, leading to spectral suppression. Since $|3\rangle$ is not coupled to the ground state $|1\rangle$, it does not contribute to emission. Therefore, this state will be referred to as the *p*-like HX in the following.

Figure 2.10 provides a more detailed depiction of the process responsible for the SHG dip. Simulated results, obtained by density-matrix dynamics, shown in the two upper rows, are compared with the corresponding measured spectra. The top row presents the simulated population dynamics of the three-level system under the influence of a laser field, while the second row displays the resulting SHG spectra. In the middle column, the laser field has an energy of 3.3 pJ and a pulse duration of 80 fs. The population dynamics reveal that under this simulation conditions, a single Rabi oscillation occurs between states $|2\rangle$ and $|3\rangle$. The corresponding SHG spectrum exhibits a single dip at the energy of state $|3\rangle$, with the measured spectrum showing excellent agreement with the simulation.

In the left column, the pulse energy of the electric field is increased to 9.2 pJ while maintaining the same pulse duration of 80 fs. The resulting population dynamics display two Rabi oscillations between $|2\rangle$ and $|3\rangle$, leading to an SHG spectrum with two dips, a feature reproduced in both the simulated and experimental data.

For the right column, the laser pulse energy is set to 3.3 pJ, but the pulse duration is extended to 140 fs. The population dynamics again indicate two Rabi oscillations between $|2\rangle$ and $|3\rangle$, and the resulting SHG spectra from both simulation and experiment exhibit two dips. From these observations, it can be concluded that the number of Rabi oscillations can be increased either by raising the laser pulse energy or by lengthening the pulse duration. Furthermore, the number of Rabi oscillations is directly correlated with the number of dips observed in the SHG spectrum.

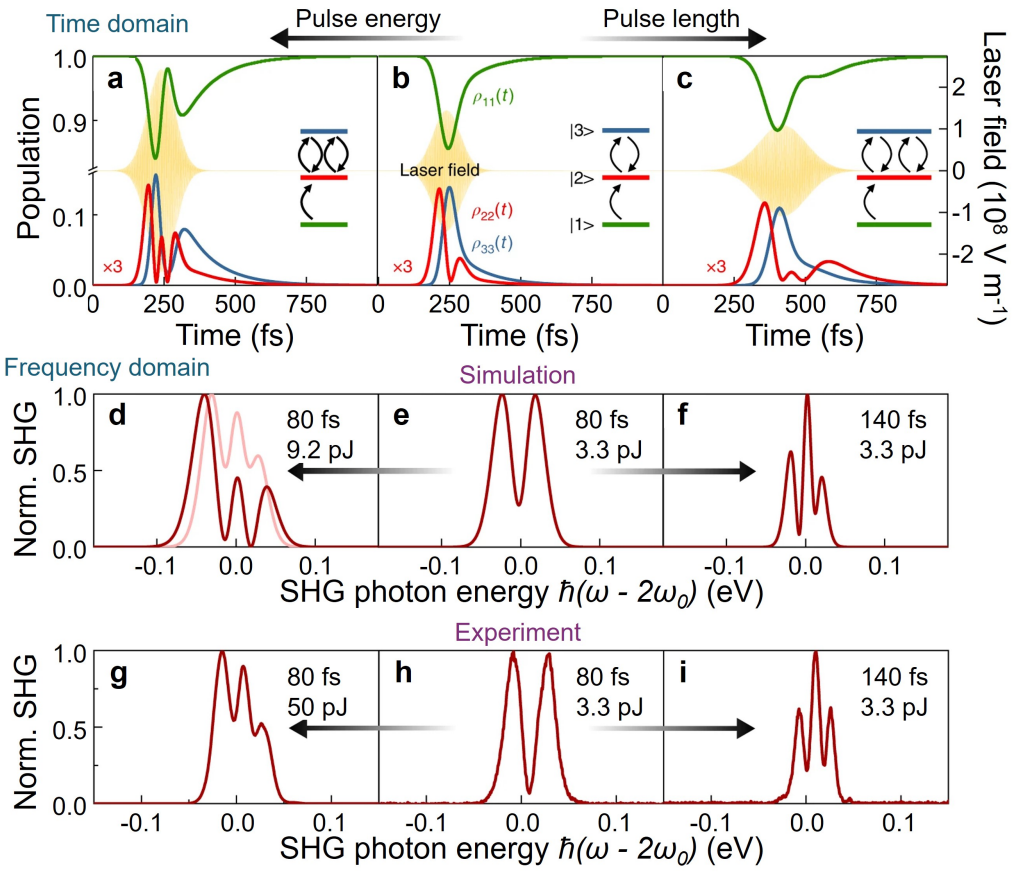

Figure 2.10: Comparison between simulated population dynamics (**a**-**c**) and corresponding simulated SHG spectra (**d**-**f**) with experimentally measured SHG spectra (**g**-**i**) for different pulse lengths and energies. The number of Rabi oscillations between states $|2\rangle$ and $|3\rangle$ during the laser pulse (yellow) determines the number of dips in the SHG spectrum. Adapted from Ref. [190].

Another parameter for probing the SHG dip is the sample temperature, which allows investigation of the effects of decoherence and inhomogeneous broadening of excitonic resonances [190]. The wavelength-dependent SHG dip of monolayer WSe_2 at various sample temperatures is shown in fig. 2.11. A clear temperature dependence is observed. The SHG anticrossing is most pronounced at the lowest temperature of 5 K. As the temperature increases,

the dip becomes progressively shallower and vanishes. At 100 K, a small kink remains visible, whereas at 200 K, the SHG spectrum exhibits the trivial linear dependence on excitation wavelength. Furthermore, the position of the SHG dip, corresponding to the energy of the third state $|3\rangle$, shifts to higher wavelengths with increasing temperature.

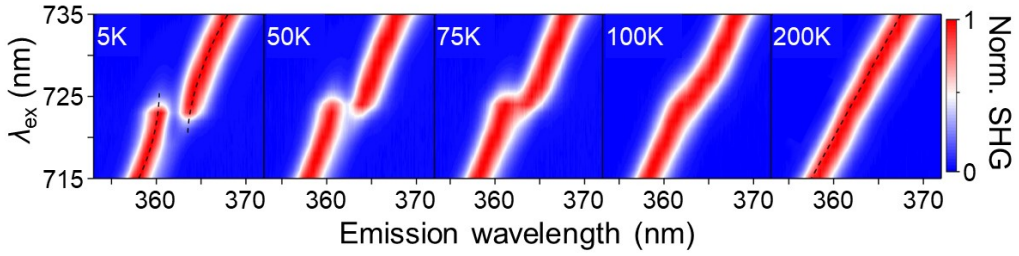

Figure 2.11: Temperature dependence of the excitation-wavelength dependent SHG, measured at temperatures ranging from 5 K (left) to 200 K (right). With increasing temperature, the dip becomes shallower and disappears. The dip energy shifts to higher wavelengths with increasing temperature. Adapted from Ref. [190].

Another approach to probe excitonic resonances is to examine their influence on the power-law exponent of the SHG signal: here, the detected intensity of the SHG process is analyzed as a function of the excitation power, for various excitation wavelengths, following $\int I_{\mathrm{SHG}}(\lambda_{\mathrm{em}}, \lambda_{\mathrm{ex}}) d\lambda_{\mathrm{em}} \propto I_{\mathrm{ex}}^{p(\lambda_{\mathrm{ex}})}$. For a trivial SHG process, the power-law exponent $p(\lambda_{\mathrm{ex}})$ is equal to 2, reflecting the involvement of two photons in the generation process. Excitonic resonances, however, can modify this exponent: a reduction in the power-law exponent is indicative of the AX resonance, as this state saturates when excited with a high-power laser.

Simulations reveal that in a three-level system, the effect of resonant excitation is more complex. When the excitation is close to the two-photon resonance of the $|1\rangle$ to $|3\rangle$ transition, the power-law exponent exhibits a dispersive feature. Due to AC-Stark shifts of the energy levels, the exponent decreases for blue-detuned excitation and increases for red-detuned excitation

[190]. The measured power-law exponent of the SHG signal from monolayer WSe_2 is presented in fig. 2.12. The power-law exponent of the SHG signal

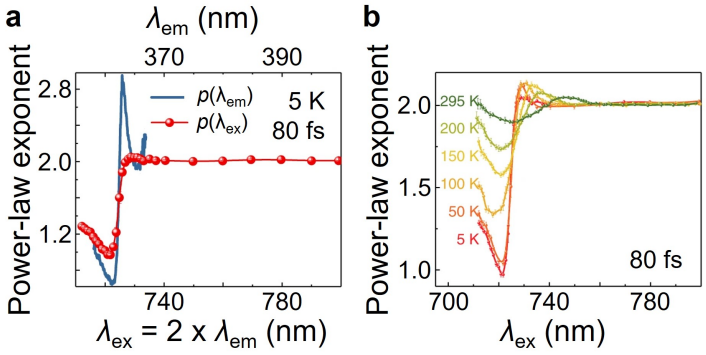

Figure 2.12: Power-law exponent measurements of the SHG signal reveal excitonic resonances. **a** The power-law exponent of the SHG signal, obtained under excitation at 724 nm (blue line), exhibits a Fano-like line shape as a function of emission wavelength. The power-law exponent for different excitation wavelengths is shown as red dots. **b** The influence of excitonic resonances on the power-law exponent persists even at room temperature, providing a robust signature of the excitonic three-level system. Adapted from Ref. [190].

from monolayer WSe_2 is resolved with respect to both excitation and emission energy for different temperatures, clearly demonstrating the impact of excitonic transitions. Notably, the effect of excitonic resonances remains observable even at room temperature. A more detailed discussion of the power-law exponent analysis is provided in section 2.5.

The influence of the dielectric environment on excitonic resonances, and consequently on the SHG dip, is examined in the publication reviewed next [200]. In this study, a monolayer of WSe_2 is placed on a 285 nm-thick layer of SiO_2 deposited on a Si substrate. The samples are then encapsulated with various materials, including hBN, PMMA, Zeonex, and PS. The effect of the dielectric environment is investigated through measurements of both the PL spectrum and the SHG dip. It is observed that the dielectric environment

alters the energies of the excitonic species. In fig. 2.13, the energies of the AX are plotted against the energies of the SHG dip, which correspond to the HX, for the different dielectric environments. The data points for all materials lie on a straight line with a slope of 1. This linear relationship indicates that both excitonic species originate from the CB and that the spectral bifurcation of the SHG spectrum cannot be attributed to a biexciton [200].

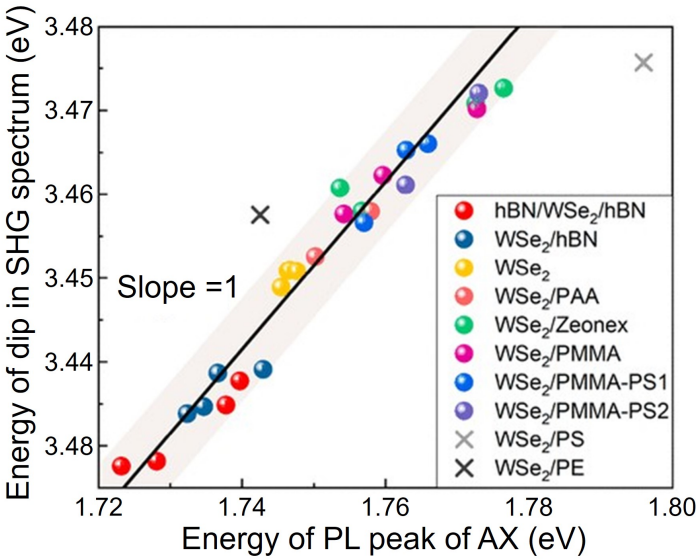

Figure 2.13: Energy of the SHG dip plotted against the energy of the AX for different dielectric environments. The black line has a slope of 1. Adapted from Ref. [200].

In addition to the *p*-like HX, the existence of an *s*-like HX has been proposed in [201]. For this, a resonant excitation of the AX, leading to an Auger-like energy transfer to a higher-lying state is suggested. The energy of this *s*-like HX is 3.4 eV, slightly lower than twice the energy of the AX at 1.732 eV, as shown in fig. 2.14. *Ab initio* GW-BSE calculations reveal an energy level labeled CB+2 at the corresponding transition energy.

Notably, the curvature of the CB+2 band is negative, indicating a nega-

tive effective electron mass. The HX signal, obtained via upconverted photoluminescence (UPL), exhibits a pronounced multi-peak structure. The peaks are equally spaced by 15.5 meV, suggesting an energy reduction via emission of a longitudinal acoustic (LA) phonon, which scatters the electron between the K and K′ valleys and back. The intensity of every even-numbered peak is enhanced relative to the odd-numbered peaks, an effect attributed to a required spin flip for odd numbers of phonon-assisted transitions between different K points.

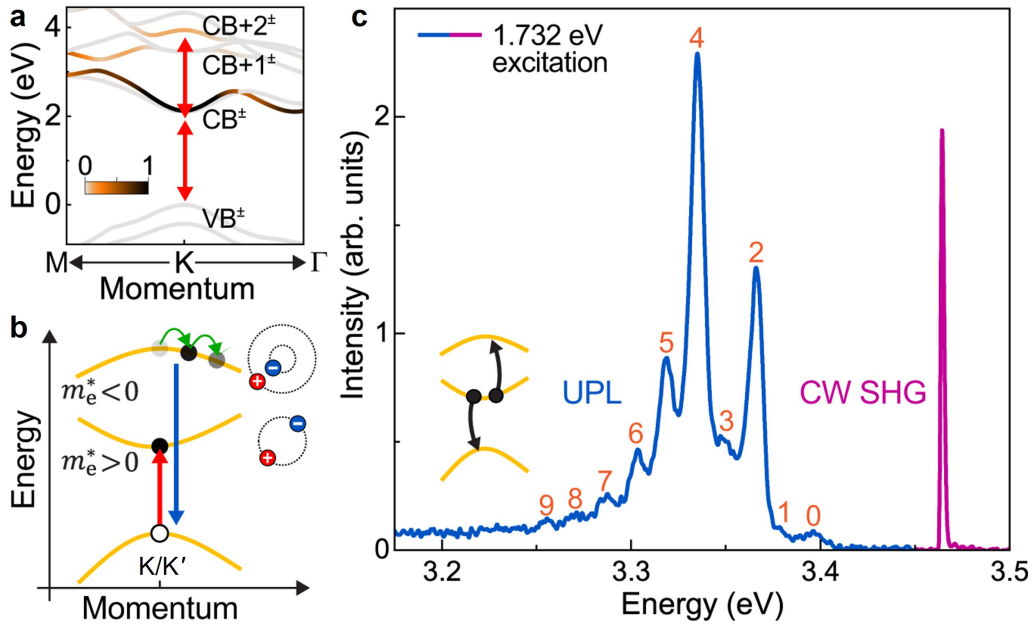

Figure 2.14: **a** Calculated band structure of monolayer WSe_2, with oscillator strength encoded in the color scale. The VB, CB, and higher conduction bands CB+1 and CB+2 are labeled. **b** Simplified band structure around the K point, highlighting the bands responsible for the AX (CB) and the *s*-like HX (CB+2). **c** UPL spectrum of monolayer WSe_2 under resonant excitation of the AX, showing a multi-peak structure consistent with the presence of the *s*-like HX. Adapted from Ref. [201].

Figure 2.15 illustrates two possible mechanisms for exciting the *s*-like HX. One approach involves resonant excitation of the AX with a continuous-wave

(cw) laser, generating a high exciton-density.

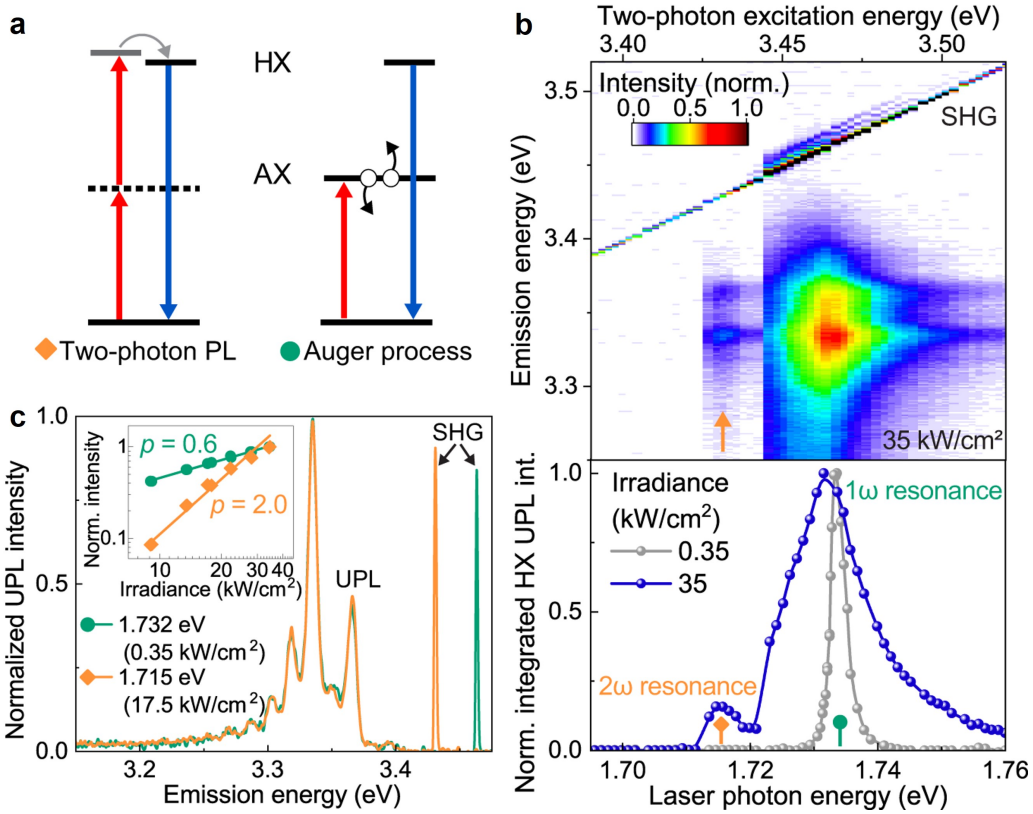

Figure 2.15: Comparison of two mechanisms for exciting the *s*-like HX. **a** The *p*-like HX can be excited via two-photon resonance, with subsequent nonradiative transfer of population to the *s*-like HX. Resonant excitation of the AX followed by an Auger-like process promotes an electron to a higher CB. **b** The two processes are distinguishable by their excitation energy dependence. The two-photon process requires higher irradiance than the Auger process. **c** Both processes yield the same UPL spectrum but exhibit different power-law exponents: 0.6 for the Auger process and 2 for the two-photon process. Adapted from Ref. [201].

Through an Auger-like recombination process, the energy of one electron is transferred to another, promoting it into a higher CB and creating HX that subsequently recombines radiatively. The second mechanism is a two-photon

luminescence process, in which the *p*-like HX is resonantly excited by two photons of the cw laser. The population is then transferred nonradiatively from the *p*-like to the *s*-like HX, which recombines radiatively to the ground state. These two processes can be clearly distinguished by their differing excitation-energy-dependencies and distinct power-law exponents.

By comparing experimental results with *ab initio* GW-BSE calculations, the authors conclude that the *s*-like HX originates from the CB+2 and is localized around the K valleys.

Few layers of TMDCs offer remarkable versatility for fabricating artificial heterostructures by stacking individual layers. In such systems, not only the choice of material combinations but also the twist angle between layers plays a crucial role, as it can significantly alter the material properties [43]. The influence of twist angle on excitonic resonances has been investigated in [202]. Experiments were conducted on several twisted WSe_2 bilayers, employing PL, UPL, and SHG anticrossing measurements. The twist angle was precisely controlled during fabrication and verified via polarization-resolved SHG measurements. It was varied from 1° to 59° in increments of approximately 6°. As shown in fig. 2.16, the energy of the AX, determined from PL measurements, depends on the twist angle, with an average twist-angle susceptibility of 0.8 meV/°. In contrast, the *s*-like HX exhibits a much stronger dependence, with an average twist-angle susceptibility of 8.1 meV/°.

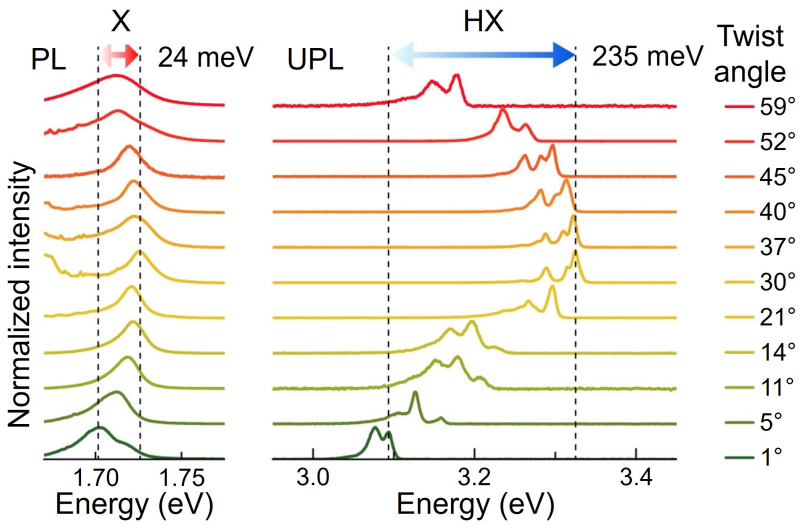

Figure 2.16: Excitonic resonances obtained from PL and UPL measurements for twist angles ranging from 1° to 59°. The AX energy can be tuned by 24 meV, whereas the *s*-like HX energy can be tuned by 235 meV. Adapted from Ref. [202].

The pronounced twist-angle dependence of excitonic resonances also affects the SHG dip, as it is directly linked to the energetic position of the *p*-like HX. As shown in fig. 2.17**a**, the anticrossing feature, as discussed earlier, is observed only for twist angles between 21° and 45°. Outside this range, the SHG signal exhibits a trivial linear dependence on excitation wavelength. To explain this behavior, the authors calculated the partial charge density of the relevant states. The results show that the VB and the CB have charge density contributions localized around the tungsten atoms, whereas the CB+2 has a more delocalized contribution around the selenium atoms, as shown in fig. 2.17**b,c**. This delocalization renders CB+2 more exposed to its environment and thus more sensitive to external perturbations.

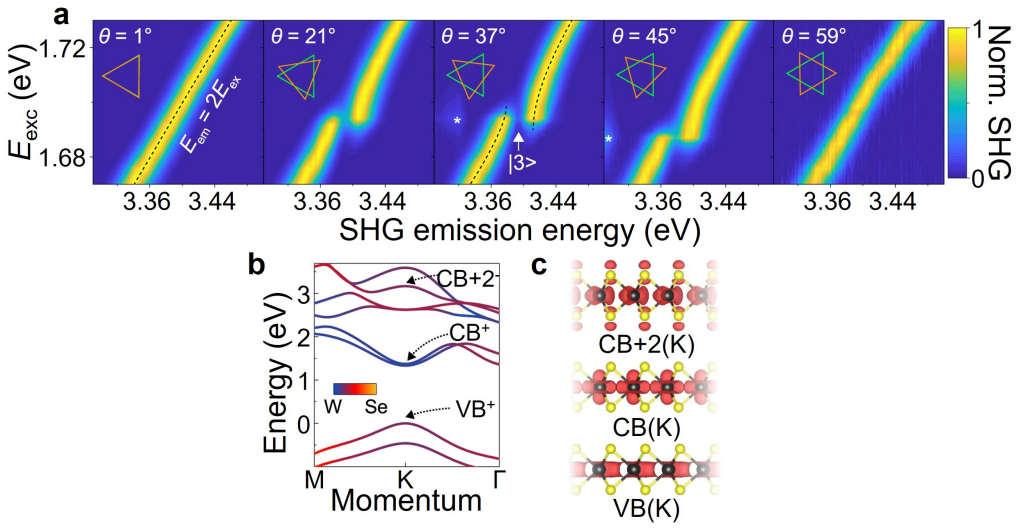

Figure 2.17: **a** Excitation-energy dependence of the SHG signal for different twist angles. The anticrossing feature is present only for twist angles between 21° and 45°. Outside of this range, the SHG signal shows a trivial linear dependence. **b** Simulated band structure of monolayer WSe_2, with wavefunction projections color-coded by atomic contribution. **c** Partial charge density at the K points, showing VB and CB contributions centered on tungsten atoms, while CB+2 is more delocalized around selenium atoms. Adapted from Ref. [202].

Since both the *p*-like HX and *s*-like HX originate from the same region in the band structure, a similar twist-angle dependence is expected. The angle-dependent energies of the *s*-like HX, the *p*-like HX, and twice the AX energy are shown in fig. 2.18. The disappearance of the quantum interference dip in SHG at small and large twist angles is attributed to the loss of the resonance condition of almost equal energy differences of the transition $|1\rangle$ to $|2\rangle$ and $|2\rangle$ to $|3\rangle$ caused by the strong redshift of the HX energies.

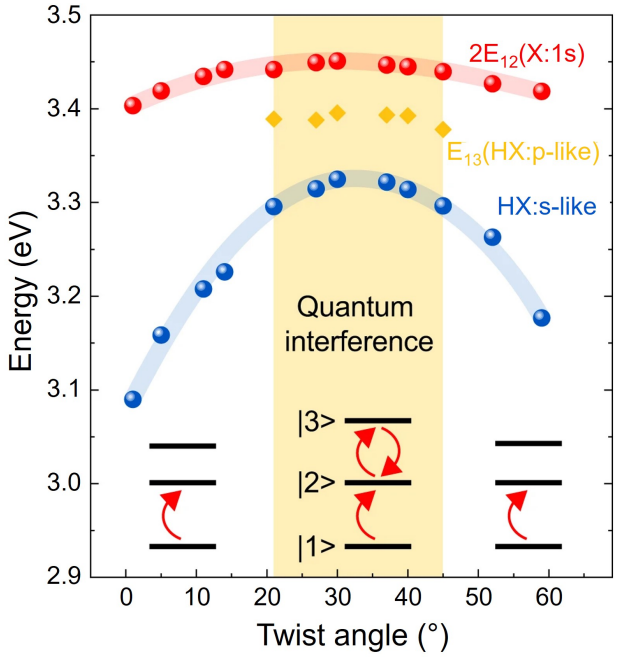

Figure 2.18: Energies of the AX (from PL), the *p*-like HX (from SHG dip), and the *s*-like HX (from UPL) plotted against twist angle. The orange region marks the range where quantum interference occurs. As the HX energies shift more strongly with twist angle than the AX, the resonance condition is lost for angles below 21° and above 45°. Adapted from Ref. [202].

Given the similar band structures of semiconducting TMDCs, it is reasonable to speculate that quantum interference effects involving HXs could also be observed in other materials, such as $MoSe_2$. However, in the monolayer case, the energy separation between states $|2\rangle$ and $|3\rangle$ is apparently larger than that between $|1\rangle$ and $|2\rangle$, preventing the resonance condition from being met, as shown in fig. 2.19**a** [202].

In twisted bilayers of WSe_2, the energy of the third state $|3\rangle$ can be tuned via the twist angle. This tuning parameter is used in a twisted bilayer of $MoSe_2$ with a twist angle of 0°, where the bandstructure is altered and the SHG spectrum exhibits an anticrossing feature, indicating quantum

interference, as shown in fig. 2.19**b**. This highlights the universal character of HXs in different semiconducting TMDC materials, which will be further investigated and presented in section 4.1.2.

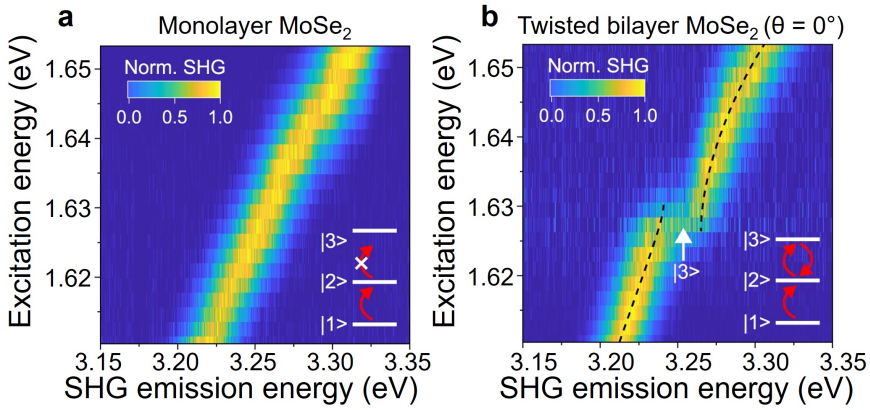

Figure 2.19: **a** Excitation-energy dependence of the SHG signal for monolayer $MoSe_2$, showing a trivial linear dependence due to the absence of the resonance condition. **b** Excitation-energy dependence of the SHG signal for a twisted bilayer $MoSe_2$ with a twist angle of 0°, showing an anticrossing feature at 3.25 eV, indicative of quantum interference. Adapted from Ref. [202].

Another effective tuning parameter for excitonic properties in TMDCs is the use of biased gates placed in proximity to the TMDC layer. Such gated structures enable the investigation of out-of-plane electric field effects as well as modulation of the charge carrier density through electrostatic doping. The dependence of HX on gate voltage is shown in fig. 2.20 [181]. Remarkably, under both positive and negative gate voltages, additional peaks emerge in the UPL spectrum. These features are assigned to the negative high-lying trion (HX^-) and the positive high-lying trion (HX^+). The energy separation from the neutral HX, in this case referred to as HX^0 is 35.2 meV for HX^+ and 42.6 meV for HX^-. This trend mirrors the observed binding energy for band-edge trions, but with binding energies approximately 1.4 times larger. Polarization-resolved UPL measurements reveal a striking difference in optical selection rules. The HX^- exhibits co-polarized emission, whereas HX^+

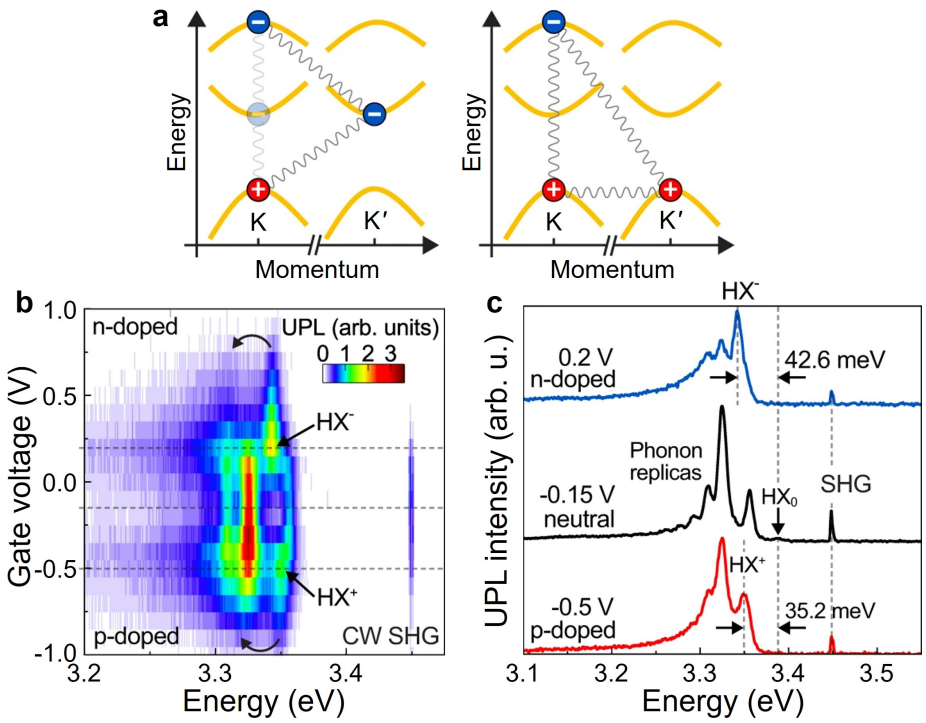

Figure 2.20: **a** Schematic of the charge configurations for negatively (left) and positively (right) charged high-lying trions. In HX^-, the resident electron occupies the first CB at either the K or K′ valley, while in HX^+, the resident hole resides in the VB. **b** Gate voltage-dependent UPL spectra of a monolayer WSe_2 device and **c** selected UPL spectra, showing the HX^0, its phonon replica, and the charged HX^- and HX^+. The energy offsets relative to HX^0 are 42.6 meV for HX^- and 35.2 meV for HX^+. Adapted from Ref. [181].

is cross-polarized. This contrast is attributed to the distinct nature of the respective resident charge carriers.

The influence of gate voltage on quantum interference, involving *p*-like HX, is presented in fig. 2.21. For the ungated device, the SHG spectrum displays the well-known anticrossing feature at the energy of the *p*-like HX (left panel). Upon increasing the gate voltage to 1.5 V (middle panels), a second anticrossing feature emerges at a slightly lower excitation energy.

This additional dip appears 42 meV below the primary anticrossing, in excellent agreement with the binding energy of the HX^- observed in the UPL measurements. The second feature is, therefore, attributed to a quantum interference process in a three-level system comprising the ground state, the negative band-edge trion, and the negative high-lying trion.

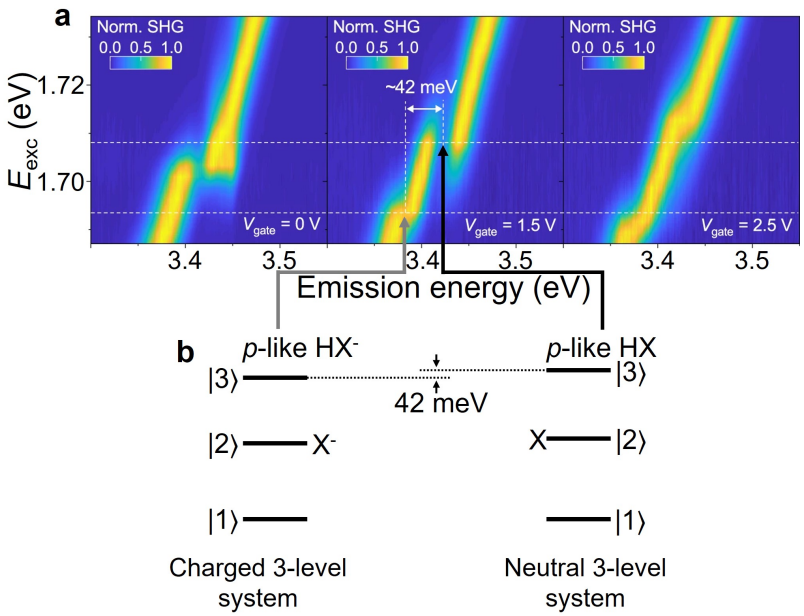

Figure 2.21: **a** Excitation-energy-dependent SHG signal for the ungated device, showing the characteristic anticrossing at the *p*-like HX. Increasing the gate voltage to 1.5 V induces a second anticrossing at lower energy. **b** This second feature is attributed to quantum interference in a three-level system consisting of the ground state, the negative band-edge trion, and the negative high-lying trion. Adapted from Ref. [181].

Finally, the influence of an out-of-plane electric field on excitonic species has been investigated in [203]. Since such a field is expected to affect only excitons with an out-of-plane dipole moment, a bilayer WSe_2 sample was studied, where the wavefunction of the HX is anticipated to be spread over both layers, rendering it sensitive to the applied field. The UPL spectrum

obtained from a dual-gated bilayer WSe_2 device is shown in fig. 2.22**a**. The narrow HX peak, accompanied by its previously discussed phonon replica, exhibits a pronounced Stark-shift under the electric field, which is shown in fig. 2.22**b**. From these measurements, a dipole moment of $\mu_{HX} = 0.26\,\mathrm{e\,nm}$ and a polarizability of $\alpha_{HX} = 0.82\,\mathrm{eV\,nm^2\,V^{-2}}$ were extracted by polynomial fitting of the electric field-dependent exciton peaks. Although these values are smaller than those reported for interlayer excitons in heterostructures [90, 188], they highlight the hybridized nature of the HX.

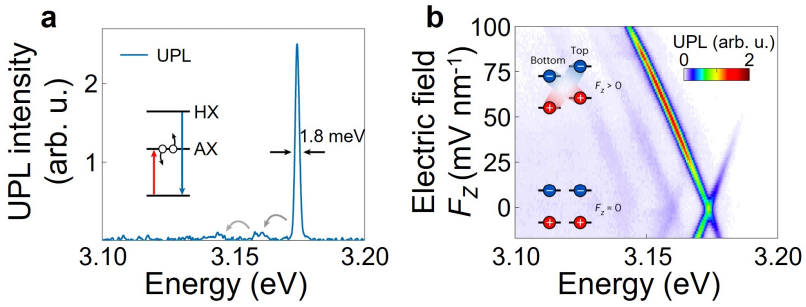

Figure 2.22: **a** UPL spectrum of the bilayer WSe_2 device, obtained via Auger recombination, showing HX with a linewidth of 1.8 meV and its phonon replica. **b** The heatmap of UPL spectra as a function of applied out-of-plane electric field gives rise to a pronounced Stark-shift of the HX. The insets schematically illustrate the contribution of charge carriers. Adapted from Ref. [203].

Further investigation of high-lying trion species in bilayer WSe_2 reveals an HX^+ located 19 meV below the neutral HX, and an HX^- located 29 meV below the neutral HX. Both trions exhibit a Stark-shift under an out-of-plane electric field, reinforcing their interlayer character. Interestingly, the dipole moment of HX^- is $0.95\,\mu_{\mathrm{HX}}$, while that of HX^+ is $1.3\,\mu_{\mathrm{HX}}$, relative to the neutral HX. This asymmetry is attributed to the distinct momentum-space locations of the resident carriers. The additional electron in HX^- occupies the Q valley, whereas the additional hole in HX^+ resides at the K point. The larger dipole moment of HX^+ can be explained by the fact that states

originating from the Q valley are more strongly hybridized between the layers, modifying the spatial charge distribution and, thus, the dipole strength.

Having now reviewed the main experimental findings regarding HXs in established publications, we proceed to provide a detailed description of the modelling approach employed to simulate the nonlinear optical processes in the excitonic three-level system.

2.5 Modelling of the excitonic three-level system

To describe the processes occurring in the excitonic three-level system, we use the model according to the schematic shown in fig. 2.23.

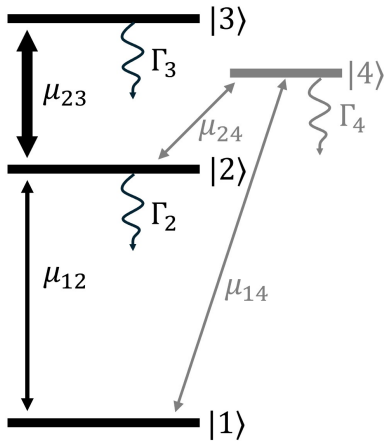

Figure 2.23: Schematic of the excitonic model used to simulate nonlinear processes. $|1\rangle$: ground state; $|2\rangle$: AX; $|3\rangle$: HX. The transition dipole moment μ_{12} is about four times smaller than μ_{23}. Lifetimes Γ_2 and Γ_3 are set to match experimental data. State $|4\rangle$ breaks inversion symmetry, enabling second-order nonlinear processes via weak couplings to $|1\rangle$ and $|2\rangle$. Parameters that show little influence on the results are shown in grey.

The parameters are chosen to reproduce the key experimental observations. The ground state $|1\rangle$ is set to $E_1 = 0\,\mathrm{eV}$. The AX is represented by

$|2\rangle$ at $E_2 = 1.722\,\mathrm{eV}$, and the HX by $|3\rangle$ at $E_3 = 3.426\,\mathrm{eV}$. The transition dipole moment between $|1\rangle$ and $|2\rangle$ is $\mu_{12} = 0.14\,\mathrm{e\,nm}$. To correctly reproduce the SHG power-law exponent and anticrossing behavior, the transition dipole moment between $|2\rangle$ and $|3\rangle$ is set to $\mu_{23} = 0.58\,\mathrm{e\,nm}$, approximately four times larger than μ_{12}. The lifetimes are chosen as $\hbar\Gamma_2 = 0.005\,\mathrm{eV}$ and $\hbar\Gamma_3 = 0.003\,\mathrm{eV}$, consistent with previous experimental results and confirmed by time-resolved nonlinear spectroscopy (section 4.2.1). The dipole moment between $|1\rangle$ and $|3\rangle$ is set to zero, reflecting the fact that the high-lying state is only indirectly observed in nonlinear spectroscopy and not in direct emission. Therefore, we treat $|3\rangle$ as a p-like state that does not couple directly to the ground state [204]. To enable simulation of second-order nonlinear processes, such as SHG, the system must lack inversion symmetry. This is implemented by introducing an additional state $|4\rangle$, which couples weakly to both $|2\rangle$ and $|1\rangle$, with $\mu_{24} = 0.02\,\mathrm{e\,nm}$ and $\mu_{14} = 0.007\,\mathrm{e\,nm}$, respectively. The exact setting of these small values has negligible influence on the results. The lifetime of $|4\rangle$ is set to $\hbar\Gamma_4 = 0.1\,\mathrm{eV}$, and its energy to $E_4 = 3.28\,\mathrm{eV}$. The exact choice of parameters related to $|4\rangle$ does not affect the simulations, given they are not resonant with the excitation pulse energy. The simulation parameters are summarized in table 2.1.

State	E_1		E_2		E_3	E_4
Energy (eV)	0		1.722		3.426	(3.28)
Decay rate (eV)	$\hbar\Gamma_2$		$\hbar\Gamma_3$			$\hbar\Gamma_4$
	0.005		0.003			(0.1)
Transition dipole moment (e nm)	μ_{12}	μ_{13}	μ_{14}	μ_{23}	μ_{24}	μ_{34}
	0.14	0	(0.007)	0.58	(0.02)	0

Table 2.1: Simulation parameters used for the density-matrix model. Values related to state $|4\rangle$ (in parantheses) have little influence on the results.

2.5.1 Influence of excitonic resonances on the SHG power-law exponent

As discussed in section 2.2, the second-order polarization of the SHG is generally expressed as $P(2\omega) = \epsilon_0 \chi^{(2)} E(\omega)^2$. This results in a constant power-law exponent of 2, as the second-harmonic generation signal is proportional to the square of the excitation intensity $I(2\omega) \propto I(\omega)^2$. However, this is only true if the SHG signal is not influenced by any resonances of the material. TMDC monolayers are known to exhibit strong optical nonlinearities due to their broken inversion symmetry, making them the ideal candidate to investigate nonlinear light-matter interaction [205–209]. SHG spectroscopy can be used to identify excitonic resonances in the material, as they result in an enhancement of the SHG signal [144].

When the excitation frequency is close to the energy of an excitonic transition, states become dressed by photons, Rabi oscillations occur and the macroscopic effective susceptibility $\chi^{(2)}$ becomes a function of the Rabi frequency $\Omega_{\text{Rabi}} = \sqrt{(\mu E(\omega)/\hbar)^2 + \Delta^2}$ where μ is the transition dipole moment, $E(\omega)$ is the electric field amplitude of the excitation laser and Δ is the detuning of the excitation frequency from the excitonic resonance. Under strong pumping of excitonic transitions, the energy level will be shifted by the AC-Stark effect [210, 211]. Usually, the energy gap between the two levels will increase for red-detuned pump frequency and decrease for blue-detuned pump frequency. This leads to a power-dependent shift of the excitonic resonance and therefore to a reduction of the resonant enhancement. Consequently, the second-order polarization becomes field strength dependent, leading to a power-law exponent deviating from the trivial value of 2. The AC-Stark shift of excitonic resonances is more complex in the case of an almost degenerate three-level system, as AC-Stark effects of several transitions can counteract.

We choose the deviation of the power-law exponent of the SHG from the trivial value of 2 as the experimental observable. By comparing experimental

data with simulation, we found that the transition dipole moments need to be chosen in a way, such that the transition dipole between state $|2\rangle$ and $|3\rangle$, μ_{23}, is roughly four times larger than the transition dipole coupling ground state $|1\rangle$ to state $|2\rangle$, μ_{12} [190].

In order to investigate the influence of the energetic positions of the excitonic resonances on the power-law exponent, we perform numerical simulations of systems with different energy level positions. The simulated power-law exponents of the SHG signal obtained from a model system for different excitation wavelengths is shown in fig. 2.24. We artificially choose the energy

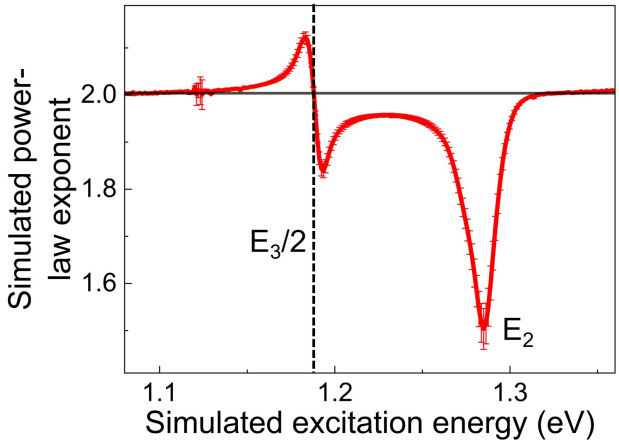

Figure 2.24: Simulated power-law exponent of the SHG signal, obtained for artificially chosen energy levels in a three-level system. The second state $|2\rangle$ is set to 1.285 eV. A saturation of the state results in a reduction of the power-law exponent at this energy. The third state is set to 2.38 eV. Due to shifting of this energy level, a dispersive feature is visible in the power-law exponent. The energy, where the power-law exponent crosses 2, indicates half the energy of the excitonic resonance of state $|3\rangle$. Error bars indicate the quality of the numerical simulation.

states to be far apart in order to investigate the influence of the resonances on the power-law exponent separately. The energy of the second state is set to $E_2 = 1.285\,\text{eV}$. The energy of the third state is set to $E_3 = 2.38\,\text{eV}$. The

dipole moments are set according to table 2.1.

The simulated power-law exponent signal shows characteristic lineshapes for excitonic resonances. The second state $|2\rangle$ can be identified by a saturation, resulting in a power-law exponent smaller than 2. The third state $|3\rangle$ results in a dispersive-shaped feature, that has a power-law exponent larger than 2 for red-detuned excitation and smaller than 2 for blue-detuned excitation. The energy of state $|3\rangle$ is identified by the energy where the dispersive feature crosses the power-law exponent of 2. As the shape of the power-law exponents is a direct consequence of the excitonic resonances, it can be used to determine the material's energetic positions.

The detuning of the energy levels $\Delta E = E_{12} - E_{23} = 2E_{12} - E_{13}$ can either be positive, as in WSe_2, or negative, as in $MoSe_2$. Therefore, we simulate the power-law exponents for very large or small detuning in positive or negative direction, respectively, as shown fig. 2.25. Panel **a** shows the power-law exponent for negative detuning with the two characteristic features, well separated at distinct energy positions. When the detuning is reduced, as shown in panel **b**, the features merge, resulting in a notable 'peak-and-two-dip' shape. For the simulated positive detuning, shown in panel **c** and panel **d**, the shape is inverted. Corresponding experimental data, analysing the lineshapes of power-law exponents, obtained by SHG measurements of different materials is shown in section 4.1.2.

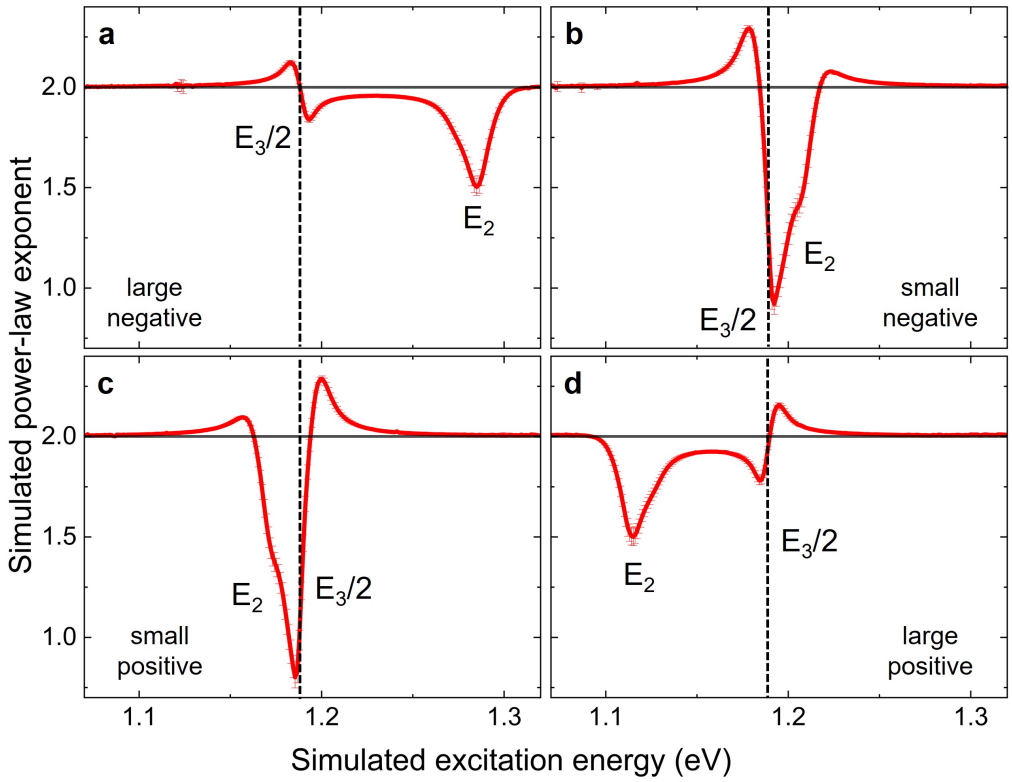

Figure 2.25: Simulated power-law exponent of the SHG signal of three-level systems. The dispersive feature indicating the third state $|3\rangle$ and the saturation of the second state $|2\rangle$ is marked in every graph. **a** The two features are well separated for a large negative detuning ΔE. **b** The features merge into one feature, for a smaller negative detuning. **c** The feature is reversed compared to **b** for small positive detuning. **d** The features are well separated for large positive detuning.

2.5.2 Spectral phase and second-harmonic generation dips

The quantum interference SHG dip is attributed to Rabi oscillations occuring in the three-level system under suitable resonant excitation, as seen in their population dynamics in fig. 2.10. In this chapter, we analyse the spectral properties of simulated SHG signals, in order to obtain information about

the underlying process. The simulated time-dependent polarization $P(\mathrm{t})$ of the system is shown in fig. 2.26**a** for a low-power excitation, corresponding to one quantum interference dip and in fig. 2.26**b** for high-power excitation, corresponding to two quantum interference dips. In both cases, the polarization shows several nodes, which is captured by the Fourier-filtered polarization at the fundamental frequency $P_{\omega}(\mathrm{t})$ leading to the envelope of $P(\mathrm{t})$. By Fourier-space filtering at the SHG frequency, we obtain the small fraction of polarization at the SHG frequency $P_{2\omega}(\mathrm{t})$, which shows only one or two nodes, for low- or high-power excitation, respectively. This analysis makes it intuitive to relate the number of nodes in the time-dependent polarization at the SHG frequency to the number of dips in the SHG spectrum.

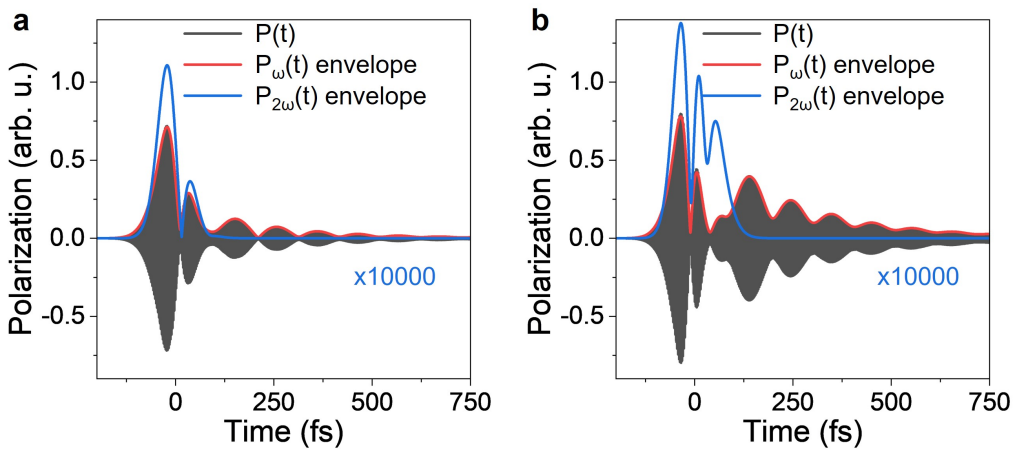

Figure 2.26: Time-dependent polarization (black line) and its envelope (red line) for **a** low-power excitation, resulting in one dip of the SHG spectrum, and **b** high-power excitation, resulting in two dips of the SHG spectrum. The rescaled polarization at the SHG frequency (blue line) only has one or two dips, respectively.

The frequency counterpart of the time-dependent polarization can be analyzed in order to obtain additional information about spectral phase and group delay and their relation to Rabi oscillations. Figure 2.27 shows the

simulated spectrum of a one-dip SHG spectrum in the left column and a two-dip SHG spectrum, obtained for higher excitation power, in the right column. The spectral phase ϕ of both polarizations shows one or two jumps at the energy of the SHG dips, respectively. Consequently, the derivative of the spectral phase, the group delay $\frac{d\phi}{d\omega}$ shows one or two dips at corresponding frequencies.

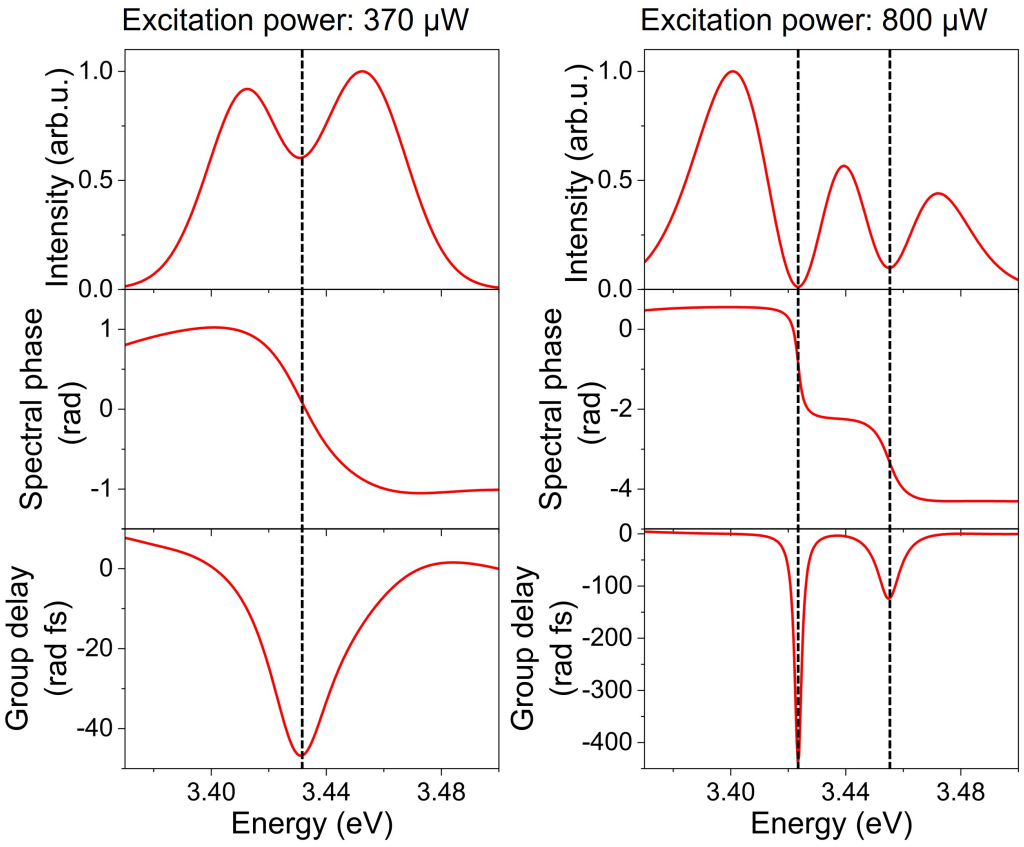

Figure 2.27: Spectral analysis of **left column** low-power-excited SHG spectrum with one dip and **right column** high-power-excited SHG spectrum, showing two dips. The spectral phase shows one or two phase jumps, corresponding to the number of dips. The group delay shows one or two dips, corresponding to the number of dips in the SHG spectrum. Vertical lines are guides to the eye indicating the position of the SHG dips.

This analysis provides intuitive understanding of the suppression mechanism. Frequency components of the SHG dip are only emitted when low excitation power is present, i.e., at the early part of the laser, limiting them to negative group delays. When the power is stronger, in the middle of the laser pulse, Rabi oscillations take place, suppressing emission of corresponding frequency components. This analysis seems to be quite robust and is used to rationalize the chirp-dependent SHG dips in section 4.1.1.

The influence of phase jumps on spectral bifurcation is well-known in literature [212–214]. Here, the spectral phase of the laser can be shaped in a way that the SHG signal of a nonlinear crystal shows a bifurcation at desired wavelengths [212]. The spectral phase can also be tailored in a way that emission of a two-photon allowed transitions is completely suppressed, as a result of destructive interference between photons with different energy in one pulse [213]. Phase jumps cannot only be introduced by tailoring the laser field, but also by the material itself. Therefore, transform-limited pulses are often not ideal for efficient excitation of certain transitions. Laser pulses can be tailored, to optimize the nonlinear light-matter interaction [214].

In our experiments, the phase of the laser field remains uninfluenced, while the unique properties of the excitonic levels in the materials lead to jumps of the spectral phase, resulting in spectral bifurcation.

Having now established the main theoretical concepts of TMDCs, their band-edge excitons, high-lying excitons, and the influence of excitonic resonances on nonlinear optical processes, the implementation of the optical experiments will be discussed in the following chapter.

CHAPTER 3

Measurement techniques

In order to investigate the properties of the materials, various optical measurement techniques are employed. This includes both linear and nonlinear methods. The linear techniques include PL measurements of the band-edge states, as well as UPL measurements of *s*-like HX. The nonlinear techniques are applied to probe *p*-like HX. Experiments using a single-laser excitation are performed to study SHG effects, while FWM and SFG signals are investigated using two laser excitations with a fixed pulse delay. The techniques will be described in the following.

All experiments are carried out by focusing the laser onto a TMDC layer placed inside a cryostat, using an objective integrated into a custom microscope in back-scattering geometry. The emitted light from the sample is collected by the same objective and directed through a beamsplitter, which separates the detection path from the excitation path. The detection path guides the emission into a spectrometer, where it is spectrally dispersed and recorded by a CCD camera. The power of all lasers is carefully monitored and controlled. Throughout this thesis, the corresponding pulse fluence is calcu-

lated and given in parentheses where relevant. Appropriate excitation filters are used to suppress reflected light from the excitation laser. A schematic overview of the general setup is shown in fig. 3.1.

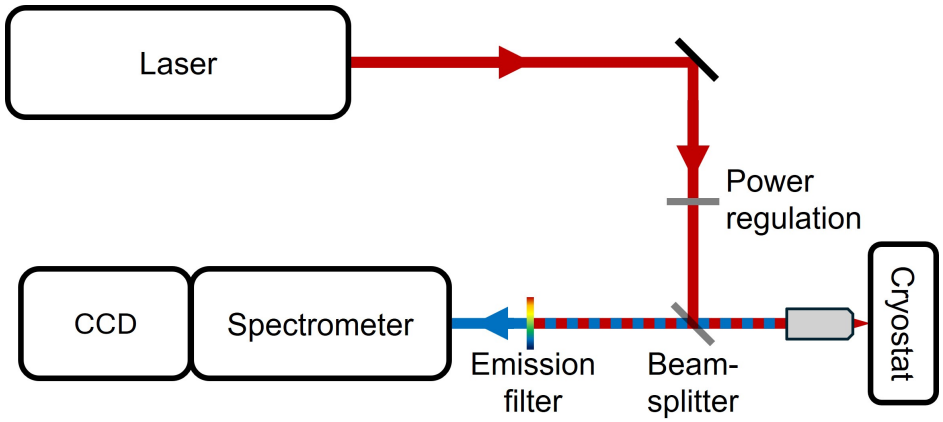

Figure 3.1: Schematic illustration of the measurement setup. Laser radiation is directed through a microscope objective onto a sample held in a cryostat at cryogenic temperatures. The power of each laser is precisely controlled. The emitted light is collected by the same objective and passes through a beamsplitter, which separates the excitation path (red) from the emission path (blue). The emission is filtered to suppress reflected excitation light, dispersed in a spectrometer, and detected by a CCD camera. This setup is used for all experiments in this work, with minor modifications as required for specific measurement techniques.

The following sections describe the measurement techniques and the adjustments to the setup, as required by each technique.

3.1 Photoluminescence spectroscopy

The materials investigated in this work exhibit a direct bandgap in the visible spectral range, with energies between 1.1 eV and 2.1 eV and binding energies on the order of several 100 meV [33, 38, 141–144, 153]. For PL excitation, the photon energy needs to exceed the optical bandgap. Therefore, a CW

solid-state laser (*Coherent Sapphire 488 SF NX*) with a fixed wavelength of 488 nm and a maximum output power of 100 mW is used. Typically the power used for PL is on the order of 1 µW to 100 µW

Under resonant excitation of the AX, the electron density in the corresponding state can be increased to a level where Auger recombination becomes significant. In this non-radiative process, the energy of one electron is transferred to another, promoting the latter to a higher conduction-band state. The upconverted electron can then recombine radiatively with a hole in the valence band, emitting a photon with the energy corresponding to the higher-lying state. This UPL process is used in this work to investigate *s*-like HX.

The most efficient way to induce Auger recombination is by using a CW laser resonant with the AX. This approach maintains a constant electron density in the conduction band, in contrast to pulsed excitation, which tends to enhance exciton-exciton annihilation and thereby suppress the Auger process. For the investigation of HX in WSe_2 and $MoSe_2$, a Ti:sapphire CW laser (*Sirah Matisse CR*) with a tuning range of 680 nm to 1020 nm and a maximum power of 2 W is used. To investigate the temporal dynamics of the *s*-like HX using a streak camera, pulsed excitation is required. For this purpose, a *Coherent Chameleon Ultra II* laser is employed, offering a tuning range from 680 nm to 1080 nm and a maximum output power of 4 W. The laser delivers pulses with a duration of 140 fs at a repetition rate of 80 MHz. Typically, the power used for UPL is on the order of 100 µW to 3 mW.

3.2 Second-harmonic generation

To efficiently generate SHG signals, a sufficiently large electric field is required, which can be achieved using pulsed lasers with high peak power. In this work, SHG is investigated under resonant excitation of excitonic transitions, which imposes specific requirements on the excitation wavelength.

For this purpose, a *Spectra-Physics MaiTai BB* laser is employed, delivering pulses with a duration of 80 fs at a repetition rate of 80 MHz. The laser provides a spectral tuning range from 710 nm to 990 nm and a maximum output power of 1.5 W. To extend the accessible excitation range, the *Coherent Chameleon Ultra II* is used to pump an optical parametric oscillator (OPO) (*APE OPO-X fs*), enabling wavelength coverage from 505 nm to 730 nm, at a repetition rate of 80 MHz. This extended range allows resonant access to a broader set of excitonic transitions in the investigated materials. Usually powers between 500 µW (200 µJ cm^{-2}) and 3 mW (1200 µJ cm^{-2}) are used for SHG measurements.

3.3 Pump probe experiments with two-laser excitation

In this work, the nonlinear response of the material under illumination with two intense laser pulses is investigated. We measure the delay-time-dependent SFG and FWM signals. One laser frequency is in or close to resonance with real excitonic transitions. For this experiment, the *Chameleon* and the *OPO* are used, as they emit synchronized radiation. The temporal delay is adjusted by a mechanical delay line.

In order to guide radiation from two different laser sources onto the same optical path way, a 50:50 beamsplitter is used. This reduces the power of each laser by half, which is generally no problem in the given configuration. Furthermore, we use the residual radiation from the beamsplitter to employ a novel technique, to determine the temporal overlap of the two laser pulses with high precision during the experiment, limiting errors introduced by instabilities in the setup. The fraction of both lasers that is not exciting the sample is guided onto a beta barium oxide (BBO) crystal, widely used in nonlinear wave-mixing applications due to its high nonlinear coefficients [215], and set to the phase-matching condition of the SFG signal of the two laser

beams. The generated SFG signal is detected with a photodiode. With a bandgap exceeding 6 eV, BBO is a suitable candidate for non-resonant SHG studies in the red and near-infrared spectral range [145]. As parametric nonlinear processes are highly dependent on the intensity of the exciting lasers, the SFG signal reaches maximum if the two laser pulses overlap temporally.

To find the zero delay time of both lasers we place a second BBO in the cryostat, next to the sample. To achieve phase-matching conditions over a broad range of fundamental wavelengths without rotating the crystal, a thin BBO plate, cut at 29.2° with thickness of 100 µm, is employed, making conversion efficiency insensitive to wavelengths. The SFG signal of the two lasers, generated in the BBO, is detected by the spectrometer. We compare the time-dependent intensity of the SFG signal for both BBO crystals in order to calibrate the setup for every wavelength combination used.

3.4 Technical implementation

In this section, the technical implementation of the general setup shown in fig. 3.1 is described. The investigated samples are mounted in a continuous-helium-flow cryostat (*Janis, ST-500* or *Cryovac, Konti Micro*), which can be operated at temperatures from 4 K to 300 K. The cryostat is mounted on an *xy*-stage. The lasers are focused onto the sample by an objective (*OLYMPUS LUCPLFLN 40X/0.6*) mounted on a *z*-stage. The emitted light is collected by the same objective and passes through a non-polarizing 50:50 beamsplitter (*Thorlabs BSW26R*). The light then passes through a filter to block the excitation light. Several filters are used depending on the requirements of the different experiments. This includes, in particular, a *Semrock RE 488 LP* for PL measurements and a *Semrock FF01-680/SP25* for UPL and nonlinear wave-mixing experiments. The signal is then focused into a spectrometer (*Princeton Instruments Acton SP2300*) with a rotatable grating turret equipped with gratings of 150 $\frac{1}{\text{mm}}$, 600 $\frac{1}{\text{mm}}$, and 1200 $\frac{1}{\text{mm}}$. The spectrum is de-

tected by a CCD camera (*Princeton Instruments PIXIS 100*). To investigate the temporal dynamics of the *s*-like HX, a *Hamamatsu Universal Streak Camera* with time resolution of approximately 5 ps is used instead of the CCD. The power of the lasers is measured by a photodiode (*Thorlabs S120VC*) and controlled by a power-regulation based on a computer-controlled neutral density filter wheel (*Thorlabs NDC-100C-4*). Imaging of the sample inside the cryostat is achieved by replacing the spectrometer with a CMOS camera (*Hamamatsu ORCA-Flash4.0*), allowing for easy sample navigation and laser focusing. When passing through optical media, the pulsed lasers acquire chirp. To compensate for this, a prism compressor is used.

The aforementioned devices will be explained in detail in the following sections.

3.4.1 Streak camera

In order to investigate the temporal dynamics of the emitted signals, the CCD camera is replaced by a universal streak camera. The emitted photons are first dispersed in a grating spectrometer and then directed onto a photocathode, which emits electrons when hit by photons. These electrons are accelerated and pass through a streak tube, containing a pair of deflection plates. The AC electric field is varied sinusoidally in synchronisation with the repetition rate of the laser. Consequently, electrons arriving earlier experience a smaller electric field strength than those arriving later. This results in a spatial deflection of the electrons depending on their time of emission. The electrons are subsequently collected on a phosphor screen at the end of the streak tube, generating radiation that is recorded by a sCMOS camera and thereby providing both temporal and spectral information.

3.4.2 Titanium-sapphire laser

Since its discovery as a vibronic laser material in 1982, titanium-doped sapphire (Ti:Sa) has become the workhorse of near-infrared laser spectroscopy. Owing to its broad absorption peak around 500 nm, it can be efficiently pumped in the green spectral range using high-intensity argon-ion lasers or frequency-doubled neodymium-doped yttrium aluminum garnet (Nd:YAG) lasers [216]. Ti:Sa exhibits a broad emission spectrum spanning from 650 nm to 1100 nm, enabling the generation of laser light in both the red and near-infrared regions. Through mode-locking, a fixed phase relationship between the longitudinal cavity modes is established, resulting in the formation of ultrashort pulses in the time domain. In Ti:Sa lasers, this is most commonly achieved via Kerr-lens mode locking, where the intensity-dependent refractive index of the gain medium acts as an ultrafast saturable absorber. This allows the generation of pulsed laser radiation with typical repetition rates in the range of 70 MHz to 90 MHz and pulse durations from 10 fs to 10 ps. By incorporating wavelength-selective elements such as birefringent filters or etalons, the spectral bandwidth can be narrowed, enabling CW laser operation.

3.4.3 Optical parametric oscillator

An optical parametric oscillator (OPO) uses a nonlinear crystal to convert the energy of a pump laser into light at different frequencies. In our case, the high-energy pump wave ω_p, generated by the *Chameleon* laser, is directed into a nonlinear crystal, where it is converted into two lower-energy output waves, the idler ω_i and the signal ω_s. The sum of the energies of the idler and signal waves is equal to the pump energy:

$$\hbar\omega_\mathrm{p} = \hbar\omega_\mathrm{i} + \hbar\omega_\mathrm{s} \tag{3.1}$$

The photons circulate within an optical cavity. For efficient energy transfer, the waves must conserve momentum and remain in phase over each round trip, known as the phase-matching condition:

$$n_{\mathrm{p}}\omega_{\mathrm{p}} = n_{\mathrm{i}}\omega_{\mathrm{i}} + n_{\mathrm{s}}\omega_{\mathrm{s}} \tag{3.2}$$

Since the refractive index n generally varies with wavelength, fulfilling this condition is challenging. Here, the birefringent properties of crystals come into play, as differently polarized beams exhibit different refractive indices. In principle, this could allow complete conversion of the pump beam into signal and idler beams, which is never achieved in practice.

The system used in this work, the *APE OPO-X fs*, employs a technique known as periodic poling. A periodically poled crystal begins as a bulk crystal in which alternating regions are poled in opposite directions. This is achieved by applying a high electric field to selected regions. The stripe width is precisely controlled, such that the pump beam's phase is shifted by 180° in one stripe and then reversed in the next, bringing it back into phase with the signal or idler beam. This creates a quasi-phase-matching condition. In our system, the crystal's stripe periodicity is continuously varied, enabling phase matching over a spectral range of several hundred nanometers.

Additionally, the pump and signal pulses must overlap temporally within the nonlinear crystal, to obtain optimal conversion efficiency. This is achieved by introducing a heavy flint glass element into the cavity, allowing independent adjustment of the optical path length for each wavelength.

Once the signal beam is generated, an intracavity SHG stage is used to produce its second-harmonic in an additional nonlinear crystal. Phase matching in this stage is achieved by adjusting both the temperature and the rotation of the crystal.

3.4.4 Setup modifications for ultraviolet detection

To reduce surface reflections and enhance the performance of optical elements, special coatings are applied to their surfaces. Together with the choice of optical material, these coatings define the usable spectral range of each element. This limitation becomes particularly relevant in the present work when investigating the SHG signal of sulfur-based TMDCs under resonant excitation of their AX.

Components through which both the fundamental and second-harmonic radiation must pass simultaneously are especially critical and, in several cases, require replacement. The transmissive objective is replaced with a reflecting objective *(Beck Optronics Solutions 5004)* offering a magnification of 36 and a numerical aperture of 0.5. The beamsplitter, separating the excitation and detection paths, is substituted with a D-shaped mirror *(Thorlabs PFD05-03-P01)*. For emission filtering, a colored-glass bandpass filter *(Thorlabs FGUV11)* is employed.

3.4.5 Controlling chirp with a prism compressor

Due to the uncertainty principle, limiting a signal in time requires it to be spread in frequency. If all frequency components are in phase, the pulse is transform-limited. However, when traveling through optical dense media, the frequency components experience different phase delays due to the wavelength-dependent refractive index of the medium, resulting in a chirped pulse. For common substrates used in optical components, such as fused silica, longer wavelengths travel faster through the medium, leading to positive group delay dispersion (GDD), also referred to as glass-like chirp. Chirp is often an unwanted feature, as it broadens the pulse in time and reduces its peak power. Furthermore, a non-transform-limited pulse can behave in a complex manner, leaving the pulse structure uncontrolled. However, chirp can be used to amplify high-intensity laser pulses by chirped pulse amplifi-

cation [217]. In general, it is important to control the chirp of pulsed laser sources. This can be achieved using optical elements that introduce negative GDD, such as chirped mirrors, or setups consisting of dispersive elements like gratings or prisms.

In this work, we demonstrate that chirp can serve as an interesting tuning parameter to investigate material properties. Several setups to control the chirp can be used. Here, we modify a common setup, consisting of four prisms, which is seen in fig. 3.2.

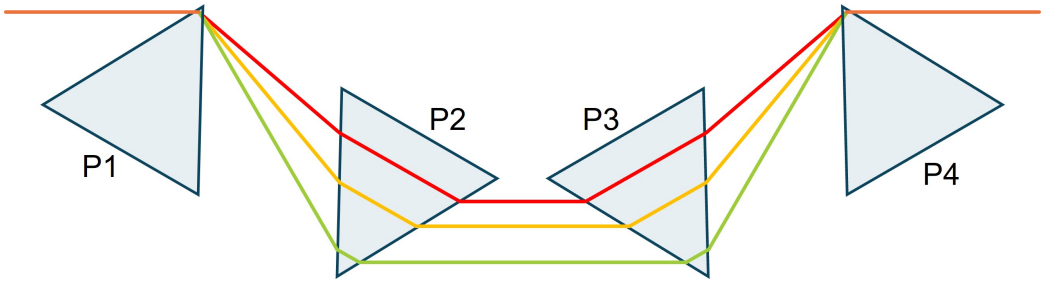

Figure 3.2: Schematic setup of a four-prism arrangement to control chirp. The laser travels from left to right through 4 prisms (P1 to P4). The distance between P1 and P2 is adjusted to control the chirp.

As an ultrafast laser, consisting of a broad range of frequency components, passes through the first prism (P1), the different frequency components are dispersed. This causes them to travel different path lengths between P1 and P2, resulting in different points of incidence on P2. The specific arrangement of the prisms leads to shorter path lengths for lower-frequency components, producing positive, glass-like chirp. Two competing processes in P2 are used to adjust the chirp. The lower-frequency components of the laser pulse travel a longer distance through the optically dense medium but move faster due to their lower refractive index. Depending on the optical path length, they can either gain or lose phase relative to the higher-frequency components. The optical path length is adjusted by changing the point of incidence on P2, which is controlled by varying the distance between P1 and P2. Prisms P3

and P4 are used to compensate for dispersion and to spatially recombine the frequency components. P3 introduces the same amount of chirp as P2.

As it is challenging in practice to construct the setup so that the action of P1 and P2 is completely reversed by P3 and P4, the arrangement is often simplified by replacing P3 and P4 with a mirror folding the beam back through P2 and P1. This modification also reduces the spatial requirements and the need for expensive components. In this work, the setup is further reduced to a one-prism arrangement, as shown in fig. 3.3.

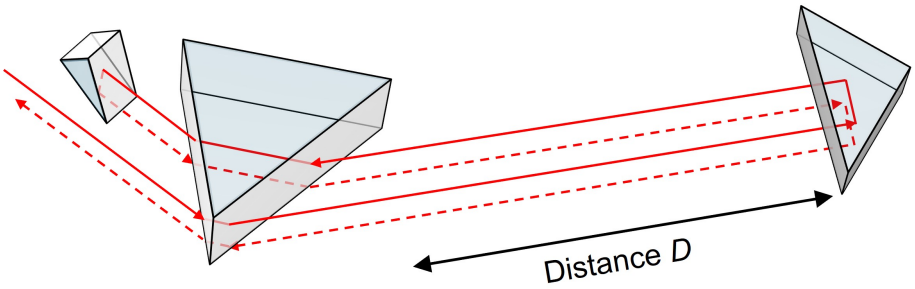

Figure 3.3: Schematic setup of a one-prism arrangement to control the chirp. The direction of beam propagation is indicated by arrows along the red line. The laser pulse passes through the prism four times, with horizontal and vertical displacements achieved by two roof mirrors. The different optical paths of the incoming and outgoing beams make it straightforward to separate them for further use.

The physical working principle of the one-prism setup is comparable to that of the four-prism setup. The laser passes through the prism four times. First at the apex on the upper side of the prism. Then, after horizontal displacement by a half mirror, a second time at the back side on the upper section. Next, after vertical displacement by a second roof mirror, a third time at the back side on the lower section and finally, after horizontal displacement by the first roof mirror, a fourth time at the apex on the lower side of the prism. The compensated beam exits at a lower height, allowing

it to be guided into the setup. The chirp is easily adjusted by changing the distance between the prism and the first roof mirror.

We use a prism made of highly dispersive material (*Thorlabs AFS-SF14*) and silver-coated roof mirrors (*Thorlabs GRS1015-P01*). The maximum distance between the prism and the roof mirror is 50 cm.

To characterize the setup, we perform autocorrelation measurements of the *MaiTai* laser at 726 nm using an industrial autocorrelator (*APE Pulsecheck*). The autocorrelation signals for two representative positions are shown in fig. 3.4. One should note that the FWHM of the Gaussian autocorrelation signal is larger than the actual pulse duration $\Delta\tau$ by a factor of $\sqrt{2}$ [218]. First, we determine the transform-limited pulse duration of the laser. The

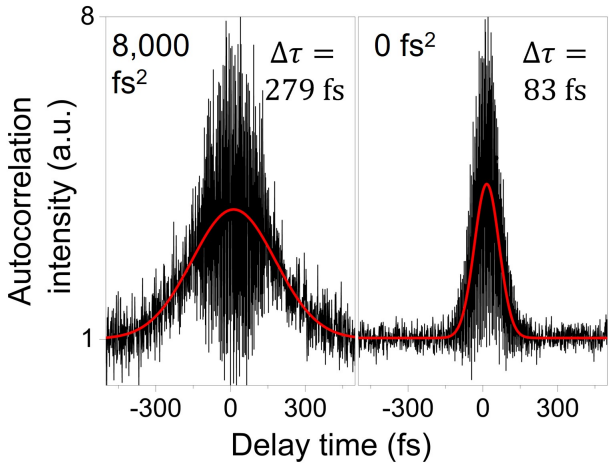

Figure 3.4: Autocorrelation signal of the *MaiTai* laser at 726 nm for two different distances between the prism and the roof mirror. The signal on the left corresponds to a distance of 300 mm, showing a broadened pulse with 8000 fs^2 GDD. The signal on the right corresponds to a distance of 140 mm, showing a transform-limited pulse with 0 fs^2 GDD.

lowest measured value of 83 fs is obtained at a distance of 140 mm between the roof mirror and the prism. For transform-limited Gaussian-shaped laser pulses, the time-bandwidth product (TBP), defined as the product of the

FWHM of the pulse duration $\Delta\tau$ and spectral FWHM $\Delta\nu$, is constant [218]:

$$TBP = \Delta\nu\Delta\tau = \frac{2\log 2}{\pi} = 0.441 \tag{3.3}$$

We measure the spectral width of the laser in wavelength and convert it to frequency for a fixed center wavelength λ using:

$$\Delta\nu = \frac{c\Delta\lambda}{\lambda^2} \tag{3.4}$$

In our experiment, the measured spectral width of the laser is $\Delta\lambda = 9.7\,\text{nm}$ at center wavelength 726 nm, which corresponds to the transform-limited pulse duration $\Delta\tau = 83\,\text{fs}$, which confirms the specified value of the laser system.

We measure the pulse duration of the laser at various distances between the prism and the roof mirror. The magnitude of the chirp, referred to group-delay dispersion (GDD), is calculated using the following formula [219] as:

$$GDD = \frac{1}{4\log 2}\sqrt{\left(\frac{TBP\cdot\Delta\tau}{\Delta\nu}\right)^2 - \left(\frac{TBP}{\Delta\nu}\right)^4}. \tag{3.5}$$

One can compute that the unit of the GDD is fs^2. From the physics of a prism compressor, as discussed earlier, one can assume that positive GDD is introduced for shorter distances, while negative GDD occurs at larger distances.

It can be shown that the GDD varies linearly with the distance between the prism and the roof mirror [220], which can be seen in fig. 3.5. Our setup can introduce GDD values ranging from $8000\,\text{fs}^2$ to $-13\,000\,\text{fs}^2$. The asymmetry in the achievable GDD range originates from spatial constraints in the setup.

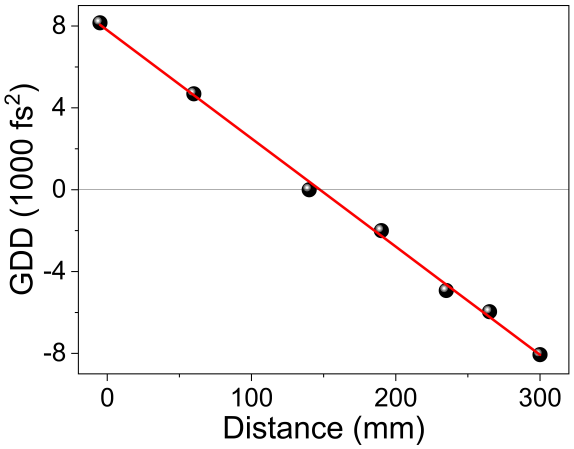

Figure 3.5: GDD of the chirp-control-setup as a function of the distance between the prism and the first roof mirror. The transform-limited pulse duration is obtained at 140 mm. GDD is positive for distances below 140 mm and negative for distances above 140 mm. A linear fit is shown in red.

The chirp-controlling prism arrangement is employed in two parts of this work: in section 4.1.1, to investigate the influence of chirp on the quantum interference of SHG signals, and in section 4.2.1, to minimize chirp and obtain transform-limited pulses for studying the temporal dynamics of HX.

With this fundamental understanding of the optical measurement techniques, and their technical implementations, the key experimental findings of this work will be presented in the following chapters.

CHAPTER 4

Experimental results

The conducted experiments in this thesis can be divided into two parts. The first part addresses the energetic landscape of HXs. We investigate the lifted degeneracy of the three-level system in WSe_2 using nonlinear spectroscopy under chirped-laser excitation. Furthermore, we explore HX species in monolayers TMDCs, including WS_2, MoS_2, $MoSe_2$ and $MoTe_2$. For this, we employ linear spectroscopy techniques such as UPL, as well as nonlinear techniques like SHG and the analysis of the corresponding power-law exponent.

The second part focuses on the temporal dynamics of HX. We use delay-time-dependent two-laser experiments to determine the lifetime of *p*-like HX in WSe_2 by SFG and FWM. Finally, we study the temporal dynamics of *s*-like HX in WSe_2, generated by UPL by means of streak camera measurements.

4.1 Mapping of high-lying excitonic energy levels

A characteristic feature of HX in WSe_2 is the presence of a three-level system, comprising the ground state, the AX, and the *p*-like HX [190]. An *s*-like HX has also been reported [201, 202]. This chapter examines the physical consequences of the three-level system and demonstrates that the occurrence of HX species is a general phenomenon in semiconducting TMDCs.

4.1.1 Chirp-dependent bifurcation of second-harmonic generation signal

The energy of the *p*-like HX can be determined by measuring the energetic position of a dip observed in SHG measurements when excited at half the energy of the HX. It turns out that the three-level system in monolayer WSe_2 is not completely degenerate: The energy separation between the ground state and the AX, E_{12}, is slightly larger than the separation between AX and HX, E_{23}. We define the energy offset as

$$\Delta E = E_{12} - E_{23} = 2E_{12} - E_{13}. \tag{4.1}$$

In the case of our hBN-encapsulated monolayer WSe_2, the offset is 36 meV, which is comparable to previously reported values [202]. The spectral FWHM of a Gaussian-shaped 80 fs pulse with a central energy at 1.708 eV is 23 meV, on the same order of magnitude as the offset. This makes it promising to investigate effects arising from the reordering of spectral components within the pulse on the SHG resonance dip.

To ensure that chirping the laser does not induce unwanted effects to the spectrum, we first conduct control measurements on the well-known nonlinear material BBO. We measure the SHG signal from the BBO crystal at

a fixed excitation energy of $E_{\mathrm{exc}} = 1.708\,\mathrm{eV}$ and excitation power of 1 mW ($400\,\mu\mathrm{J\,cm^{-2}}$) for different chirp values. The normalized SHG response is presented in fig. 4.1. As expected for non-resonant SHG, the spectral profile remains unaffected by chirp. However, the signal-to-noise ratio decreases at large absolute chirp values, which can be attributed to the reduction in peak intensity for chirped pulses. The interference fringes observed in the SHG signal arise from reflections at the surfaces of the thin BBO crystal.

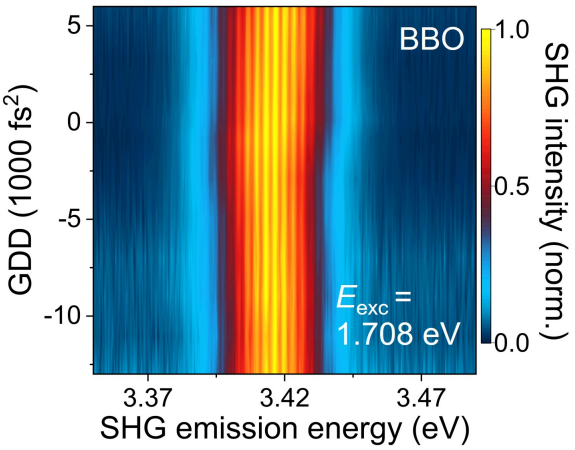

Figure 4.1: Chirp-dependent normalized SHG signal from a BBO crystal at a fixed excitation energy of 1.708 eV and excitation power of 1 mW ($400\,\mu\mathrm{J\,cm^{-2}}$). The SHG response is unaffected by the chirp. The interference fringes arise from reflections at the surfaces of the thin BBO crystal.

A measurement with identical experimental parameters is subsequently performed on a WSe_2 monolayer, encapsulated in hBN at cryogenic temperatures. The chirp-dependent normalized SHG signal at a fixed excitation energy of $E_{\mathrm{exc}} = 1.708\,\mathrm{eV}$ and excitation power of 1 mW ($400\,\mu\mathrm{J\,cm^{-2}}$) is shown in fig. 4.2. At $0\,\mathrm{fs}^2$, the signal exhibits the well-known anticrossing feature associated with two-photon resonant excitation of E_3 [190, 202]. This anticrossing feature persists for positive chirp values up to $6000\,\mathrm{fs}^2$. For negative chirp values below $-3000\,\mathrm{fs}^2$ a second dip emerges on the high-energy

side of the spectrum. When the chirp is reduced beyond $-7000\,\mathrm{fs}^2$, the middle branch of the signal diminishes in intensity, while the other branches become dominant.

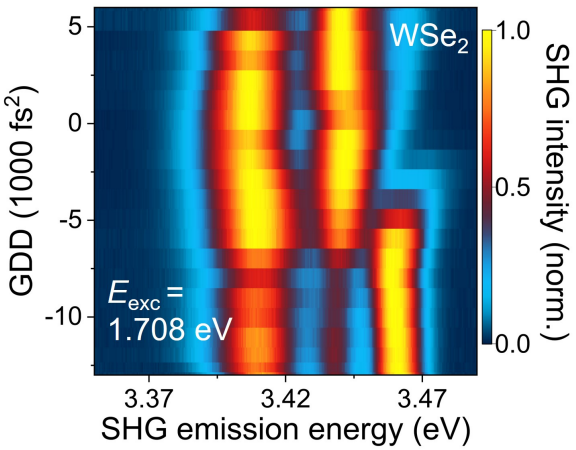

Figure 4.2: Chirp-dependent normalized SHG signal from a WSe_2 monolayer at a temperature of 5 K,a fixed excitation energy of 1.708 eV and excitation power of 1 mW($400\,\mu\mathrm{J\,cm}^{-2}$). The SHG response varies with the chirp value. The well-known anticrossing feature at $0\,\mathrm{fs}^2$ is clearly visible and remains unchanged for positive chirp values. For negative chirp values below $-3000\,\mathrm{fs}^2$, a second dip occurs on the high-energy side of the spectrum. At values below $-7000\,\mathrm{fs}^2$, the middle branch decreases in intensity, while the other branches dominate the signal.

Clearly, the chirp of the resonant excitation laser field influences the SHG response of the WSe_2 monolayer.

To further examine the influence of chirp on the three-level system, we perform excitation-energy-dependent measurements of the SHG signal for various chirp values: The center photon energy of the laser, corresponding to the y-axis, is varied from 1.687 eV to 1.729 eV, while the excitation power is held constant at 1 mW ($400\,\mu\mathrm{J\,cm}^{-2}$). The x-axis corresponds to the detected photon energy, where a single measurement results in an emission spectrum plotted against the bottom axis. Measurements are conducted for chirp val-

ues of $-8000\,\mathrm{fs}^2$, $-4500\,\mathrm{fs}^2$, $0\,\mathrm{fs}^2$, $4500\,\mathrm{fs}^2$, and $8000\,\mathrm{fs}^2$. The resulting data, normalized to the maximum of the SHG signal, are presented in fig. 4.3. As

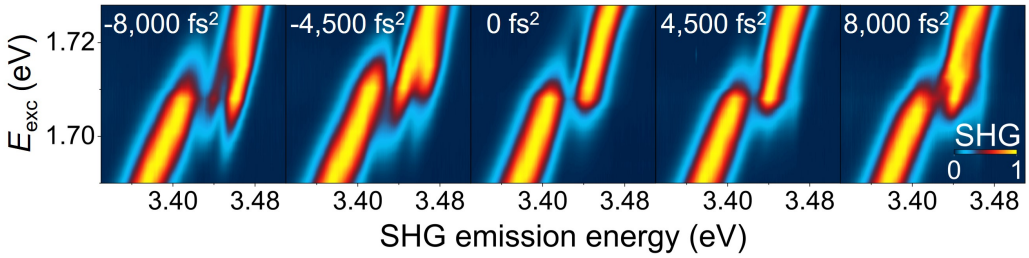

Figure 4.3: Excitation-energy-dependent normalized SHG signal from monolayer WSe_2 for different chirp values of the laser pulse, ranging from $-8000\,\mathrm{fs}^2$ (left) to $8000\,\mathrm{fs}^2$ (right). The characteristic anticrossing dip is dependent on the chirp of the excitation pulse.

expected, all graphs exhibit a standard Gaussian-shaped SHG signal at high and low excitation-energies, consistent with non-resonant excitation of the system. At $0\,\mathrm{fs}^2$ chirp, the signal displays the well-known anticrossing feature, indicating the two-photon resonance of the third state $|3\rangle$. Experimentally, the number of dips increases with decreasing chirp value. At $-4500\,\mathrm{fs}^2$, a second dip emerges on the high-energy side of the spectrum, while the energy of the first dip remains constant. This second dip becomes more pronounced at $-8000\,\mathrm{fs}^2$. In contrast, positive chirp values only slightly modify the signal: at $4500\,\mathrm{fs}^2$ a single dip is observed, which is also present at $8000\,\mathrm{fs}^2$. Here, the signal exhibits slight modulation, which could be attributed to a reduction of peak intensity of the laser pulse.

To further validate these experimental findings, we perform density-matrix calculations as described in section 2.3. We simulate the SHG signal for different central energies of a Gaussian-shaped electric field, incorporating chirp into the pulse to match experimental conditions. The resulting simulated data, shown in fig. 4.4, presents the normalized intensity at the SHG signal energy as a function of the central excitation energy for chirp values of $-8000\,\mathrm{fs}^2$, $-4500\,\mathrm{fs}^2$, $0\,\mathrm{fs}^2$, $4500\,\mathrm{fs}^2$, and $8000\,\mathrm{fs}^2$. The simulated data show

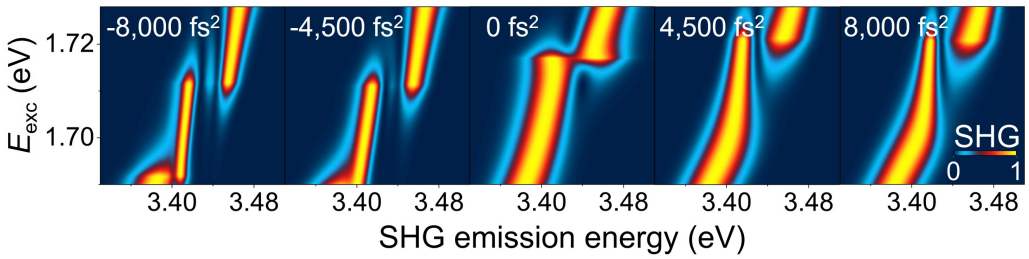

Figure 4.4: Simulation of quantum-interference effects in the SHG signal for various chirped excitation fields using a density-matrix formalism. The normalized SHG intensity is shown as a function of emitted photon energy and central excitation energy for chirp values ranging from $-8000\,\mathrm{fs}^2$ (left) to $8000\,\mathrm{fs}^2$ (right). For unchirped and positively chirped excitation, only one anticrossing feature is present, whereas a second interference dip emerges for a negatively-chirped pulse, in good agreement with the experimental data.

similar features as the experimental results. At $0\,\mathrm{fs}^2$, the anticrossing feature is observed, indicating a single Rabi oscillation between the second state $|2\rangle$ and the third state $|3\rangle$. For negative chirp values of $-4500\,\mathrm{fs}^2$, a second dip appears, becoming more pronounced at $-8000\,\mathrm{fs}^2$. In contrast, signals at $4500\,\mathrm{fs}^2$ and $8000\,\mathrm{fs}^2$ exhibit only a single dip.

The simulation also shows differences compared with the experiment results: the energies of the dips are not constant. These energy-shifts could be attributed to AC-Stark effects of the laser field, which could be reasonable for high-power excitation of resonances, but seem to be underrepresented in the experimental results.

Density-matrix simulations in previous studies have shown that a dip in the SHG signal can be attributed to a Rabi oscillation between states $|2\rangle$ and $|3\rangle$, with the number of dips corresponding to the number of Rabi oscillations. This can be achieved by either increasing the temporal pulse width or the electric field strength [190]. To explain the asymmetry with respect to the sign of the chirp values, we consider the spectral shape of the electric-field pulse and compare it with the simplified band structure of the underlying

three-level system. The corresponding schematic is shown in fig. 4.5.

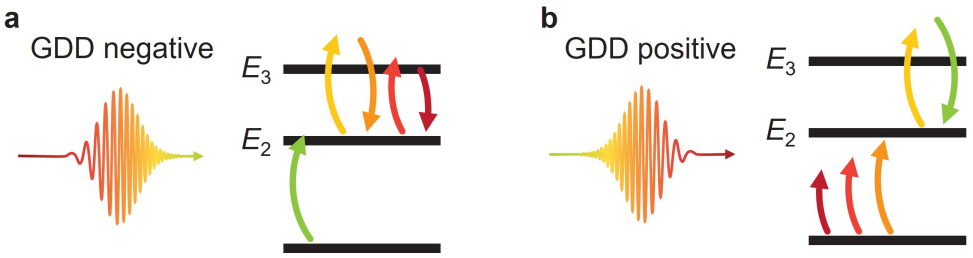

Figure 4.5: Simplified band structure of the three-level system in monolayer WSe_2. **a** For excitation with a negatively chirped pulse, the second state $|2\rangle$ is populated during the initial part of the femtosecond pulse, leaving sufficient time to induce two Rabi oscillation between $|2\rangle$ and $|3\rangle$. **b** In contrast, in a positively chirped pulse, the low-energy photons arriving first are of insufficient energy to populate $|2\rangle$. Only the later, higher-energy photons can drive the transition, and the remaining pulse duration permits only a single Rabi oscillation.

In the schematic, the two Gaussian-shaped electric-field pulses provide a simplified depiction of chirped laser pulses. The pulse in panel **a** represents a negative chirp, where high-energy photons (indicated in green) arrive first at the material. Lower-energy photons (indicated in red) arrive later. The high-energy photons are sufficient to populate the second state $|2\rangle$ during the initial part of the pulse. Due to the lifted degeneracy in the system, the low-energy photons can then drive Rabi oscillations between $|2\rangle$ and $|3\rangle$. As the chirp stretches the pulse in time, sufficient time after the high-energy photons allows for two Rabi oscillations between these states.

A positively-chirped pulse, drawn in panel **b** exhibits the opposite behavior. Low-energy photons (indicated in red) arrive first at the material, while high-energy photons (indicated in green) arrive later. The energy of the low-energy photons is insufficient to populate the second state $|2\rangle$. Only the later-arriving high-energy photons can drive the transition, leaving a pulse duration that permits only a single Rabi oscillation.

This explanation is supported by analyzing the time- and frequency-dependent polarization, obtained by density-matrix simulation, as shown in fig. 4.6. The time-dependent polarization for both negative and positive

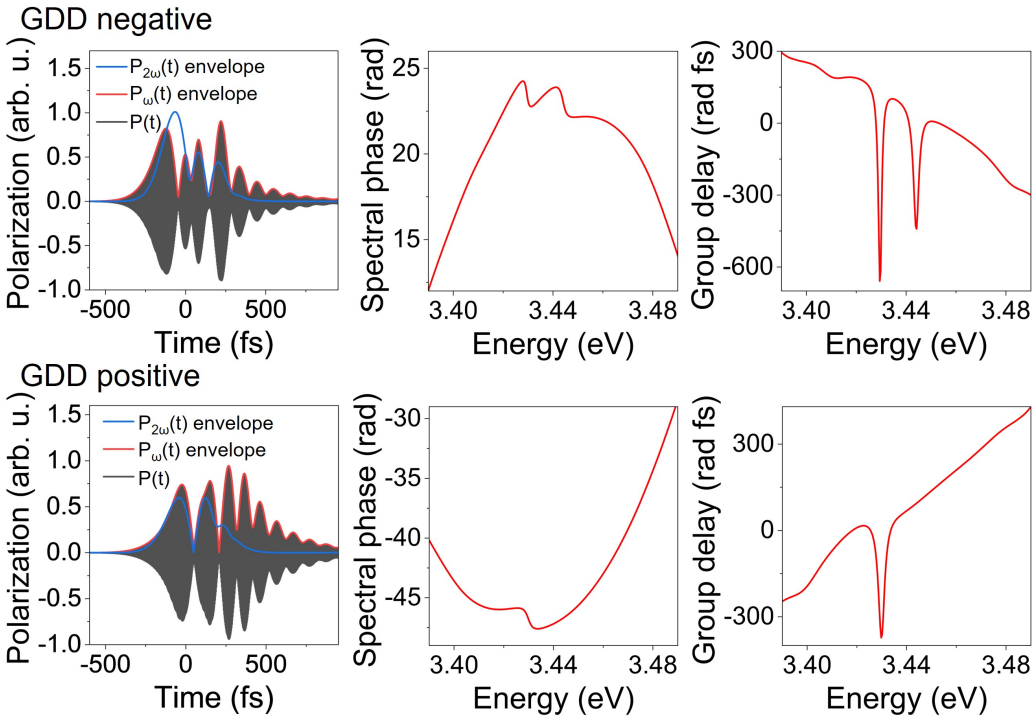

Figure 4.6: Analysis of the temporal polarization, calculated for **top row** negative chirp and **bottom row** positive chirp. The time-dependent polarization shows complex behavior, with many nodes. The Fourier-filtered polarization at the SHG frequency shows only two nodes or one node for negative or positive chirp, respectively. The analysis of the spectral phase and group delay of the frequency-dependent polarization reveals two jumps in the spectral phase or two dips in the group delay for negative chirp, indicating two Rabi oscillations. For positive chirp, signatures of only one Rabi oscillation are visible. The global curvature of the spectral phase results from the chirped excitation.

chirped laser fields shows a complex oscillatory behavior. The Fourier-filtered polarization at the SHG frequency reveals two prominent oscillations for neg-

ative chirps, while positive GDD results only in one oscillation. Comparable behavior can be seen in the spectral phase and group delay of the SHG signal. Negative chirp results in two spectral phase jumps and two dips in the group delay. A positive chirp reveals only one jump and one dip in the group delay. The spectral phase shows a curvature on larger frequency scales as a result of the chirped excitation.

In this experiment, we demonstrated that chirp is a powerful tool for probing the offset of the energetic landscape of HXs in monolayer WSe_2. We perform density-matrix calculations that rationalize our experimental findings. Further insight is gained by analyzing the simulated polarization, justifying the assignment of Rabi oscillations, responsible for quantum interference dips.

A logical follow-up experiment would be the investigation of a negatively detuned system, where the energy difference between state $|1\rangle$ and state $|2\rangle$ is smaller than the energy difference between $|2\rangle$ and $|3\rangle$. In such a case, one expects a second dip in the SHG signal to appear for positive chirp values. However, materials exhibiting negative offset, such as monolayer $MoSe_2$ or WS_2, do not display a split SHG signal, as we demonstrate in section 4.1.2.

4.1.2 High-lying excitons in different semiconducting transition metal dichalcogenides

As noted earlier, most publications on HX have focused on WSe_2, with only limited studies extending to $MoSe_2$. However, the general similarities in the band structures of monolayer semiconducting TMDCs such as WS_2, MoS_2, and $MoTe_2$ suggest that their energetic landscapes of HX should be comparable to that of WSe_2, making them suitable candidates in the search for signatures of these states.

In this chapter, we present the results of our investigation of HX in monolayers of WS_2, MoS_2, $MoTe_2$, and $MoSe_2$. For this, monolayers are mechanically exfoliated from bulk crystals in the 2H phase, bought from *HG graphene*

and encapsulated in hBN to enhance optical properties. PL spectra of the band-edge excitons are provided to characterize the samples. UPL signals, obtained under resonant excitation of the AX, are presented to probe the *s*-like HX. SHG measurements are shown to identify potential anticrossing features indicative of *p*-like HX. In addition, the power-law exponent of the SHG signal is determined, as it is known to be a robust indicator of excitonic resonances [190].

It should be noted that not all measurements could be performed under optimal conditions, as the range of accessible excitation wavelengths was limited by the available laser sources.

$MoSe_2$

First, we investigate the energetic landscape of a monolayer $MoSe_2$ at a temperature of 5 K. The sample is characterized by PL, UPL, and nonlinear optical measurements, as shown in fig. 4.7. The doping-resolved PL spectrum, obtained by excitation with a cw laser at 488 nm, an excitation power of 100 nW and integration time of 1 s, confirms the AX at 1.646 eV, the negative trion at 1.616 eV, and the positive trion at 1.621 eV.

The UPL spectrum, obtained under resonant excitation of the AX with a cw laser at 1.645 eV, excitation power of 1 mW (400 µJ cm^{-2}) and integration time of 250 s, reveals an *s*-like HX at 3.24 eV and a SHG signal of the incident laser. The small but consistent red shift for PL and UPL results, compared to published values, is likely due to sample-specific variations, like strain or defects. Previous studies have also reported high-lying trions in this material [181].

In order to investigate the excitation-energy dependence of the SHG close to excitonic resonances, the sample is excited by a pulsed laser with 80 MHz repetition rate, 80 fs pulse width and center frequencies ranging from 1.57 eV to 1.7 eV with increments of roughly 2 meV. The power is held constant at 400 µW (160 µJ cm^{-2}), each spectrum is integrated for 1 s. The obtained

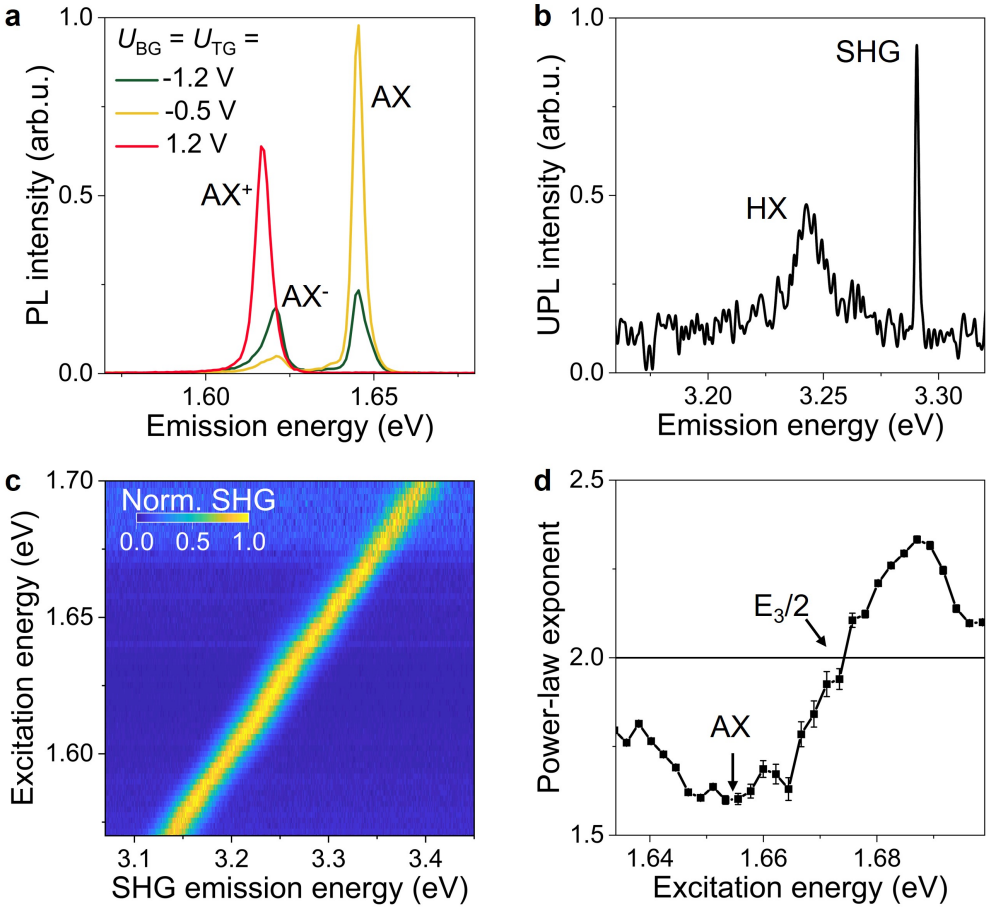

Figure 4.7: Optical spectroscopy results of monolayer $MoSe_2$ at 5 K. **a** PL measurements reveal the AX at 1.646 eV, a negative trion at 1.616 eV, and a positive trion at 1.621 eV. The applied gate voltage in this dual gated device, influencing the electrostatic doping of the system, is shown. **b** The UPL spectrum shows an *s*-like HX at 3.24 eV. The peak at 3.29 eV corresponds to SHG of the laser. **c** The normalized excitation-energy-dependent SHG signal shows no anticrossing feature, indicating a negative offset of the three-level system. **d** The power-law exponent of the SHG signal indicates the AX at 1.65 eV and the *p*-like HX at 3.35 eV. Error bars originate from the fitting procedure.

SHG signals show no anticrossing feature, which can be attributed to a larger energy separation between $|2\rangle$ and $|3\rangle$ than between $|1\rangle$ and $|2\rangle$, resulting in a negative offset that does not satisfy the resonance condition required for SHG splitting, confirming already published results [202].

Next, the power-law exponent of the SHG signal is investigated. For this, the sample is excited with energies ranging from 1.63 eV to 1.7 eV with increments of roughly 2 meV, while the power is varied with ten logarithmic spaced values between 500 µW (200 µJ cm^{-2}) and 5 mW (2000 µJ cm^{-2}) for 1 s, each. The resulting power-law exponent shows a non-trivial behavior: The AX appears as a dip at 1.65 eV, consistent with the PL results. An enhanced exponent is observed near 1.69 eV, exceeding the trivial value of 2, and crosses 2 at 1.675 eV. As discussed in section 2.5, this behavior indicates the presence of HX level at 3.35 eV, in agreement with the hypothesis of a negative offset. The offset is calculated as $\Delta E = -50$ meV.

$MoTe_2$

Next, we investigate the optical properties of monolayer $MoTe_2$. PL and SHG power-law exponent measurements, shown in fig. 4.8 were conducted at 5 K. PL measurements are performed by exciting the monolayer with a cw laser at 488 nm at an excitation power of 500 µW for an integration time of 60 s. Following assignments in literature, the measurements reveal a trion at 1.158 eV and the AX at 1.184 eV [221]. The emission-energy is at the edge of the detection range of our spectrometer, resulting in a reduced signal-to-noise ratio, which could be improved by even longer integration times. The power-law exponent, obtained from a different sample, indicates the bleached AX transition at 1.18 eV and a dispersive feature, indicating the *p*-like HX at 2.38 eV. No *s*-like HX could be observed, due to lacking of suitable laser radiation. The excitation-energy-dependent SHG signal shows no anticrossing features. This is conclusive for a negative offset of $\Delta E = -20$ meV.

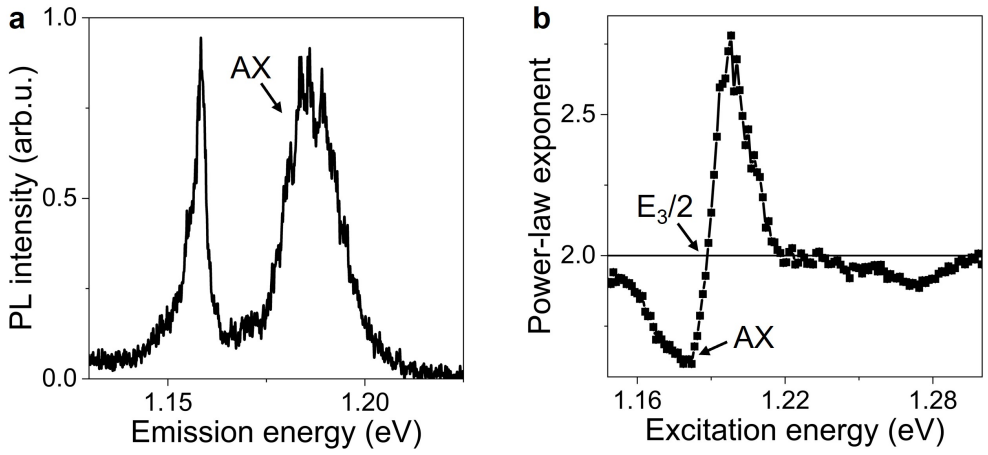

Figure 4.8: Optical spectroscopy results of monolayer $MoTe_2$ at 5 K. **a** The PL spectrum shows two distinct peaks. The emission at 1.184 eV is attributed to the AX. A trion is measured at 1.158 eV [221]. **b** The power-law exponent of the SHG signal reveals an AX at 1.18 eV and an HX energy of 2.38 eV.

WS_2

We now investigate a monolayer of WS_2 at 5 K. The PL spectrum of the AX, the UPL spectrum of HX, the power-law exponent of the SHG signal, and the excitation-energy dependence of the SHG signal are shown in fig. 4.9.

The PL spectrum, obtained under excitation with 488 nm at an excitation power of 5 µW for an integration time of 60 s, identifies the AX at 2.06 eV, along with lower-energy peaks, which we assign to many-body complexes such as trions. Under resonant excitation of the AX with a cw laser, at excitation energy of 2.06 eV, excitation power of 16 µW and 60 s integration time, UPL is observed. In addition to the SHG peak of the laser, a distinct signal at 4.039 eV is measured, which we assign to an *s*-like HX. A weaker peak at slightly lower energy could correspond to a high-lying trion. However, due to the absence of charge-carrier density tuning in this ungated sample, this assignment remains speculative.

Next, the excitation-energy dependence of the SHG is investigated with

an OPO, producing laser pulses with 140 fs pulse width at 80 MHz repetition rate and center excitation photon energies ranging from 2 eV to 2.1 eV with

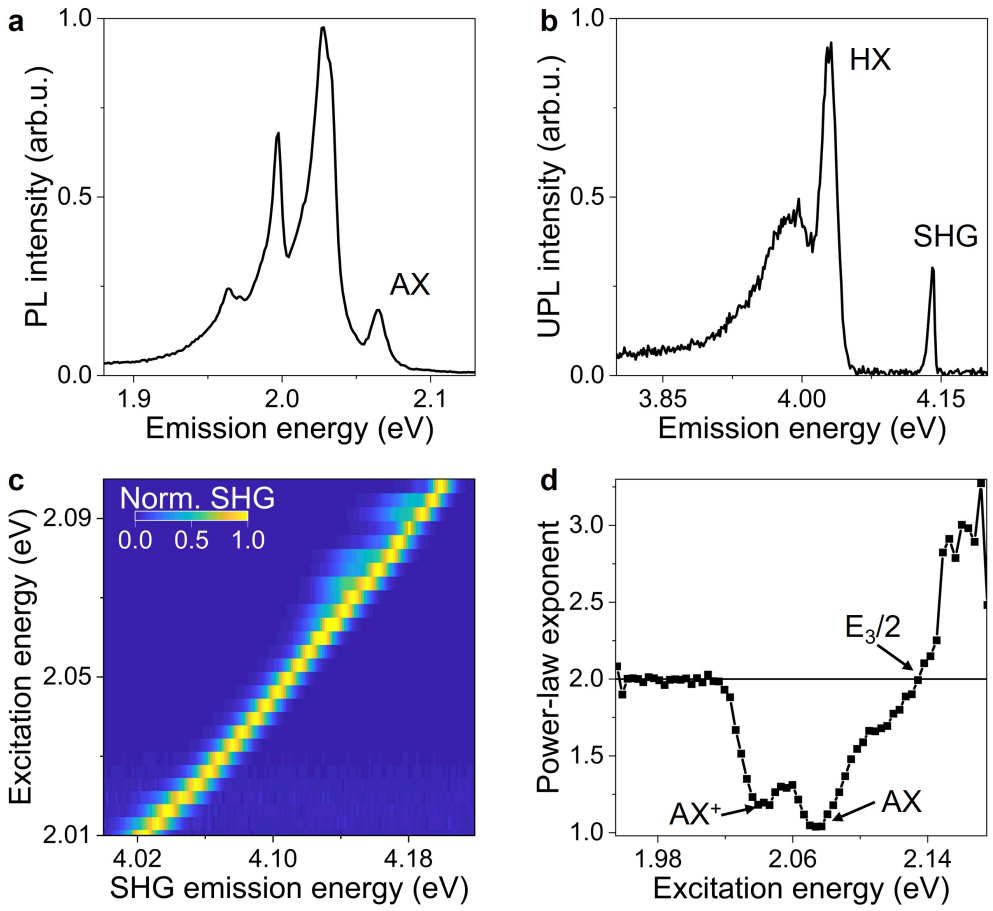

Figure 4.9: Optical spectroscopy results of monolayer WS_2 at 5 K. **a** The PL spectrum shows the AX at 2.06 eV and several many-body species at lower energies. **b** The UPL spectrum reveals an *s*-like HX at 4.026 eV. A second peak at slightly lower energy may correspond to a high-lying trion. The SHG of the laser appears at 4.14 eV. **c** The normalized excitation-energy-dependent SHG signal shows no anticrossing features. **d** The power-law exponent of the SHG signal displays dips at 2.07 eV and 2.04 eV, attributed to the neutral AX and positive AX^+, respectively. A crossing of the trivial exponent value of two suggests the presence of a *p*-like HX at 4.26 eV.

a spacing of roughly 3 meV. The excitation power is kept constant at 2 mW ($800\,\mu J\,cm^{-2}$) and spectra are integrated for 30 s. No anticrossing features are measured, indicating that the resonance condition is not satisfied. This is also supported by the power-law exponent, obtained by analysing the SHG signals generated by the sample by varying the excitation power from 800 µW ($320\,\mu J\,cm^{-2}$) to 3.2 mW ($1270\,\mu J\,cm^{-2}$) and back to 800 µW ($320\,\mu J\,cm^{-2}$) in four logarithmically spaced steps for 1 s at excitation energies ranging from 1.968 eV to 2.157 eV with increments of roughly 3 meV. The power-law exponent shows a non-trivial behavior, exhibiting two dips and one increase above the value of 2. The dip at 2.07 eV is assigned to the AX. The second dip at 2.04 eV is assigned to a trion species that has a sufficiently large oscillator strength due to intrinsic doping of the sample. The increase of the power-law exponent to a value of almost 3, visible at 2.15 eV, indicates the presence of a *p*-like HX at an energy of 4.26 eV. The offset of the corresponding three-level system is calculated as $\Delta E = -120$ meV, confirming a negative offset that prevents the quantum interference responsible for SHG dips.

MoS_2

Finally, we examine the optical properties of a monolayer MoS_2 at 5 K which are summarized in fig. 4.10, including the PL spectrum, the excitation-energy dependence of the SHG, and the SHG power-law exponent, obtained at 5 K. Due to the limited tuning range of the available laser sources, no *s*-like HX could be accessed by means of resonant upconversion in this sample. PL measurements are performed, using a cw laser at 488 nm with an excitation power of 200 µW for an integration time of 10 s. The AX is measured at 1.939 eV, with no clear signatures of trions in this ungated sample. The lower-energy PL emission is consistent with recombination from defect-trapped excitons, reported in literature [160].

To probe the *p*-like HX, we investigate the excitation-energy dependence of the SHG signal with the OPO, producing laser pulses with 140 fs pulse

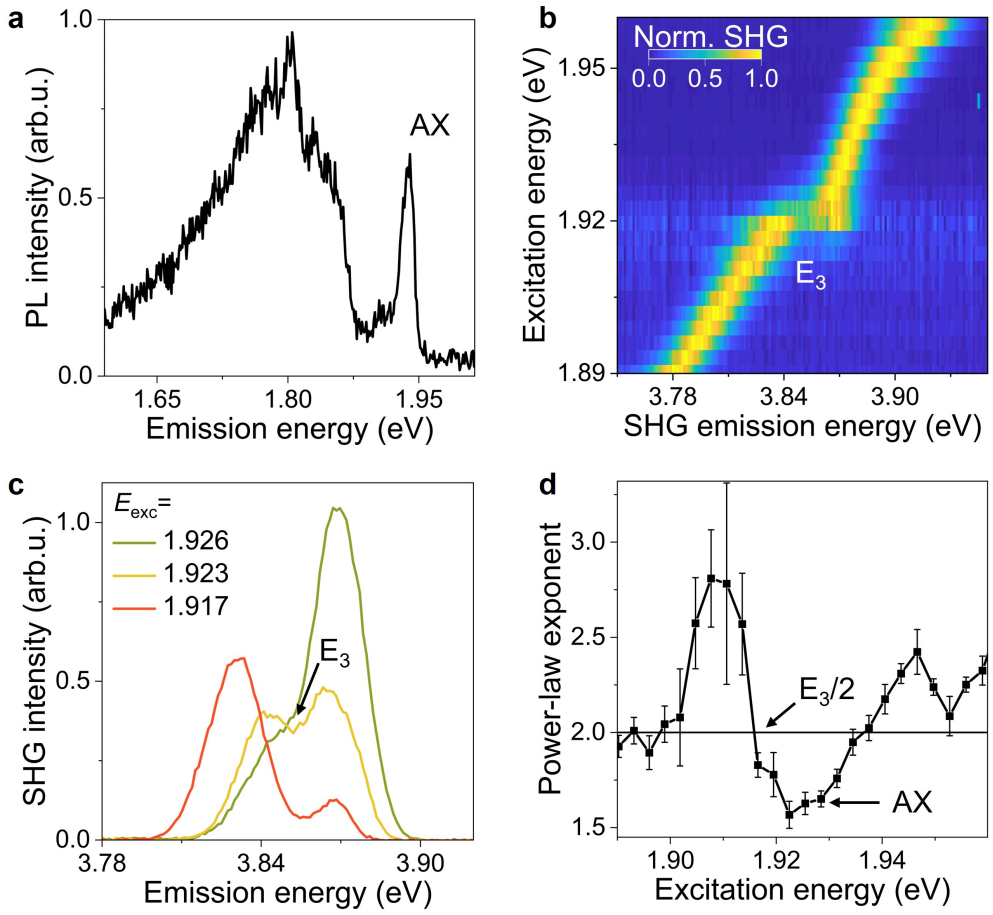

Figure 4.10: Spectroscopy results of monolayer MoS_2 at 5 K. **a** PL spectrum showing the AX at 1.939 eV. The lower-energy emission arises from defect-trapped excitons [160]. **b** Excitation-energy-dependence of the normalized SHG signal. A pronounced anticrossing appears at 1.923 eV, indicating a two-photon resonance with the third state E_3. **c** SHG spectra for three excitation energies around the anticrossing feature, revealing a dip at 3.846 eV. **d** Power-law exponent of the SHG signal, showing features consistent with excitonic resonances at 1.925 eV and 3.831 eV, as discussed in section 2.5.

width at 80 MHz repetition rate and center excitation-photon energies ranging from 1.88 eV to 1.97 eV with increments of roughly 3 meV. The excita-

tion power is held constant at 2 mW (800 µJ cm^{-2}), and each spectrum is integrated for 120 s. Remarkably, the resulting spectra, normalized to the maximum of the SHG signal, exhibits a pronounced anticrossing at 3.846 eV. Analysis of single line spectra for three different center excitation-photon energies, shows that the dip is at a constant energy and the spectral weigthing of the two branches depends on the position of the SHG signature. This characteristics is comparable to the SHG dip observed in WSe_2 [190, 200, 202].

Finally, the power-law exponent of the SHG signal is investigated. The sample is excited with energies ranging from 1.89 eV to 1.97 eV with increments of roughly 3 meV, while the power is varied with six logarithmic spaced values between 600 µW (340 µJ cm^{-2}) and 2.8 mW (1110 µJ cm^{-2}) for 100 s, each. In the resulting spectra, the AX manifests as a dip at 1.925 eV, while an enhanced exponent of approximately 2.8 appears at 1.908 eV. The crossing of the power-law exponent with a value of two at 1.9155 eV strongly suggests the presence of a *p*-like HX at 3.831 eV.

The small difference of HX measured by a dip in the SHG spectrum and the power-law exponent can be attributed to sample inhomogeniety or sligthly different experimental conditions. Nevertheless, both measurements consistently indicate the presence of a *p*-like HX in monolayer MoS_2. The corresponding three-level system shows a positive offset, determined from the power-law exponent measurement as: $\Delta E = 32$ meV, a value well within the range that supports quantum interference effects [201, 202].

Discussion

To provide an overview of the excitonic landscapes in the investigated materials, fig. 4.11 and table 4.1 summarize the offsets between excitonic levels, defined as the difference between the measured energies and twice the AX energy. For reference, data for monolayer WSe_2 [190, 202] and 30° twisted bilayer WSe_2 [201] are included.

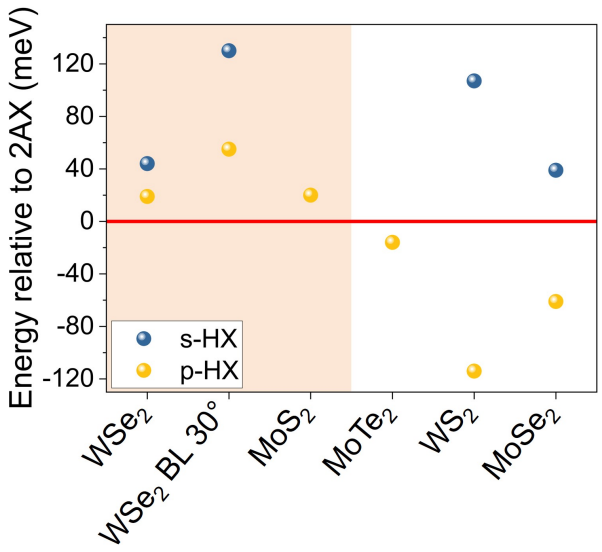

Figure 4.11: Summary of the energetic landscape of HX in different semiconducting TMDCs. The measured energies are shown relative to twice the AX energy of each material, according to $\Delta E = 2E_{AX} - E_i$, where E_i corresponds to either the p-like HX (yellow spheres) or the s-like HX (blue spheres). Data are shown for monolayer WSe_2, 30° twisted bilayer WSe_2, monolayer MoS_2, monolayer $MoTe_2$, monolayer WS_2, and monolayer $MoSe_2$. Samples exhibiting quantum interference in the SHG signal are highlighted in orange.

A positive offset of the three-level system (ground state, AX, and p-like HX) is observed in monolayer MoS_2, monolayer WSe_2, and 30° twisted bilayer WSe_2, as indicated by the orange box. Quantum interference in the SHG signal occurs exclusively in these samples. Materials with negative offset exhibit no SHG splitting. Whenever UPL measurements reveal an s-like HX, its energy is consistently lower than twice the AX energy. This may represent a necessary condition for populating the high-lying state via the upconversion process.

	Energy AX (eV)	Energy s-HX (eV)	Energy p-HX (eV)	SHG quantum interference
WSe_2 [190, 201]	1.722	3.40	3.425	✓
WSe_2 30° [202]	1.725	3.32	3.395	✓
MoS_2	1.925	-	3.831	✓
$MoTe_2$	1.18	-	2.38	✗
WS_2	2.07	4.039	4.26	✗
$MoSe_2$	1.646	3.24	3.35	✗

Table 4.1: Summary of the energetic landscape of AX, s-like HX and p-like HX in different TMDCs. The materials for which quantum interference of the SHG signal occurs are marked.

In summary, we have shown that HX species are a general phenomena in semiconducting TMDCs. The materials show slightly different relative positions of the excitonic levels, leading to different offsets of the corresponding three-level systems, that influences the appearence of quantum interference effects in the SHG signal. It should be noted that the influence of HX in WSe_2 is particularly pronounced compared to other materials. The reason for this is not fully understood yet. One can speculate that the differences of the involved elements, leading to variations in spin-orbit coupling strength, affects the band structure of the material in which HX species are formed. Further detailed theoretical studies are required to fully understand the underlying mechanism.

4.2 Temporal dynamics of high-lying excitons

Having established the excitonic landscape of HXs in several semiconducting TMDCs, we now turn to the investigation of their temporal dynamics by employing two complementary experimental approaches. First, the characteristic time scales of *p*-like HX are probed via nonlinear optical mixing processes. Second, direct streak-camera measurements provide information on the radiative lifetime of an *s*-like HX.

4.2.1 Influence of excitonic resonances on optical wave-mixing experiments

Monolayers of TMDCs are well known for their strong nonlinear optical response, arising from their high nonlinear susceptibility. Most previous investigations have been performed in the non-resonant regime, where the response is dominated by the second-order susceptibility. In this regime, the optical behavior is governed by parametric processes, as the material's energy levels remain unaffected by the laser field [206]. In contrast, here we investigate nonlinear processes under resonant excitation of the material's energy levels. Resonant excitation leads to strong coupling between the energy levels, giving rise to phenomena such as Rabi oscillations and AC-Stark shifts. In our experiments, two lasers are used. The first is tuned either to the AX resonance or to the two-photon resonance of the HX, while the second laser is fixed at an energy of 1.476 eV and serves as a non-resonant probe by providing a second photon. For clarity, we refer to the first, resonant laser as the *pump* and the second, non-resonant laser as the *probe*, without imposing restrictions on their power or temporal sequence. Both beams are focused onto the sample in a collinear geometry and are distinguished in detection by their spectral signatures. The results presented here are discussed in detail in Ref. [222].

We investigate two nonlinear processes, illustrated in fig. 4.12. The first is SFG, in which the energies of the two photons are combined to produce a new photon with the sum energy

$$\hbar\omega_{\mathrm{SFG}} = \hbar\omega_{\mathrm{pump}} + \hbar\omega_{\mathrm{probe}}. \tag{4.2}$$

In this process the signal is influenced by the AX level, as we resonantly excite it with the pump laser. The second process is FWM, where the energy of two pump photons is reduced by one probe photon to create a photon with energy

$$\hbar\omega_{\mathrm{FWM}} = 2\hbar\omega_{\mathrm{pump}} - \hbar\omega_{\mathrm{probe}}. \tag{4.3}$$

Here, resonant two-photon excitation of the HX with the pump laser enables us to investigate the temporal dynamics of the HX by analyzing the FWM signal.

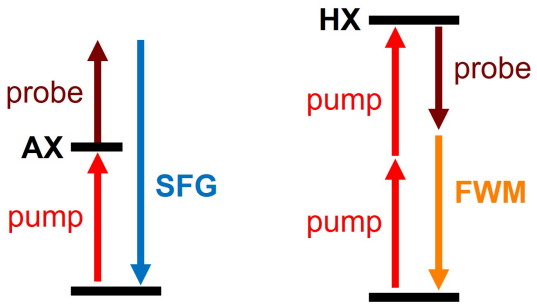

Figure 4.12: Schematic illustration of two nonlinear processes: SFG (left) and FWM (right). The two lasers are indicated by light red arrows (pump) and dark red arrows (probe). The detected signals are shown as a blue arrow (SFG) and an orange arrow (FWM). The relevant energy levels, AX and HX, are represented by black horizontal lines.

Under simultaneous excitation of a monolayer WSe_2 at a cryogenic temperature of 5 K with both lasers, the spectrum shown in fig. 4.13 is obtained. Several distinct peaks are visible, which can be assigned to specific nonlinear processes based on their spectral signatures. The incident laser energies are

$\hbar\omega_{\text{probe}} = 1.476\,\text{eV}$ and $\hbar\omega_{\text{pump}} = 1.739\,\text{eV}$. The peak at 3.478 eV corresponds to the SHG of the pump laser, while the peak at 2.952 eV arises from the SHG of the probe laser. The peak at 3.215 eV is attributed to the SFG process, in which the energies of the two photons are added to produce a photon at the sum energy. The peak at 2.002 eV is assigned to the FWM process, where the energy of two pump photons is reduced by one probe photon.

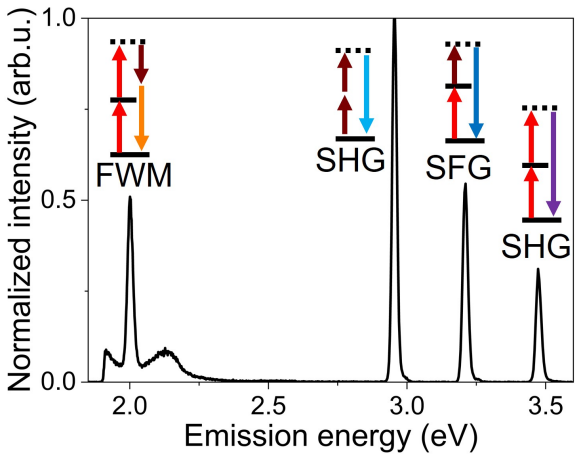

Figure 4.13: Measured spectrum of a monolayer WSe_2 at 5 K under simultaneous excitation with a pump laser at 1.739 eV (light red) and a probe laser at 1.476 eV (dark red) with zero time delay. Several distinct peaks are observed and assigned to nonlinear optical processes, schematically indicated next to their spectral signatures. 3.478 eV: SHG of the pump, 2.952 eV: SHG of the probe, 3.215 eV: SFG, 2.002 eV: FWM.

To investigate the temporal dynamics of the signal, the time delay between the peaks of the two laser pulses is adjusted, as defined in fig. 4.14. The delay time is given by

$$\Delta t = t_{\text{probe}} - t_{\text{pump}}, \tag{4.4}$$

where t_{probe} and t_{pump} denote the arrival times of the probe and pump pulses, respectively. A positive delay time corresponds to the pump pulse arriving

first, while a negative delay time indicates that the probe pulse arrives first. The FWHM of the laser pulses is on the order of 130 fs to 150 fs, comparable to the delay times used in the experiment. Consequently, temporal overlap between portions of the two pulses occurs in most of the cases presented in this work.

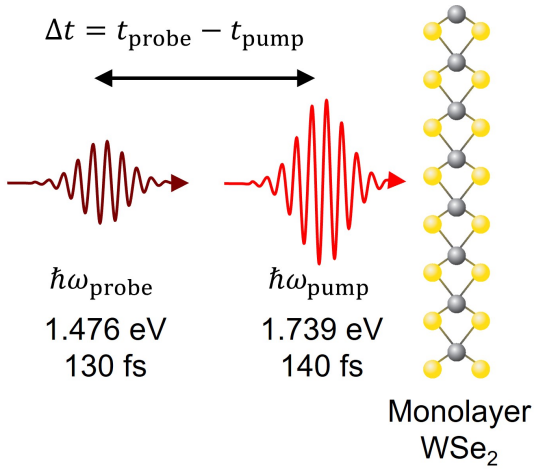

Figure 4.14: Schematic representation of the definition of delay time. The Gaussian-shaped pump and probe laser pulses are depicted in light red and dark red, respectively, with their corresponding energies and pulse length FWHM values. A schematic illustration of the crystal lattice of a monolayer WSe_2 is shown on the right side. The delay time is defined as the time between the peak of the probe laser and the peak of the pump laser, $\Delta t = t_{\text{probe}} - t_{\text{pump}}$. A positive delay time corresponds to the pump laser arriving first, while a negative delay time corresponds to the probe laser arriving first.

Varying the delay time between the laser pulses gives rise to several phenomena. The SHG signals of the individual lasers are expected to be independent of delay time, as only photons from a single laser pulse contribute to their generation. In contrast, the SFG and FWM signals should exhibit a clear delay time dependence, since photons from both laser pulses are required. A straightforward expectation is that the time-dependent SFG and FWM signals would reach their maximum intensity when the two pulses are

temporally overlapping, as the electric field at the sample is then at its highest. However, this is not observed experimentally, as shown in fig. 4.15. The

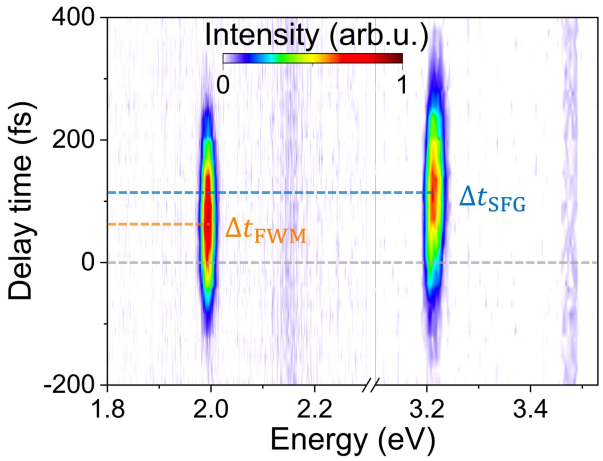

Figure 4.15: Two-dimensional color plot of the spectra obtained from the excitation of a monolayer of WSe_2 at a cryogenic temperature of 5 K, using a pump laser with an energy of 1.739 eV and a probe laser with an energy of 1.476 eV. The time delay Δt is varied from -200 fs to 400 fs with increments of 20 fs. The zero delay time is indicated by the gray dashed line. The delay corresponding to the maximum SFG intensity, Δt_{SFG}, is marked by the blue dashed line, and the delay corresponding to the maximum FWM intensity, Δt_{FWM}, is marked by the orange dashed line. Both nonlinear signals reach their maximum at a time later than the temporal overlap of the two laser pulses.

spectrum reveals that the SHG signal is time-independent, whereas the SFG and FWM signals exhibit a clear time dependence. Notably, the maximal intensities of the SFG and FWM signals occur at delay times later than the temporal overlap of the two laser pulses, i.e., when the probe pulse arrives at the sample after the pump pulse. This behavior can be explained by the fact that the SFG and FWM signals depend not only on the instantaneous electric fields of the two pulses but also on the population dynamics of the involved energy levels.

To determine the delay times corresponding to the maximum SFG and FWM intensities, we perform Gaussian fits to the spectral signatures at each measured delay time. The resulting peak intensities are plotted as a function of delay time in fig. 4.16.

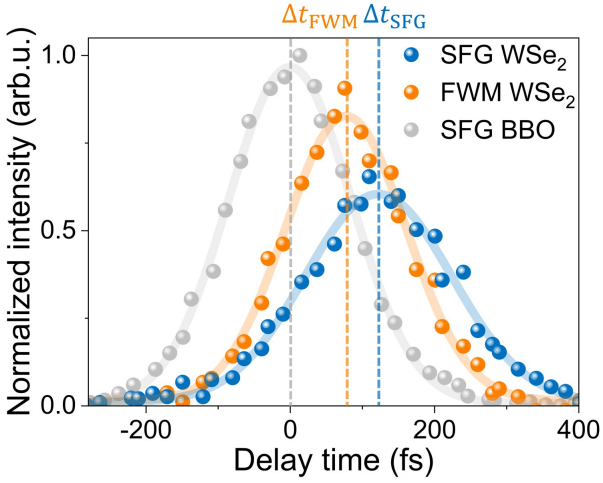

Figure 4.16: Determination of the delay times corresponding to the maximal intensities of the SFG signal (Δt_{SFG}, blue) and the FWM signal (Δt_{FWM}, orange). At each delay time, the spectra are fitted with a Gaussian peak. The resulting maximal intensities (colored spheres) are plotted as a function of delay time. Gaussian fits to these data (light blue and orange lines) yield the delay times of maximal intensity. For each wavelength combination, a reference is obtained by measuring the SFG signal from a BBO crystal (gray spheres and line). The extracted delay times for this experiment are $\Delta t_{\mathrm{SFG}} = 120\,\mathrm{fs}$ and $\Delta t_{\mathrm{FWM}} = 80\,\mathrm{fs}$.

By fitting these intensity-delay curves with Gaussian functions, we extract the delay times of maximal intensity, denoted as Δt_{SFG} and Δt_{FWM}, respectively. To define a reference time corresponding to perfect temporal overlap of the two pulses, we measure the SFG signal from a BBO crystal placed outside the cryostat simultaneously with the measurement on the WSe_2 monolayer. Since the BBO crystal is not resonantly excited, its SFG

signal is unaffected by population dynamics. The zero-delay time depends on the specific wavelength combination used. Therefore, we calibrate it for each wavelength combination by comparing the SFG signal from the external BBO crystal with the SFG signal from a second BBO crystal mounted inside the cryostat next to the WSe_2 sample. This BBO is only 100 µm thick, to obtain phase matching conditions over a broad spectral range and limit unwanted temporal effects.

To further investigate the influence of excitonic resonances on the nonlinear processes, we vary the energy of the resonant pump laser from 1.71 eV to 1.765 eV, while keeping the probe laser fixed at 1.476 eV. The delay times of maximal intensity for SFG (Δt_{SFG}) and FWM (Δt_{FWM}), together with the PL spectrum of the sample, are plotted as a function of pump laser energy in fig. 4.17. The pump energy, where the largest delay time of maximal

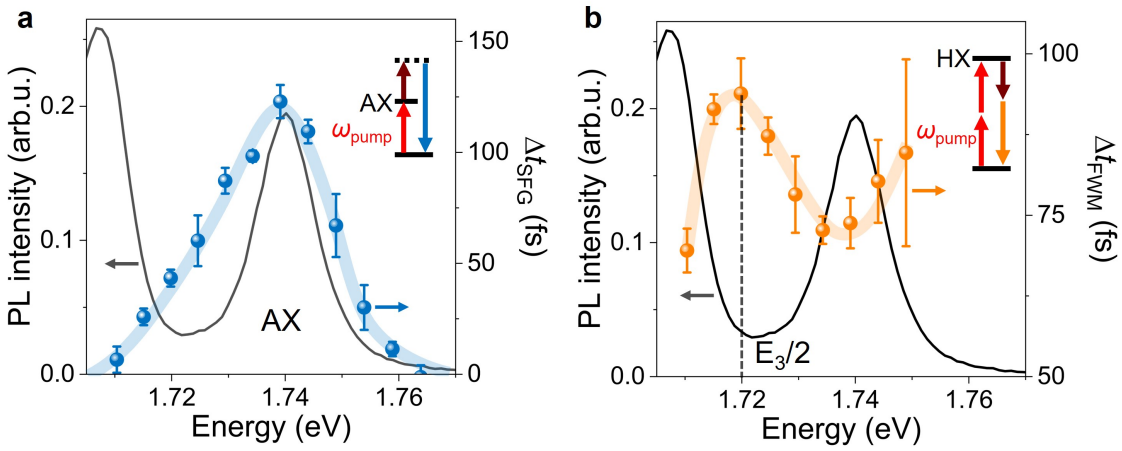

Figure 4.17: Pump-energy dependence of the delay times corresponding to the maximal SFG signal **a** and FWM signal **b**. The inset illustrates the nonlinear processes and the involved energy levels. The PL spectrum is shown in black. **a** The delay time of maximal SFG signal, Δt_{SFG}, is shown as blue dots, with the blue line serving as a guide to the eye. **b** The delay time of maximal FWM signal, Δt_{FWM}, is shown as orange dots, with the orange line as a guide to the eye.

SFG intensity, $\Delta t_{\mathrm{SFG}} = 120\,\mathrm{fs}$ occurs, coincides with the energy of the AX obtained from PL measurements. For off-resonant excitation, the delay time decreases and reaches 0 fs when the excitation energy is more than 20 meV detuned from resonance. No influence of the trion on the delay time is observed. In contrast, the pump-energy dependence of the delay time for the maximal FWM signal exhibits a more complex behavior. The largest value, $\Delta t_{\mathrm{FWM}} = 80\,\mathrm{fs}$, occurs at a pump energy of 1.72 eV, corresponding to the two-photon resonance of the HX state at 3.44 eV. For pump energies above 1.74 eV, the delay time increases again, which could be attributed to a Stark-shifted AX state induced by the strong electric field of the pump laser.

Next, we investigate the influence of the pump power of the resonant laser. The pump power is varied from 1 µW ($0.4\,\mu\mathrm{J\,cm^{-2}}$) to 2.5 mW ($1000\,\mu\mathrm{J\,cm^{-2}}$) in logarithmic steps, with the pump laser tuned to the AX resonance at 1.739 eV. The resulting delay times of maximal intensity are shown in fig. 4.18 for the SFG signal (**a**) and the FWM signal (**b**). As an additional reference, the pump-power dependence under non-resonant excitation of a WS_2 monolayer is also presented. The delay time of the maximal SFG signal, Δt_{SFG}, reaches its highest value of 120 fs at the smallest pump power of 1 µW ($0.4\,\mu\mathrm{J\,cm^{-2}}$). With increasing pump power, the delay time decreases and reaches 0 fs at 2.5 mW ($1000\,\mu\mathrm{J\,cm^{-2}}$). The delay time of the maximal FWM signal, Δt_{FWM} obtained in the same measurement, reaches its maximum of 80 fs at 1 µW ($0.4\,\mu\mathrm{J\,cm^{-2}}$), decreases with increasing pump power, crosses 0 fs at 400 µW ($160\,\mu\mathrm{J\,cm^{-2}}$), and reaches negative values of −40 fs at 2.5 mW ($1000\,\mu\mathrm{J\,cm^{-2}}$). For the reference WS_2 sample, the delay times of both maximum SFG and maximum FWM signals remain constant at 0 fs for all pump powers, indicating that the observed effects are resonance-dependent.

Several mechanisms could account for the observed pump-power dependence of the delay times. The reduction of the delay time with increasing pump power can be explained by a shortening of the state lifetimes due to higher population densities and, consequently, increased scattering rates.

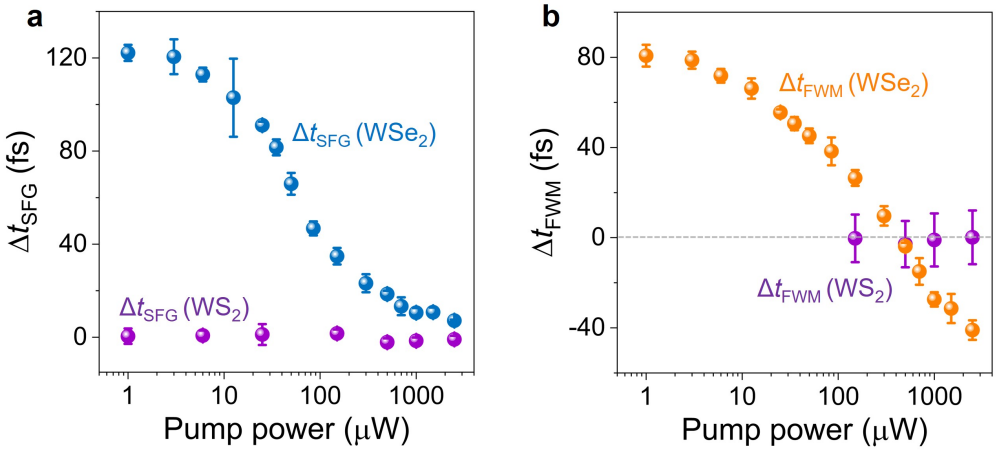

Figure 4.18: Pump-power dependence of the delay times corresponding to the maximal SFG signal and FWM signal. **a** The SFG signal (blue dots), Δt_{SFG} reaches its maximum value of 120 fs under resonant excitation of the AX at the lowest pump power of 1 µW (0.4 µJ cm^{-2}). The delay time decreases with increasing pump power, reaching 0 fs at 2.5 mW (1000 µJ cm^{-2}). **b** For the FWM signal (orange dots), Δt_{FWM} reaches 80 fs under resonant excitation of the AX state at 1 µW (0.4 µJ cm^{-2}), decreases with increasing power, crosses 0 fs at 400 µW (160 µJ cm^{-2}), and reaches negative values of −40 fs at 2.5 mW (1000 µJ cm^{-2}). As a reference, the delay times for non-resonant excitation of a WS_2 monolayer (purple dots) remain constant at 0 fs for all pump powers.

However, this mechanism alone cannot explain the negative delay times observed in the FWM signal at high pump powers.

To gain further insight, we perform simulations based on the density-matrix formalism to study the interplay between the electric fields of the laser pulses and the population dynamics of the involved energy levels. The toy model used is presented in fig. 2.23. The simulation parameters are chosen to match the experimental conditions as closely as possible. The pump laser photon energy is set to 1.739 eV at a power of 1 µW (0.4 µJ cm^{-2}), resonant with the AX. The probe laser photon energy is set to 1.476 eV at a power of 200 µW (80 µJ cm^{-2}). The Fourier transform of the time-dependent

polarization, $P(\mathrm{t})$, yields the frequency-dependent polarization, $P(\omega)$, which can be interpreted as the emission spectrum of the material, which is shown in fig. 4.19, with the intensity plotted on a logarithmic scale to capture peaks spanning over a wide range. The spectrum exhibits the same distinct features as observed experimentally in fig. 4.13, corresponding to the SHG of the pump laser, the SHG of the probe laser, the SFG process, and the FWM process.

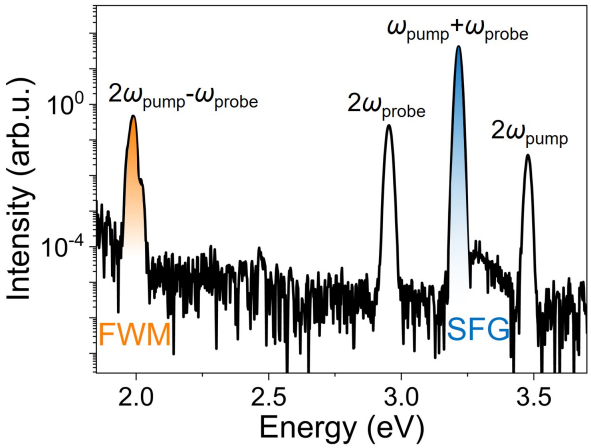

Figure 4.19: Simulated spectrum of the nonlinear optical processes, obtained using the model parameters listed in table 2.1. The spectral signatures of the FWM process (orange), the SHG of the probe beam, the SFG process (blue), and the SHG of the pump beam are indicated.

In analogy to the experimental procedure, we perform a delay-time scan by varying the parameter t_{probe} of the probe field while keeping the center time of the pump field fixed at $t_{\mathrm{pump}} = 0\,\mathrm{fs}$. Spectra are calculated for delay times ranging from $-300\,\mathrm{fs}$ to $400\,\mathrm{fs}$ in steps of $10\,\mathrm{fs}$. For each delay time, the spectral contributions of the individual nonlinear processes are integrated. The resulting intensities for the SFG signal (blue dots) and the FWM signal (orange dots) are plotted as a function of delay time in fig. 4.20. The corresponding experimental data are shown in fig. 4.16 for comparison. For this specific parameter setting, the maximal intensities of both the SFG

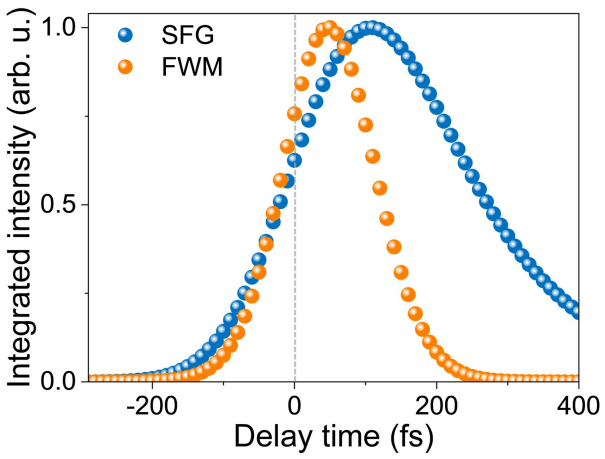

Figure 4.20: Simulated delay-time dependence of the integrated intensities of the SFG signal (blue) and the FWM signal (orange). For each delay time, the SFG and FWM intensities are fitted with a Gaussian function. In this parameter setting, the maximal SFG intensity occurs at a delay time of 105 fs, while the maximal FWM intensity occurs at 60 fs.

and FWM signals occur at positive time delays, i.e., larger than 0 fs. The integrated intensity profiles are not symmetric with respect to their maxima. This asymmetry arises because the signal is not solely determined by the convolution of two Gaussian-shaped electric fields, which would yield a symmetric Gaussian profile, but also by the population dynamics of the involved energy levels, which decay exponentially over time. A similar effect is expected but not seen in the experiment. To account for the asymmetry in the simulated data, we employ a bi-Gaussian fitting function, to obtain the time of maximal signal.

Following the experimental approach, we then investigate the dependence of the nonlinear signals on the pump-laser energy. The pump energy is varied from 1.705 eV to 1.77 eV at a fixed power of 1 µW (0.4 µJ cm^{-2}), chosen to probe the low-power regime in which the largest delay times were observed experimentally (fig. 4.18). The probe laser is kept constant at 1.476 eV. The

resulting delay times of maximal SFG intensity, Δt_{SFG} (blue dots), and maximal FWM intensity, Δt_{FWM} (orange dots), as a function of pump energy are shown in fig. 4.21. The energies of the AX and the two-photon resonance

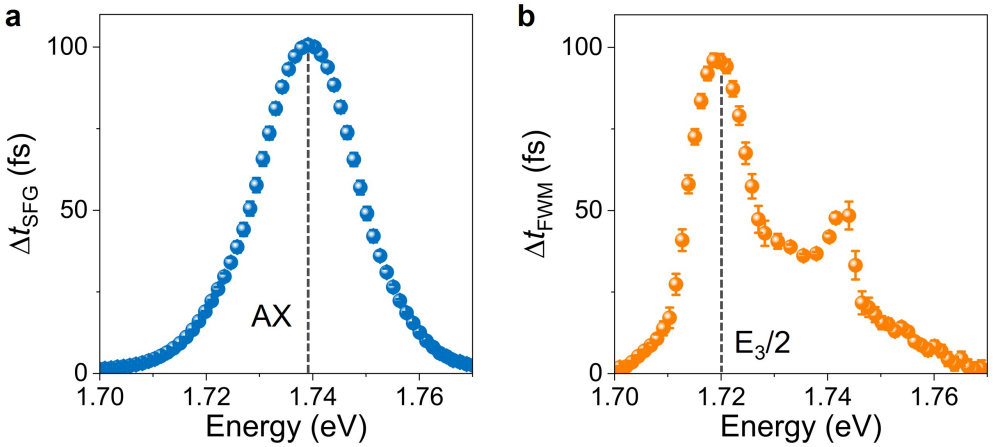

Figure 4.21: Simulated delay times of maximal SFG intensity (blue dots) and maximal FWM intensity (orange dots). Error bars result from the bi-Gaussian fitting. **a** The SFG delay time reaches its maximum at the AX resonance (1.739 eV) and decreases for off-resonant excitation. **b** The FWM delay time is maximal at the two-photon resonance of the HX state (3.44 eV).

of state $|3\rangle$ at energy $E_3/2$ are indicated by black dashed lines. The resonant enhancement of the SFG signal at the AX energy is clearly visible, as well as the resonant enhancement of the FWM delay time at the two-photon resonance of the HX state. The feature of the FWM signal at slightly higher energy as the AX can be attributed to a resonance effect of a Stark-shifted energy level, which can also be seen in the experimental data. For both signals, the delay time decreases under off-resonant excitation and approaches 0 fs. The maximal simulated delay times are $\Delta t_{\mathrm{SFG}} = 105\,\mathrm{fs}$ and $\Delta t_{\mathrm{FWM}} = 95\,\mathrm{fs}$, in good agreement with the experimental values. Furthermore, these values are influenced by the lifetimes of the relevant energy levels, which can be tuned in the simulation to match experimental results, as will be shown in

fig. 4.24. Overall, the simulated pump-energy dependence exhibits excellent agreement with the experimental findings, shown in fig. 4.17.

Next, we investigate the influence of the pump power of the resonant laser. The pump power is simulated from 1 µW (0.4 µJ cm^{-2}) to 5 mW (2000 µJ cm^{-2}) in logarithmic steps. For the SFG signal, the pump laser is tuned to the AX resonance at 1.739 eV, while for the FWM signal, it is set to the two-photon resonance of the HX state at 1.72 eV. The probe laser is kept constant at 1.476 eV. The simulated SFG and FWM intensities as a function of delay time and pump power are shown in fig. 4.22. The white dashed lines indicate the delay times corresponding to the maximal intensities of the SFG and FWM signals, respectively. Both simulated signals

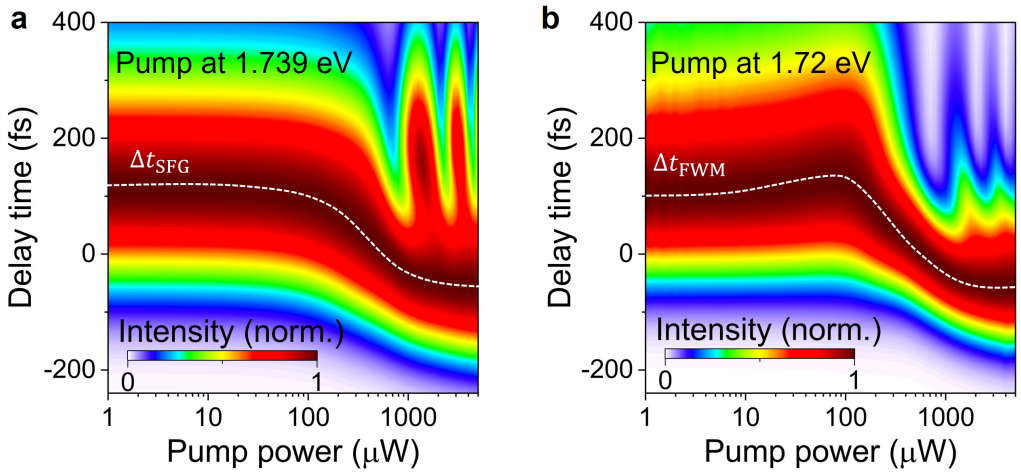

Figure 4.22: Simulated pump-power dependence of the delay times for **a** the SFG signal and **b** the FWM signal. For the SFG signal, the pump laser is tuned to the AX resonance at 1.739 eV. For the FWM signal, it is tuned to the two-photon resonance of the HX state at 1.72 eV. The probe laser is fixed at 1.476 eV. The white dashed lines indicate the delay times of maximal intensity for each signal. A clear reduction in delay time with increasing pump power is observed. At pump powers above 1000 µW (400 µJ cm^{-2}), additional periodic peaks appear in both SFG and FWM signals, which we attribute to Rabi oscillations, an effect not observed in the experiment.

reproduce the general behavior observed in the experiment. The delay time is maximal at the lowest pump power and decreases with increasing pump power. In contrast to the experimental results, shown in fig. 4.18, however, both the SFG and FWM signals cross the 0 fs delay at a pump power of 600 µW (240 µJ cm^{-2}). At higher powers, both delay times become negative, reaching values of approximately −50 fs. At high pump powers, both signals exhibit a more complex, finger-like structure, which we attribute to Rabi oscillations between the energy levels. These high-power effects are absent in the experiment. We speculate that this discrepancy originates from higher-order power effects, such as enhanced exciton-exciton annihilation, which are not included in the density-matrix simulation.

To gain further insight into the underlying dynamics, we examine the time evolution of the density-matrix elements, as shown in fig. 4.23. We plot the populations of the three involved energy levels, ρ_{11} (gray), ρ_{22} (blue), and ρ_{33} (orange), for a pump power of **a** 1 µW (0.4 µJ cm^{-2}) and **b** 1 mW (400 µJ cm^{-2}), at a pump photon energy of 1.739 eV, without a probe pulse. The pump pulse is centered at 0 fs, and the populations are shown as a function of time. Before the arrival of the pump pulse, the population resides entirely in the ground state, ρ_{11}. Starting at simulation time 0 fs, the ground-state population decreases as it is transferred to the first and second excited states, ρ_{22} and ρ_{33} by the simulated field pulse. In the low-power regime this transfer occurs over a finite time, influenced by the lifetimes of the states. The maximal population for ρ_{22} is reached at 105 fs, maximal population for ρ_{33} is reached at 40 fs. These times of maximal population in ρ_{22} and ρ_{33}, indicated by black arrows, match perfectly to the delay time of maximal SFG, $\Delta t_{\mathrm{SFG}} = 105$ fs and maximal FWM, $\Delta t_{\mathrm{FWM}} = 40$ fs for resonant AX excitation, respectively.

In the high-power regime, the ground-state population is depleted much more rapidly, and the excited states reach their maximum populations even before the center of the pump pulse. While the pulse is still present, the

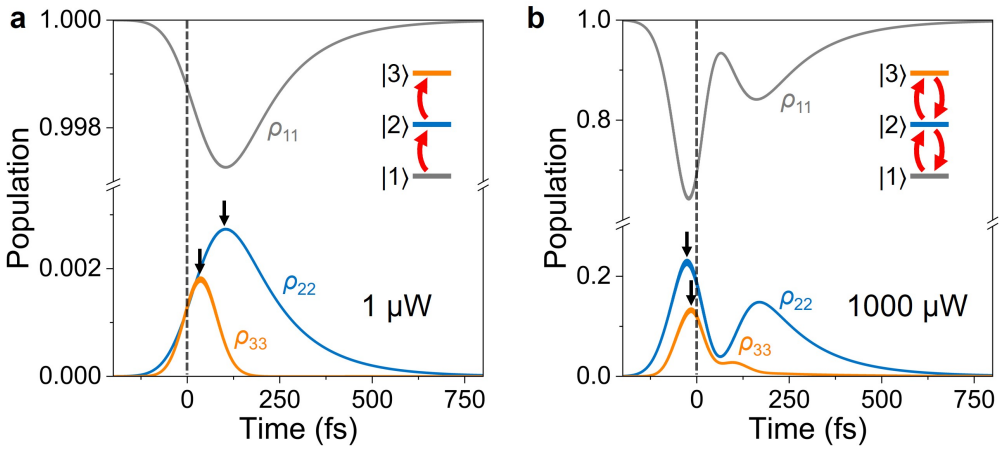

Figure 4.23: Simulated population dynamics of the three-level system for a pump power of **a** 1 µW (0.4 µJ cm^{-2}) and **b** 1 mW (400 µJ cm^{-2}). The populations of the ground state ρ_{11}, first excited state ρ_{22}, and second excited state ρ_{33} are shown in gray, blue, and orange, respectively. The pump pulse is centered at 0 fs. Times of maximal population of the excited states are marked with black arrows. The insets illustrate the proposed Rabi cycle mechanism.

excited-state populations decrease and then rise again, indicative of Rabi oscillations between the states. This behavior is known from experiments and can be observed as a spectral signature in SHG measurements [190]. Due to these oscillations, the maximal populations occur at negative delay times on the order of −30 fs, which in turn can manifest as negative Δt_{SFG} and Δt_{FWM} values.

In contrast to the simulation, the experimentally measured Δt_{SFG} never reaches negative values. We attribute this discrepancy to the absence in the model of many-body effects such as exciton-exciton annihilation or scattering processes, which can substantially increase the decay rate of state $|2\rangle$.

Finally, we explore the influence of the lifetimes of the involved energy levels on the delay times of maximal SFG and FWM intensities. Figure 4.24 shows the simulated dependence of Δt_{SFG} (blue dots, top row) and Δt_{FWM}

(orange dots, bottom row) on the lifetimes of the states.

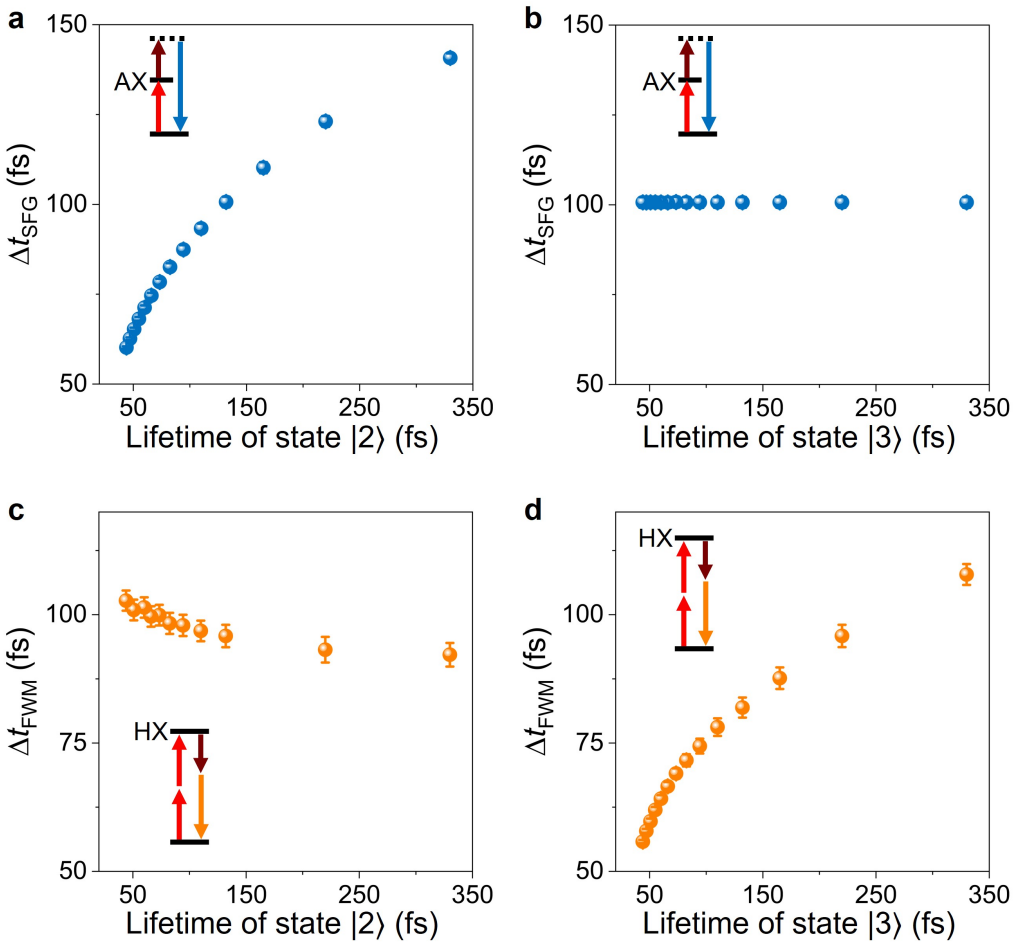

Figure 4.24: Simulated dependence of the delay times of maximal SFG and FWM signals on the lifetimes of the states. For the SFG signal, the delay time is strongly influenced by the lifetime of the second state $|2\rangle$ (top left) but shows no dependence on the lifetime of the third state $|3\rangle$ (top right). For the FWM signal, the delay time exhibits only a slight dependence on the lifetime of state $|2\rangle$ (bottom left) but is highly sensitive to the lifetime of state $|3\rangle$ (bottom right).

The lifetimes are varied from 50 fs to 350 fs. For the SFG signal, the pump

energy is set to the AX resonance at 1.739 eV, and for the FWM signal, to the two-photon resonance of the HX state at 1.72 eV, both at a pump power of 1 µW (0.4 µJ cm^{-2}). The probe laser is fixed at 1.476 eV. It is evident that Δt_{SFG} is highly sensitive to the lifetime of state $|2\rangle$, increasing with longer lifetimes. The experimentally observed maximum of 120 fs is reproduced in the simulation for a lifetime of approximately 200 fs, which is in good agreement with reported values [153, 162, 182–186]. In contrast, Δt_{SFG} is essentially independent of the lifetime of the HX state $|3\rangle$.

For the FWM signal, the situation is reversed. Δt_{FWM} shows a strong dependence on the lifetime of state $|3\rangle$, reaching the experimental maximum of 80 fs for a lifetime of about 150 fs. The dependence on the lifetime of state $|2\rangle$ is comparatively weak.

In summary, we show that the intensity of nonlinear wave-mixing signals such as SFG and FWM are highly sensitive to the excitonic resonances of the material. The simulations based on density-matrix formalism reproduce the experimental findings with high accuracy and provide insights into the underlying population dynamics, which show Rabi oscillations, responsible for the delay times required to reach maximal signal intensity. Furthermore, we demonstrate that the delay times are strongly influenced by the lifetimes of the involved energy levels, enabling their estimation based on nonlinear optical measurements.

Finally, we investigate the temporal dynamics of bright *s*-like HX using a streak camera setup, adding temporal resolution to the spectrally-resolved emission measurements. The experiments presented here serve as a proof-of-concept for future time-resolved studies of HX species in low-dimensional TMDCs.

4.2.2 Streak camera measurement on bright high-lying excitonic species

Instead of using a CCD camera to measure spectrally-resolved emission from TMDCs, we now employ a streak camera that is synchronized to the excitation laser pulse, thereby adding temporal resolution to the emitted signal. Measurements of *s*-like HX conducted so far are performed under cw excitation. This streak camera approach requires a pulsed laser. Consequently, the exciton density necessary for efficient Auger recombination is only reached during the laser pulse duration, in the fs range, making the detectable signal weaker and more challenging to analyze. To our knowledge, no streak camera data from HX has been recorded in monolayer WSe_2 to date. It is known that the *s*-like HX in naturally 2H-stacked bilayer (2L) WSe_2 is more than one order of magnitude brighter than in monolayer WSe_2 [203]. To demonstrate the feasibility of streak camera measurements on HXs, we perform experiments on 2L WSe_2.

The sample is cooled to 5 K and excited with a pulsed laser of energy 1.717 eV, resonant to the AX, with a power of 1 mW ($400\,\mu J\,cm^{-2}$), repetition rate of 80 MHz and pulse width of 140 fs. The data is collected in the digital photon counting mode of the streak camera: Here, every pixel of the two-dimensional sCMOS sensor that exceeds a certain threshold is counted as a single photon event. To measure long-lasting decays, we use the longest, coarsest time range of the streak camera. The resulting data, obtained after 17 h of integration, is shown in fig. 4.25. A clear, narrow exciton peak is visible, alongside with phonon replicas at smaller energies. The excitonic peaks show no time-dependent changes that are captured by the resolution of this measurement. The main peak is spectrally integrated from 3.192 eV to 3.205 eV and plotted as a function of time. Fitting the decay with a single exponential decay yields a lifetime of (65.0 ± 3.7) ps. This lifetime exceeds lifetimes of bright band-edge excitons by two orders of magnitude [153, 162,

182–186]. Moreover, a bright excitonic species far above the bandgap is expected to have a reduced lifetime due to multiple decay channels in this energy region. The sample emits a weak SHG signal, which is used to estimate the instrument response function of the streak camera. The instrument response function is determined by Gaussian fitting of this signal, yielding a FWHM of (20.4 ± 1.0) ps. The specified temporal resolution of the streak camera used is below 5 ps for the finest time range.

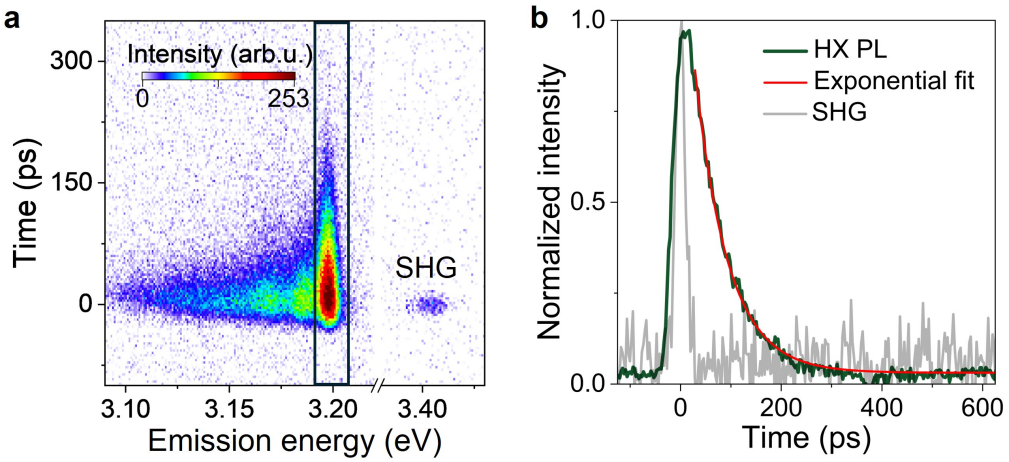

Figure 4.25: **a** Streak camera image of the *s*-like HX in natural 2L WSe_2 at 5 K. The sample is excited resonantly with the AX at 1.717 eV with a pulse length of 140 fs. The spectrally integrated region and the emitted SHG signal are marked. **b** Spectrally integrated intensity of the HX (green line) with an exponential decay fit (red line), yielding a decay time of (65.0 ± 3.7) ps. The gray line shows the SHG signal obtained during the measurement, indicating the instrument response function.

It is known that different stackings influence the energy of HX, as their orbital contribution shows strong out-of-plane character [202]. In order to investigate the effect of twisting on the lifetime of the HX, we measure the *s*-like HX in an artificially stacked bilayer WSe_2 with 3R-stacking. The sample is cooled to 5 K and excited with the same pulsed laser as before, with the

center photon energy set to 1.693 eV, resonant to the AX, with a power of 400 µW (160 µJ cm^{-2}), and an integration time of 3 h. The streak image presented in fig. 4.26 shows a narrow peak with a significantly longer lifetime. An exponential fit of the spectrally integrated data yields a decay time of (368.2 ± 4.1) ps.

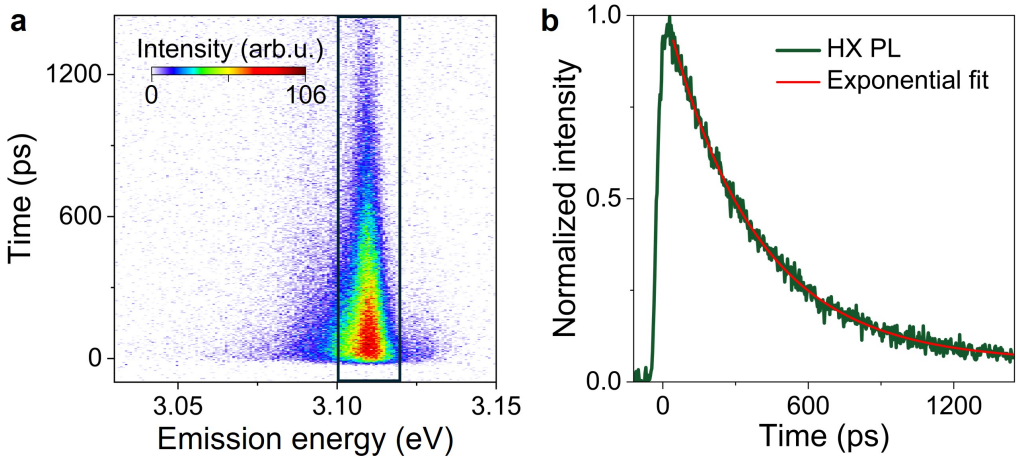

Figure 4.26: **a** Streak camera image of the *s*-like HX in a 3R-stacked bilayer WSe_2 at 5 K obtained under resonant excitation of the AX with 1.693 eV and a power of 400 µW (160 µJ cm^{-2}). The spectrally integrated region is marked. **b** Spectrally integrated exciton signal (green line) with an exponential decay fit (red line), yielding a decay time of (368.2 ± 4.1) ps.

This long lifetime for a bright excitonic species in both 2H and 3R stackings can be explained by their electronic band structure, as illustrated in fig. 4.27. In natural 2H stacking, the K valleys of the bottom layer are located beneath their K′ valleys of the top layer. An exciton formed at the K point is predominately localized within a single layer, since interlayer electron hopping requires a change in spin or momentum. These excitons, thus, have only little interlayer character, leading to faster recombination [203]. In contrast, in 3R stacking the K points are aligned, enabling electrons to tunnel between layers. This gives the exciton an increased interlayer charac-

ter, reducing the electron-hole wavefunction overlap and, thereby, decreasing the recombination rate, which results in a longer lifetime. The assignment of increased interlayer character of HX in 3R-stacked WSe_2 compared to the 2H-stacking is supported by previous observations of the dipole moment, measured under static electric field by my collegue Fabian Buchner. Here, the dipole moment of HX in 3R-stacked WSe_2 is found to be 0.6 e nm, two times larger than in 2H-stacked WSe_2, where the dipole moment of the HX is measured to be 0.3 e nm [203], indicating a stronger separation of electron and hole in the out-of-plane direction.

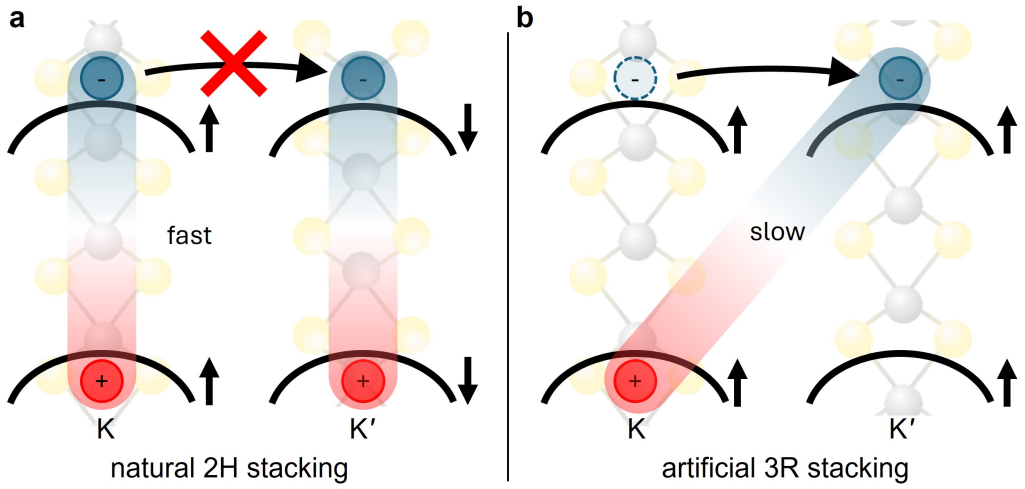

Figure 4.27: **a** Schematic of excitonic transitions in natural 2H-stacked 2L WSe_2. K points are located above K′ points, making interlayer electron hopping spin-forbidden. The resulting intralayer excitons recombine rapidly. **b** In 3R-stacked bilayer WSe_2, the K points are aligned, allowing interlayer electron tunneling and enabling the formation of long-lived interlayer excitons.

The long decay times of HXs in 2L WSe_2 are remarkable, as lifetimes of several tens to hundreds of ps are typically associated with dark excitons in two-dimensional TMDCs [123, 187]. The observed values may be linked to the unique properties of interlayer HXs, underscoring their potential for optoelectronic applications and motivating further studies.

In contrast to the proposed Auger-recombination of excitons at the K point [201], recent work suggests an alternative generation mechanism for HX states in multilayer systems [223]: Two excitons, each consisting of one electron in Q valley and one hole at the Γ point, annihilate and populate a high-lying state at the Γ point. In this scenario, the long-lived signal at the HX energy could be a consequence of a long lifetime and therefore of a slowly decaying population of the dark QΓ excitons, while the high-lying Γ-point exciton itself decays rapidly. In any case, the detection of a long-lived signal in this energy range is noteworthy. However, further investigations are required to definitively determine the origin and formation mechanism of the HX.

CHAPTER 5

Conclusion and outlook

In this thesis, we investigate the optical properties of low-dimensional semiconducting TMDCs. We performed studies using various nonlinear and linear optical spectroscopy techniques. The main focus of this work lies on the investigation of excitonic species formed at roughly twice the energy of the fundamental bandgap, referred to as high-lying excitons. These states form a dark p-like HX and a bright s-like HX. The p-like HX is accessible via two-photon excitation and shows a pronounced influence on the SHG spectrum due to excitonic quantum interference effects [190], which can be rationalized by a three-level system consisting of the ground state, the AX and the p-like HX. The bright s-like HX can be excited via UPL processes and shows a pronounced, narrow emission in the ultraviolet spectral range [201, 202]. Both HX can be efficiently tuned by changing the twist angle in bilayer structures, or by applying external electric field [181, 202, 203].

This thesis expands the current understanding of HX in several ways. The mechanism leading to quantum interference in the three-level system is further understood by investigating the influence of chirped-laser exciation

on the SHG spectrum in section 4.1.1. We investigate an hBN-encapsulated monolayer WSe_2 for different chirp values and find characteristic signatures in the SHG spectrum, depending on the sign of the chirp: Positive chirp introduces one dip in the SHG spectrum while negative chirp leads to two dips. This asymmetry is explained by a small negative detuning between the involved energy levels. The findings are supported by density-matrix calculation, showing good agreement with the experimental results. By analysing the simulated spectra, we rationalize the occurence of dips in the SHG spectrum by jumps of the spectral phase, leading to dips in the group delay, which can be explained by Rabi oscillations in the three-level system, as explained in section 2.5.2.

Most studies on HX so far focus on monolayer WSe_2 with short investigations of $MoSe_2$. Given the similarities in band structure of semiconducting TMDC materials, it is of high interest to investigate other members of this material class and look for traces of HX. In section 4.1.2 we perform optical spectroscopy measurements on monolayer $MoSe_2$, $MoTe_2$, WS_2 and MoS_2, all encaspulated in hBN. We identify the AX via PL spectroscopy and try to investigate the *s*-like HX via UPL. To investigate the *p*-like HX, we perform SHG measurements and search for anticrossing features, indicating the presence of a three-level system [190]. Furthermore, we analyze the power-law exponent of the SHG signal, which shows characteristic signatures at the energy of the AX and the *p*-like HX, which is explained in section 2.5.

We find signatures of HX in all investigated materials, which differ slightly in their energetic position with respect to the AX. To highlight, we find a pronounced anticrossing of the SHG spectrum obtained from MoS_2 indicating that the resonance condition required for quantum interference is fulfilled. This material shows a positive detuning $\Delta E = 32\,\mathrm{meV}$, comparable to values that are known to allow quantum interference in WSe_2 [190, 202]. Power-law analysis reveals that all other investigated materials show a negative detuning, explaining the absence of quantum interference effects in the cor-

responding three-level system.

The second part of the experimental results provides insights on the temporal dynamics of HX. We use a two-laser pump-probe setup to investigate the influence of excitonic resonances on the intensity of nonlinear signals like SFG and FWM in section 4.2.1. We find that under resonant excitation of the AX a time delay between pump laser and probe laser of $\Delta t = 120\,\mathrm{fs}$ is required to maximize the SFG signal. For two-photon resonant excitation of the *p*-like HX the FWM signal is maximal, if the delay time between pump and probe is $\Delta t = 80\,\mathrm{fs}$. The required time delays depend on the excitation power and wavelength of the resonant excitation laser. Our findings are supported by density-matrix calculations, showing good agreement with the experimental results. We attribute the required time delay to Rabi oscillations between the states, which shifts their maximal population to times different from zero. We find that the delay time for maximal nonlinear signals is dependent on the lifteimes of the involved states, making this method a tool to determine the lifetime of one- and two-photon allowed states.

Finally, we investigate the temporal dynamics of the bright *s*-like HX in natural 2H-stacked bilayer and artificial 3R-stacked bilayer WSe_2, as shown in section 4.2.2. We use a streak camera to directly measure the time-resolved emission of the *s*-like HX after upconversion excitation of the AX. We find a lifetime of $(67.4 \pm 3.7)\,\mathrm{ps}$ in the 2H sample and a significantly longer lifetime of $(373.2 \pm 4.1)\,\mathrm{ps}$ in the 3R sample. Both lifetimes are significantly longer than the lifetime of the AX in monolayer WSe_2, which is on the order of a few picoseconds [153, 162, 182–186]. We attribute the long lifetimes to an interlayer character of the HX in the 2H bilayer [203] which is even more pronounced in the 3R bilayer, due to the specific stacking order. However, the formation mechanism of the HX in multilayers is under debate [223] and requires further investigations.

The investigation of HX, as presented in this thesis opens new questions and avenues for future research and development. What is the population

mechanism of the bright *s*-like HX in monolayers and multilayers? While the assignment of the *s*-like HX to the CB+2 at the K point in monolayer WSe_2 is rationalized by bandstructure calculations [201, 202], the formation mechanism in multilayer structures is reported to be different [223]: Dark excitons are proposed to act as a population reservoir for the HX in samples with more than two layers, which consequently will form at the Γ point. These different formation paths will result in different time dynamics, that might be resolved by streak camera masurements of the HX in these samples.

What is the influence of the HX on other excitonic species? We have shown that the occurrence of HX species is a general phenomenon in semiconducting TMDC monolayers. Under resonant excitation of the transition between the AX and the *p*-like HX, the states will be strongly coupled via Rabi oscillations. This dressing of the AX might influence the properties of the state itself. Does this effect need to be considered in the analysis of resonant investigation of band-edge species? This question could be addressed by investigating the absorption of the AX under strong pumping of the transition between AX and *p*-like HX, which is currently done by Lucia Sichert in our group.

Can we use the three-level system to realize lasing without inversion [224, 225] in TMDC monolayers? Here, light can be amplified without having more population in the excited state than in the ground state, by making use of quantum interference effects that cancel absorption effects while keeping the stimulated emission intact. Investigation of additional tuning paramteres could lead to control of the quantum interference effect and might allow the realization of such a laser system in TMDC monolayers.

In summary, the investigation of HXs in low-dimensional semiconductors is a promising field of research, that can lead to new fundamental insights in exciton physics but also might open new avenues for applications in nanophotonics and quantum optics.

APPENDIX A

Sample preparation

In order to fabricate the investigated samples, several techniques where applied. The toolbox used to cleave monolayers from bulk crystals and consequently assemble the low-dimensional crystals into complex structures, is presented in this chapter.

A.1 Mechanical exfoliation of layered materials

Several techniques to obtain few-layers of vdW materials are used in the community. We solely focus on dry-cleaving processes that uses the weak vdW bindings of the material, using mechanical force to reduce the layer number. The two main methods, exfoliation on PDMS, following [52], and exfoliation on SiO_2, following [54], are presented.

Bulk crystals of TMDC materials in good quality are commercially available from *HQ graphene*. HBN crystals are kindly provided by *NIMS, Japan*,

graphite flakes are purchased from *NGS trading & Consulting GmbH*. We attach *SCOTCH tape* trademarked by *3M* on both sides of the thick bulk crystal. By tearing the tapes apart, the thickness of the bulk crystal is reduced, ensuring that the surface is smooth and clean. This process is repeated by attaching a *Nitto tape (Nitto Denko, SVP 224P)* with smaller adhesion to the crystal, further reducing the thickness of the material.

Next, we place a small piece of polydimethylsiloxan (PDMS) *(Gel-Pak, Gel-film X4)* on a microscope slide and attach the crystal on the Nitto tape to the PDMS. The stack is carefully pressed by a small force, to ensure good contact between PDMS and crystal. By slowly pealing the tape off the PDMS with an approximate speed of $10\,\frac{\mathrm{cm}}{\mathrm{s}}$, some parts of the crystal will stay on the PDMS, as its adhesion can be controlled by the pealing speed, due to its viscoelastic properties. One has to develop a feeling for the correct speed. If only small parts of the crystal stay on the PDMS, the speed has to be increased. If many crystals stay on the PDMS, or the crystals appear to be rough or broken, the speed has to be reduced. The tape can be attached to the PDMS and pealed off again, if no monolayer was present. The crystal is analyzed under an optical light microscope in reflection geometry. Due to the increasing transparency with decreasing layer number, one can easily identify monolayers or few-layers by the optical contrast. The PDMS technique can lead to large TMDC monolayer flakes, with edge lengths on the order of several tens to hundreds of µm within a short period of time, making the technique valuable for quick fabrication of simple structures, for example hBN-encapsulated TMDC monolayers. However, we found that residual PDMS remains on the flakes, which makes it challenging to fabricate samples with more than three layers stacked together, as no clean spot is present.

Therefore, we established a second method to fabricate clean monolayer flakes. The SiO_2-assisted exfoliation technique results in very clean flakes that can be used for the fabrication of samples with many layers. The technique

produces smaller TMDC flakes on the order of 10 µm by 10 µm. The yield is also orders of magnitude smaller than for the PDMS-assisted method. One of the most time-consuming steps is the cleaning of the SiO_2 substrates. After cutting the wafer *(Siegert Wafer)* into small 1 cm^2 pieces, they are cleaned in three consecutive baths of acetone, followed by a 1 min cleaning in an ultrasonic bath. Then the procedure is repeated with three baths of isopropanol and consecutive ultrasonic bath. Residues of the solvents are removed from the sample with two baths of deionized water. The wafers are dried with nitrogen. Finally, the wafers are treated with oxygen plasma to remove any remaining organic residues.

Next, one needs to prepare the bulk crystals on the tape. We found, that a sticky *SCOTCH tape* suits best to exfoliate TMDC materials. For hBN and graphite, the *Nitto ELP BT-130E-SL* is suited best. The bulk crystal needs to be flat and smooth without being broken. The best results are achieved if the material is thin enough that the crystal appears colorful. The cut and cleaned SiO_2 substrates are placed onto a heating plate at 120 °C. The tapes are attached to the hot substrate. They can be pressed with a small, but isotropic force, to increase the contact. If the crystals appear to be broken into small pieces, the force should be reduced. Once the substrate is cooled down, the tapes are peeled off. The speed is not too crucial for this method. Few-layer crystals remaining on the SiO_2 substrate can be identified by analysing the optical contrast, as seen through an optical light microscope.

Once suitable flakes are found, they might need to be combined and transferred onto a different substrate. The possible techniques will be presented in the following.

A.2 Transfer of layered materials to different substrates

In most cases, the substrates used to exfoliate layered materials and substrates used for measurements require different properties. Therefore, it is necessary to transfer the flakes from one substrate to another. Also, if several flakes need to be combined, suitable methods need to be implemented. These methods are highly linked to the technique used to exfoliate the materials.

In order to transfer flakes from PDMS to a silicon substrate, the viscoelastic properties of the PDMS is used again. The microscope slide with the PDMS pointing downwards is placed over the silicon substrate that is mounted on a rotational heating stage. The PDMS is slowly lowered until it is in contact with the SiO_2, which can be seen by the optical microscope as a change in optical contrast. Once the sample is perfectly aligned and fully in contact, the microscope slide is very slowly pulled away. If done right, the flakes will stay on the target substrate [52]. The sample can be heated up to 60 °C in order to ensure a slow and smooth movement of the contact area due to thermal expansion. Slow cooling of the sample back to room temperature is useful to slowly transfer the sample. Once the sample is attached to the silicon substrate, it can be used for measurements. Additional flakes can be added for more complex structures, or the flake can be further transferred, as follows.

In order to transfer flakes from a SiO_2 substrate to a different target substrate, we apply the so called *hot pick-up method*, following [55]. In general there are no differences whether the sample was exfoliated, transferred, or grown by chemical methods onto the SiO_2. We use the increasing adhesion of polycarbonate (PC) at elevated temperatures. To ensure easy handling, precise positioning and reproducible results, the following measures are taken. We put a cleaned microscope slide on a heating plate at temperatures of 120 °C and add a small drop of a mixed two-component PDMS solution

(*Sylgard 184*) on the slide. Due to the reduced cure time of PDMS at high temperatures, a dome-shaped structure evolves. The diameter should be on the order of 3 mm. The height should be 2 mm. The size can be controlled by temperature of the heating plate and amount of PDMS. Next, we create a 6 % solution of PC in chloroform. We put roughly 10 drops of the PC solution on a microscope slide, attach a second microscope slide on the top and slide it with respect to the first microscope slide, in order to fabricate a thin, homogeneous PC film. Next, we cut a circle, slightly larger than the PDMS dome, out of the PC film and support it on the edges with a Scotch tape. We put the PC film onto the PDMS dome without breaking the film or adding any kind of wrinkles. The stack is kept at a constant temperature of 120 °C. We align the stack over the exfoliated flakes and bring them in contact. If done properly, the flake will stick to the PC. Complex structures can be fabricated by picking up of consecutive flakes from top to bottom. Precise planning and alignment is required.

Once the last flake is attached to the PC, the stack is brought into contact with the target substrate. The temperature is increased to 160 °C. By carefully lifting the stack with respect to the substrate, a brown circle, indicating the contact front between PC and PDMS is visible. Once the PC is completely detached from the PDMS, the PC is melted on the edges of the contact area with the target substrate by increasing the temperature to 180 °C and slowly lifting the microscope slide. Once the sample is transferred from the PC to the goal substrate, it is cleaned with chloroform and blow-dried with nitrogen.

Bibliography

1. Genesis. “The Holy Bible”. *NIV,* 1:3–4.
2. John. “The Holy Bible”. *NIV,* 1:4–9.
3. Psalm. “The Holy Bible”. *NIV,* 119:115.
4. Ephesians. “The Holy Bible”. *NIV,* 5:8–9.
5. Hubble, E. “A relation between distance and radial velocity among extra-galactic nebulae”. *Proceedings of the National Academy of Sciences of the United States of America* **15,** 168–173 (1929).
6. Einstein, A. “Über einen die Erzeugung und Verwandlung des Lichtes betreffenden heuristischen Gesichtspunkt”. *Annalen der Physik* **322,** 132–148 (1905).
7. Basov, D. N., Averitt, R. D. & Hsieh, D. “Towards properties on demand in quantum materials”. *Nature Materials* **16,** 1077–1088 (2017).
8. Rydberg, J. R. “On the structure of the line-spectra of the chemical elements”. *The London, Edinburgh, and Dublin Philosophical Magazine and Journal of Science* **29,** 331–337 (1890).
9. Scully, M. O. & Zubairy, M. S. *Quantum optics* (Cambridge and New York, 1997).
10. MAIMAN, T. H. “Stimulated Optical Radiation in Ruby”. *Nature* **187,** 493–494 (1960).

11. Schawlow, A. L. & Townes, C. H. “Infrared and Optical Masers”. *Physical Review* **112,** 1940–1949 (1958).

12. Gyongyosi, L. & Imre, S. “A Survey on quantum computing technology”. *Computer Science Review* **31,** 51–71 (2019).

13. Huang, H.-L., Wu, D., Fan, D. & Zhu, X. “Superconducting quantum computing: a review”. *Science China Information Sciences* **63,** 1–32 (2020).

14. De Leon, N. P., Itoh, K. M., Kim, D., Mehta, K. K., Northup, T. E., Paik, H., Palmer, B. S., Samarth, N., Sangtawesin, S. & Steuerman, D. W. “Materials challenges and opportunities for quantum computing hardware”. *Science (New York, N.Y.)* **372,** 2823 (2021).

15. Žutić, I., Fabian, J. & Das Sarma, S. “Spintronics: Fundamentals and applications”. *Reviews of Modern Physics* **76,** 323–410 (2004).

16. Awschalom, D. D. & Flatté, M. E. “Challenges for semiconductor spintronics”. *Nature Physics* **3,** 153–159 (2007).

17. Pulizzi, F. “Spintronics”. *Nature Materials* **11,** 367 (2012).

18. Walmsley, I. A. “Quantum optics: science and technology in a new light”. *Science (New York, N.Y.)* **348,** 525–530 (2015).

19. Maser, A., Gmeiner, B., Utikal, T., Götzinger, S. & Sandoghdar, V. “Few-photon coherent nonlinear optics with a single molecule”. *Nature Photonics* **10,** 450–453 (2016).

20. Ying, Z., Feng, C., Zhao, Z., Dhar, S., Dalir, H., Gu, J., Cheng, Y., Soref, R., Pan, D. Z. & Chen, R. T. “Electronic-photonic arithmetic logic unit for high-speed computing”. *Nature Communications* **11,** 2154 (2020).

21. Zasedatelev, A. V., Baranikov, A. V., Sannikov, D., Urbonas, D., Scafirimuto, F., Shishkov, V. Y., Andrianov, E. S., Lozovik, Y. E., Scherf, U., Stöferle, T., Mahrt, R. F. & Lagoudakis, P. G. "Single-photon nonlinearity at room temperature". *Nature* **597,** 493–497 (2021).

22. Knox, R. S. "Wannier Excitons in Simple van der Waals Crystals". *Radiation Research* **20,** 77 (1963).

23. Knox, R. S. *Theory of excitons / Robert S. Knox* (New York, 1963).

24. Yu, P. Y. & Cardona, M. *Fundamentals of semiconductors. Physics and materials properties* 4th ed. (Berlin and New York, 2010).

25. Green, M. A. "Silicon solar cells: evolution, high-efficiency design and efficiency enhancements". *Semiconductor Science and Technology* **8,** 1–12 (1993).

26. High, A. A., Novitskaya, E. E., Butov, L. V., Hanson, M. & Gossard, A. C. "Control of exciton fluxes in an excitonic integrated circuit". *Science (New York, N.Y.)* **321,** 229–231 (2008).

27. Kuznetsova, Y. Y., Remeika, M., High, A. A., Hammack, A. T., Butov, L. V., Hanson, M. & Gossard, A. C. "All-optical excitonic transistor". *Optics letters* **35,** 1587–1589 (2010).

28. Stillman, G. E., Wolfe, C. M. & Dimmock, J. O. "Hall coefficient factor for polar mode scattering in n-type GaAs". *Journal of Physics and Chemistry of Solids* **31,** 1199–1204 (1970).

29. Nam, S. B., Reynolds, D. C., Litton, C. W., Almassy, R. J., Collins, T. C. & Wolfe, C. M. "Free-exciton energy spectrum in GaAs". *Physical Review B* **13,** 761–767 (1976).

30. Sugie, A., Nakano, K., Tajima, K., Osaka, I. & Yoshida, H. "Dependence of Exciton Binding Energy on Bandgap of Organic Semiconductors". *The journal of physical chemistry letters* **14,** 11412–11420 (2023).

31. Tsumura, A., Koezuka, H. & Ando, T. “Macromolecular electronic device: Field-effect transistor with a polythiophene thin film”. *Applied Physics Letters* **49,** 1210–1212 (1986).

32. Hu, P., He, X. & Jiang, H. “Greater than 10 cm^2 V^{-1} s^{-1} : A breakthrough of organic semiconductors for field–effect transistors”. *InfoMat* **3,** 613–630 (2021).

33. Ramasubramaniam, A. “Large excitonic effects in monolayers of molybdenum and tungsten dichalcogenides”. *Physical Review B* **86,** 115409 (2012).

34. Shi, H., Pan, H., Zhang, Y.-W. & Yakobson, B. I. “Quasiparticle band structures and optical properties of strained monolayer MoS_2 and WS_2”. *Physical Review B* **87,** 155304 (2013).

35. Zhu, B., Chen, X. & Cui, X. “Exciton binding energy of monolayer WS_2”. *Scientific Reports* **5,** 9218 (2015).

36. Yu, Z., Ong, Z.-.-Y., Li, S., Xu, J.-.-B., Zhang, G., Zhang, Y.-.-W., Shi, Y. & Wang, X. “Analyzing the Carrier Mobility in Transition–Metal Dichalcogenide MoS_2 Field–Effect Transistors”. *Advanced Functional Materials* **27,** 1604093 (2017).

37. Li, X., Mullen, J. T., Jin, Z., Borysenko, K. M., Buongiorno Nardelli, M. & Kim, K. W. “Intrinsic electrical transport properties of monolayer silicene and MoS_2 from first principles”. *Physical Review B* **87,** 115418 (2013).

38. Chernikov, A., Berkelbach, T. C., Hill, H. M., Rigosi, A., Li, Y., Aslan, O. B., Reichman, D. R., Hybertsen, M. S. & Heinz, T. F. “Exciton binding energy and nonhydrogenic Rydberg series in monolayer WS_2”. *Physical review letters* **113,** 076802 (2014).

39. Novoselov, K. S., Geim, A. K., Morozov, S. V., Jiang, D., Zhang, Y., Dubonos, S. V., Grigorieva, I. V. & Firsov, A. A. "Electric Field Effect in Atomically Thin Carbon Films". *Science (New York, N.Y.)* **306,** 666–669 (2004).

40. Novoselov, K. S., Jiang, D., Schedin, F., Booth, T. J., Khotkevich, V. V., Morozov, S. V. & Geim, A. K. "Two-dimensional atomic crystals". *Proceedings of the National Academy of Sciences of the United States of America* **102,** 10451–10453 (2005).

41. Novoselov, K. S., Geim, A. K., Morozov, S. V., Jiang, D., Katsnelson, M. I., Grigorieva, I. V., Dubonos, S. V. & Firsov, A. A. "Two-dimensional gas of massless Dirac fermions in graphene". *Nature* **438,** 197–200 (2005).

42. Geim, A. K. & Novoselov, K. S. "The rise of graphene". *Nature materials* **6,** 183–191 (2007).

43. Joseph, S., Mohan, J., Lakshmy, S., Thomas, S., Chakraborty, B., Thomas, S. & Kalarikkal, N. "A review of the synthesis, properties, and applications of 2D transition metal dichalcogenides and their heterostructures". *Materials Chemistry and Physics* **297,** 127332 (2023).

44. Cho, A. Y. "Morphology of Epitaxial Growth of GaAs by a Molecular Beam Method: The Observation of Surface Structures". *Journal of Applied Physics* **41,** 2780–2786 (1970).

45. Gonser, U., Osgood, R. M., Panish, M. B., Sakaki, H., Lotsch, H. K. V., Herman, M. A. & Sitter, H. *Molecular Beam Epitaxy* (Berlin, Heidelberg, 1996).

46. Henini, M. "Molecular beam epitaxy from research to mass-production — Part 1". *III-Vs Review* **9,** 32–34 (1996).

47. Geim, A. K. & Grigorieva, I. V. "Van der Waals heterostructures". *Nature* **499,** 419–425 (2013).

48. Liu, Y., Weiss, N. O., Duan, X., Cheng, H.-C., Huang, Y. & Duan, X. "Van der Waals heterostructures and devices". *Nature Reviews Materials* **1,** 1–17 (2016).

49. Frisenda, R., Niu, Y., Gant, P., Muñoz, M. & Castellanos-Gomez, A. "Naturally occurring van der Waals materials". *npj 2D Materials and Applications* **4,** 1–13 (2020).

50. Pizzocchero, F., Gammelgaard, L., Jessen, B. S., Caridad, J. M., Wang, L., Hone, J., Bøggild, P. & Booth, T. J. "The hot pick-up technique for batch assembly of van der Waals heterostructures". *Nature Communications* **7,** 11894 (2016).

51. Wang, L., Meric, I., Huang, P. Y., Gao, Q., Gao, Y., Tran, H., Taniguchi, T., Watanabe, K., Campos, L. M., Muller, D. A., Guo, J., Kim, P., Hone, J., Shepard, K. L. & Dean, C. R. "One-dimensional electrical contact to a two-dimensional material". *Science (New York, N.Y.)* **342,** 614–617 (2013).

52. Castellanos-Gomez, A., Buscema, M., Molenaar, R., Singh, V., Janssen, L., van der Zant, H. S. J. & Steele, G. A. "Deterministic transfer of two-dimensional materials by all-dry viscoelastic stamping". *2D Materials* **1,** 011002 (2014).

53. Castellanos-Gomez, A., Vicarelli, L., Prada, E., Island, J. O., Narasimha-Acharya, K. L., Blanter, S. I., Groenendijk, D. J., Buscema, M., Steele, G. A., Alvarez, J. V., Zandbergen, H. W., Palacios, J. J. & van der Zant, H. S. J. "Isolation and characterization of few-layer black phosphorus". *2D Materials* **1,** 025001 (2014).

54. Huang, Y., Sutter, E., Shi, N. N., Zheng, J., Yang, T., Englund, D., Gao, H.-J. & Sutter, P. "Reliable Exfoliation of Large-Area High-Quality Flakes of Graphene and Other Two-Dimensional Materials". *ACS Nano* **9,** 10612–10620 (2015).

55. Purdie, D. G., Pugno, N. M., Taniguchi, T., Watanabe, K., Ferrari, A. C. & Lombardo, A. "Cleaning interfaces in layered materials heterostructures". *Nature Communications* **9,** 5387 (2018).

56. Zhao, Q., Wang, T., Ryu, Y. K., Frisenda, R. & Castellanos-Gomez, A. "An inexpensive system for the deterministic transfer of 2D materials". *Journal of Physics: Materials* **3,** 016001 (2020).

57. Wang, W. *et al.* "Clean assembly of van der Waals heterostructures using silicon nitride membranes". *Nature Electronics* **6,** 981–990 (2023).

58. Tran, K. *et al.* "Evidence for moiré excitons in van der Waals heterostructures". *Nature* **567,** 71–75 (2019).

59. Carr, S., Fang, S. & Kaxiras, E. "Electronic-structure methods for twisted moiré layers". *Nature Reviews Materials* **5,** 748–763 (2020).

60. Baek, H., Brotons-Gisbert, M., Koong, Z. X., Campbell, A., Rambach, M., Watanabe, K., Taniguchi, T. & Gerardot, B. D. "Highly energy-tunable quantum light from moiré-trapped excitons". *Science advances* **6,** 8526 (2020).

61. McGilly, L. J. *et al.* "Visualization of moiré superlattices". *Nature Nanotechnology* **15,** 580–584 (2020).

62. Andrei, E. Y., Efetov, D. K., Jarillo-Herrero, P., MacDonald, A. H., Mak, K. F., Senthil, T., Tutuc, E., Yazdani, A. & Young, A. F. "The marvels of moiré materials". *Nature Reviews Materials* **6,** 201–206 (2021).

63. Lau, C. N., Bockrath, M. W., Mak, K. F. & Zhang, F. "Reproducibility in the fabrication and physics of moiré materials". *Nature* **602,** 41–50 (2022).

64. Mak, K. F. & Shan, J. "Semiconductor moiré materials". *Nature Nanotechnology* **17,** 686–695 (2022).

65. Regan, E. C. *et al.* "Mott and generalized Wigner crystal states in WSe_2/WS_2 moiré superlattices". *Nature* **579,** 359–363 (2020).

66. Smoleński, T., Dolgirev, P. E., Kuhlenkamp, C., Popert, A., Shimazaki, Y., Back, P., Lu, X., Kroner, M., Watanabe, K., Taniguchi, T., Esterlis, I., Demler, E. & Imamoğlu, A. "Signatures of Wigner crystal of electrons in a monolayer semiconductor". *Nature* **595,** 53–57 (2021).

67. Miao, S., Wang, T., Huang, X., Chen, D., Lian, Z., Wang, C., Blei, M., Taniguchi, T., Watanabe, K., Tongay, S., Wang, Z., Di Xiao, Cui, Y.-T. & Shi, S.-F. "Strong interaction between interlayer excitons and correlated electrons in WSe_2/WS_2 moiré superlattice". *Nature Communications* **12,** 3608 (2021).

68. Li, H., Li, S., Regan, E. C., Wang, D., Zhao, W., Kahn, S., Yumigeta, K., Blei, M., Taniguchi, T., Watanabe, K., Tongay, S., Zettl, A., Crommie, M. F. & Wang, F. "Imaging two-dimensional generalized Wigner crystals". *Nature* **597,** 650–654 (2021).

69. Cao, Y., Fatemi, V., Fang, S., Watanabe, K., Taniguchi, T., Kaxiras, E. & Jarillo-Herrero, P. "Unconventional superconductivity in magic-angle graphene superlattices". *Nature* **556,** 43–50 (2018).

70. Cao, Y., Fatemi, V., Demir, A., Fang, S., Tomarken, S. L., Luo, J. Y., Sanchez-Yamagishi, J. D., Watanabe, K., Taniguchi, T., Kaxiras, E., Ashoori, R. C. & Jarillo-Herrero, P. "Correlated insulator behaviour at half-filling in magic-angle graphene superlattices". *Nature* **556,** 80–84 (2018).

71. Wu, F., Lovorn, T., Tutuc, E. & MacDonald, A. H. "Hubbard Model Physics in Transition Metal Dichalcogenide Moiré Bands". *Physical review letters* **121,** 026402 (2018).

72. Yankowitz, M., Chen, S., Polshyn, H., Zhang, Y., Watanabe, K., Taniguchi, T., Graf, D., Young, A. F. & Dean, C. R. "Tuning superconductivity in

twisted bilayer graphene". *Science (New York, N.Y.)* **363,** 1059–1064 (2019).

73. Wang, L. *et al.* "Correlated electronic phases in twisted bilayer transition metal dichalcogenides". *Nature Materials* **19,** 861–866 (2020).

74. Xu, Y., Liu, S., Rhodes, D. A., Watanabe, K., Taniguchi, T., Hone, J., Elser, V., Mak, K. F. & Shan, J. "Correlated insulating states at fractional fillings of moiré superlattices". *Nature* **587,** 214–218 (2020).

75. Balents, L., Dean, C. R., Efetov, D. K. & Young, A. F. "Superconductivity and strong correlations in moiré flat bands". *Nature Physics* **16,** 725–733 (2020).

76. Zhang, Y., Yuan, N. F. Q. & Fu, L. "Moiré quantum chemistry: Charge transfer in transition metal dichalcogenide superlattices". *Physical Review B* **102,** 201115 (2020).

77. Pan, H., Wu, F. & Das Sarma, S. "Quantum phase diagram of a Moiré-Hubbard model". *Physical Review B* **102,** 201104 (2020).

78. Morales-Durán, N., MacDonald, A. H. & Potasz, P. "Metal-insulator transition in transition metal dichalcogenide heterobilayer moiré superlattices". *Physical Review B* **103,** L241110 (2021).

79. Tang, Y., Li, L., Li, T., Xu, Y., Liu, S., Barmak, K., Watanabe, K., Taniguchi, T., MacDonald, A. H., Shan, J. & Mak, K. F. "Simulation of Hubbard model physics in WSe_2/WS_2 moiré superlattices". *Nature* **579,** 353–358 (2020).

80. Jin, C., Tao, Z., Li, T., Xu, Y., Tang, Y., Zhu, J., Liu, S., Watanabe, K., Taniguchi, T., Hone, J. C., Fu, L., Shan, J. & Mak, K. F. "Stripe phases in WSe_2/WS_2 moiré superlattices". *Nature Materials* **20,** 940–944 (2021).

81. Wietek, A., Rossi, R., Šimkovic, F., Klett, M., Hansmann, P., Ferrero, M., Stoudenmire, E. M., Schäfer, T. & Georges, A. "Mott Insulating States with Competing Orders in the Triangular Lattice Hubbard Model". *Physical Review X* **11,** 041013 (2021).

82. Nagler, P., Plechinger, G., Ballottin, M. V., Mitioglu, A., Meier, S., Paradiso, N., Strunk, C., Chernikov, A., Christianen, P. C. M., Schüller, C. & Korn, T. "Interlayer exciton dynamics in a dichalcogenide monolayer heterostructure". *2D Materials* **4,** 025112 (2017).

83. Miller, B., Steinhoff, A., Pano, B., Klein, J., Jahnke, F., Holleitner, A. & Wurstbauer, U. "Long-Lived Direct and Indirect Interlayer Excitons in van der Waals Heterostructures". *Nano letters* **17,** 5229–5237 (2017).

84. Mueller, T. & Malic, E. "Exciton physics and device application of two-dimensional transition metal dichalcogenide semiconductors". *npj 2D Materials and Applications* **2,** 1–12 (2018).

85. Deilmann, T. & Thygesen, K. S. "Interlayer Excitons with Large Optical Amplitudes in Layered van der Waals Materials". *Nano letters* **18,** 2984–2989 (2018).

86. Kunstmann, J., Mooshammer, F., Nagler, P., Chaves, A., Stein, F., Paradiso, N., Plechinger, G., Strunk, C., Schüller, C., Seifert, G., Reichman, D. R. & Korn, T. "Momentum-space indirect interlayer excitons in transition-metal dichalcogenide van der Waals heterostructures". *Nature Physics* **14,** 801–805 (2018).

87. Choi, J. *et al.* "Twist Angle-Dependent Interlayer Exciton Lifetimes in van der Waals Heterostructures". *Physical review letters* **126,** 047401 (2021).

88. Jiang, Y., Chen, S., Zheng, W., Zheng, B. & Pan, A. "Interlayer exciton formation, relaxation, and transport in TMD van der Waals heterostructures". *Light: Science & Applications* **10,** 72 (2021).

89. Montblanch, A. R.-P. *et al.* "Confinement of long-lived interlayer excitons in WS_2/WSe_2 heterostructures". *Communications Physics* **4,** 1–8 (2021).

90. Barré, E., Karni, O., Liu, E., O'Beirne, A. L., Chen, X., Ribeiro, H. B., Yu, L., Kim, B., Watanabe, K., Taniguchi, T., Barmak, K., Lui, C. H., Refaely-Abramson, S., Da Jornada, F. H. & Heinz, T. F. "Optical absorption of interlayer excitons in transition-metal dichalcogenide heterostructures". *Science (New York, N.Y.)* **376,** 406–410 (2022).

91. Policht, V. R., Mittenzwey, H., Dogadov, O., Katzer, M., Villa, A., Li, Q., Kaiser, B., Ross, A. M., Scotognella, F., Zhu, X., Knorr, A., Selig, M., Cerullo, G. & Dal Conte, S. "Time-domain observation of interlayer exciton formation and thermalization in a $MoSe_2/WSe_2$ heterostructure". *Nature Communications* **14,** 7273 (2023).

92. Lin, Y., Ling, X., Yu, L., Huang, S., Hsu, A. L., Lee, Y.-H., Kong, J., Dresselhaus, M. S. & Palacios, T. "Dielectric screening of excitons and trions in single-layer MoS_2". *Nano letters* **14,** 5569–5576 (2014).

93. Kylänpää, I. & Komsa, H.-P. "Binding energies of exciton complexes in transition metal dichalcogenide monolayers and effect of dielectric environment". *Physical Review B* **92,** 205418 (2015).

94. Rösner, M., Steinke, C., Lorke, M., Gies, C., Jahnke, F. & Wehling, T. O. "Two-Dimensional Heterojunctions from Nonlocal Manipulations of the Interactions". *Nano letters* **16,** 2322–2327 (2016).

95. Raja, A. *et al.* "Coulomb engineering of the bandgap and excitons in two-dimensional materials". *Nature Communications* **8,** 15251 (2017).

96. Raja, A., Waldecker, L., Zipfel, J., Cho, Y., Brem, S., Ziegler, J. D., Kulig, M., Taniguchi, T., Watanabe, K., Malic, E., Heinz, T. F., Berkelbach, T. C. & Chernikov, A. "Dielectric disorder in two-dimensional materials". *Nature Nanotechnology* **14,** 832–837 (2019).

97. Riis-Jensen, A. C., Lu, J. & Thygesen, K. S. "Electrically controlled dielectric band gap engineering in a two-dimensional semiconductor". *Physical Review B* **101,** 121110 (2020).

98. Popert, A., Shimazaki, Y., Kroner, M., Watanabe, K., Taniguchi, T., Imamoğlu, A. & Smoleński, T. "Optical Sensing of Fractional Quantum Hall Effect in Graphene". *Nano letters* **22,** 7363–7369 (2022).

99. Li, X., Tao, L., Chen, Z., Fang, H., Li, X., Wang, X., Xu, J.-B. & Zhu, H. "Graphene and related two-dimensional materials: Structure-property relationships for electronics and optoelectronics". *Applied Physics Reviews* **4,** 021306 (2017).

100. Huang, B., Clark, G., Navarro-Moratalla, E., Klein, D. R., Cheng, R., Seyler, K. L., Zhong, D., Schmidgall, E., McGuire, M. A., Cobden, D. H., Yao, W., Di Xiao, Jarillo-Herrero, P. & Xu, X. "Layer-dependent ferromagnetism in a van der Waals crystal down to the monolayer limit". *Nature* **546,** 270–273 (2017).

101. Li, L., Yu, Y., Ye, G. J., Ge, Q., Ou, X., Wu, H., Feng, D., Chen, X. H. & Zhang, Y. "Black phosphorus field-effect transistors". *Nature Nanotechnology* **9,** 372–377 (2014).

102. Wang, Q. H., Kalantar-Zadeh, K., Kis, A., Coleman, J. N. & Strano, M. S. "Electronics and optoelectronics of two-dimensional transition metal dichalcogenides". *Nature Nanotechnology* **7,** 699–712 (2012).

103. Novoselov, K. S., Mishchenko, A., Carvalho, A. & A. H. Castro Neto. "2D materials and van der Waals heterostructures". *Science (New York, N.Y.)* **353,** 9439 (2016).

104. Britnell, L., Ribeiro, R. M., Eckmann, A., Jalil, R., Belle, B. D., Mishchenko, A., Kim, Y.-J., Gorbachev, R. V., Georgiou, T., Morozov, S. V., Grigorenko, A. N., Geim, A. K., Casiraghi, C., Castro Neto, A. H. & Novoselov, K. S. "Strong light-matter interactions in

heterostructures of atomically thin films". *Science (New York, N.Y.)* **340,** 1311–1314 (2013).

105. Hu, Z., Wu, Z., Han, C., He, J., Ni, Z. & Chen, W. "Two-dimensional transition metal dichalcogenides: interface and defect engineering". *Chemical Society Reviews* **47,** 3100–3128 (2018).

106. Wang, X., Yasuda, K., Zhang, Y., Liu, S., Watanabe, K., Taniguchi, T., Hone, J., Fu, L. & Jarillo-Herrero, P. "Interfacial ferroelectricity in rhombohedral-stacked bilayer transition metal dichalcogenides". *Nature Nanotechnology* **17,** 367–371 (2022).

107. Xia, F., Wang, H., Di Xiao, Dubey, M. & Ramasubramaniam, A. "Two-dimensional material nanophotonics". *Nature Photonics* **8,** 899–907 (2014).

108. Bhimanapati, G. R. *et al.* "Recent Advances in Two-Dimensional Materials beyond Graphene". *ACS Nano* **9,** 11509–11539 (2015).

109. Frindt, R. F. "Single Crystals of MoS_2 Several Molecular Layers Thick". *Journal of Applied Physics* **37,** 1928–1929 (1966).

110. Wilson, J. A. & Yoffe, A. D. "The transition metal dichalcogenides discussion and interpretation of the observed optical, electrical and structural properties". *Advances in Physics* **18,** 193–335 (1969).

111. Bromley, R. A., Murray, R. B. & Yoffe, A. D. "The band structures of some transition metal dichalcogenides. III. Group VIA: trigonal prism materials". *Journal of Physics C: Solid State Physics* **5,** 759–778 (1972).

112. Joensen, P., Frindt, R. F. & Morrison, S. "Single-layer MoS_2". *Materials Research Bulletin* **21,** 457–461 (1986).

113. Ribeiro-Soares, J., Almeida, R. M., Barros, E. B., Araujo, P. T., Dresselhaus, M. S., Cançado, L. G. & Jorio, A. "Group theory analysis of phonons in two-dimensional transition metal dichalcogenides". *Physical Review B* **90,** 115438 (2014).

114. El Youbi, Z., Jung, S. W., Richter, C., Hricovini, K., Cacho, C. & Watson, M. D. "Fermiology and electron-phonon coupling in the 2H and 3R polytypes of NbS_2". *Physical Review B* **103,** 155105 (2021).

115. Reina, A., Jia, X., Ho, J., Nezich, D., Son, H., Bulovic, V., Dresselhaus, M. S. & Kong, J. "Large area, few-layer graphene films on arbitrary substrates by chemical vapor deposition". *Nano letters* **9,** 30–35 (2009).

116. Lee, Y.-H., Zhang, X.-Q., Zhang, W., Chang, M.-T., Lin, C.-T., Chang, K.-D., Yu, Y.-C., Wang, J. T.-W., Chang, C.-S., Li, L.-J. & Lin, T.-W. "Synthesis of large-area MoS_2 atomic layers with chemical vapor deposition". *Advanced Materials* **24,** 2320–2325 (2012).

117. Liu, K.-K., Zhang, W., Lee, Y.-H., Lin, Y.-C., Chang, M.-T., Su, C.-Y., Chang, C.-S., Li, H., Shi, Y., Zhang, H., Lai, C.-S. & Li, L.-J. "Growth of large-area and highly crystalline MoS_2 thin layers on insulating substrates". *Nano letters* **12,** 1538–1544 (2012).

118. Zhan, Y., Liu, Z., Najmaei, S., Ajayan, P. M. & Lou, J. "Large-area vapor-phase growth and characterization of MoS_2 atomic layers on a SiO_2 substrate". *Small* **8,** 966–971 (2012).

119. van der Zande, A. M., Huang, P. Y., Chenet, D. A., Berkelbach, T. C., You, Y., Lee, G.-H., Heinz, T. F., Reichman, D. R., Muller, D. A. & Hone, J. C. "Grains and grain boundaries in highly crystalline monolayer molybdenum disulphide". *Nature Materials* **12,** 554–561 (2013).

120. Dumcenco, D., Ovchinnikov, D., Marinov, K., Lazić, P., Gibertini, M., Marzari, N., Lopez Sanchez, O., Kung, Y.-C., Krasnozhon, D., Chen, M.-W., Bertolazzi, S., Gillet, P., Fontcuberta i Morral, A., Radenovic,

A. & Kis, A. "Large-Area Epitaxial Monolayer MoS_2". *ACS Nano* **9,** 4611–4620 (2015).

121. Najmaei, S., Liu, Z., Zhou, W., Zou, X., Shi, G., Lei, S., Yakobson, B. I., Idrobo, J.-C., Ajayan, P. M. & Lou, J. "Vapour phase growth and grain boundary structure of molybdenum disulphide atomic layers". *Nature Materials* **12,** 754–759 (2013).

122. Liu, H. J., Jiao, L., Xie, L., Yang, F., Chen, J. L., Ho, W. K., Gao, C. L., Jia, J. F., Cui, X. D. & Xie, M. H. "Molecular-beam epitaxy of monolayer and bilayer WSe_2 : a scanning tunneling microscopy/spectroscopy study and deduction of exciton binding energy". *2D Materials* **2,** 034004 (2015).

123. Zhang, Y. *et al.* "Direct observation of the transition from indirect to direct bandgap in atomically thin epitaxial $MoSe_2$". *Nature Nanotechnology* **9,** 111–115 (2014).

124. Coleman, J. N. *et al.* "Two-dimensional nanosheets produced by liquid exfoliation of layered materials". *Science (New York, N.Y.)* **331,** 568–571 (2011).

125. Smith, R. J., King, P. J., Lotya, M., Wirtz, C., Khan, U., De, S., O'Neill, A., Duesberg, G. S., Grunlan, J. C., Moriarty, G., Chen, J., Wang, J., Minett, A. I., Nicolosi, V. & Coleman, J. N. "Large-scale exfoliation of inorganic layered compounds in aqueous surfactant solutions". *Advanced Materials* **23,** 3944–3948 (2011).

126. Backes, C., Szydłowska, B. M., Harvey, A., Yuan, S., Vega-Mayoral, V., Davies, B. R., Zhao, P.-L., Hanlon, D., Santos, E. J. G., Katsnelson, M. I., Blau, W. J., Gadermaier, C. & Coleman, J. N. "Production of Highly Monolayer Enriched Dispersions of Liquid-Exfoliated Nanosheets by Liquid Cascade Centrifugation". *ACS Nano* **10,** 1589–1601 (2016).

127. Castro Neto, A. H., Guinea, F., Peres, N. M. R., Novoselov, K. S. & Geim, A. K. "The electronic properties of graphene". *Reviews of Modern Physics* **81,** 109–162 (2009).

128. Glazov, M. M. & Ivchenko, E. L. "Valley Orientation of Electrons and Excitons in Atomically Thin Transition Metal Dichalcogenide Monolayers (Brief Review)". *JETP Letters* **113,** 7–17 (2021).

129. Kohn, W. "Nobel Lecture: Electronic structure of matter—wave functions and density functionals". *Reviews of Modern Physics* **71,** 1253–1266 (1999).

130. Hohenberg, P. & Kohn, W. "Inhomogeneous Electron Gas". *Physical Review* **136,** B864–B871 (1964).

131. Kohn, W. & Sham, L. J. "Self-Consistent Equations Including Exchange and Correlation Effects". *Physical Review* **140,** A1133–A1138 (1965).

132. Splendiani, A., Sun, L., Zhang, Y., Li, T., Kim, J., Chim, C.-Y., Galli, G. & Wang, F. "Emerging photoluminescence in monolayer MoS_2". *Nano letters* **10,** 1271–1275 (2010).

133. Mak, K. F., Lee, C., Hone, J., Shan, J. & Heinz, T. F. "Atomically thin MoS_2: a new direct-gap semiconductor". *Physical review letters* **105,** 136805 (2010).

134. Li, T. & Galli, G. "Electronic Properties of MoS_2 Nanoparticles". *The Journal of Physical Chemistry C* **111,** 16192–16196 (2007).

135. Zhu, Z. Y., Cheng, Y. C. & Schwingenschlögl, U. "Giant spin-orbit-induced spin splitting in two-dimensional transition-metal dichalcogenide semiconductors". *Physical Review B* **84,** 153402 (2011).

136. Kormányos, A., Burkard, G., Gmitra, M., Fabian, J., Zólyomi, V., Drummond, N. D. & Fal'ko, V. "k · p theory for two-dimensional transition metal dichalcogenide semiconductors". *2D Materials* **2,** 022001 (2015).

137. Frenkel, J. "On the Transformation of light into Heat in Solids. I". *Physical Review* **37,** 17–44 (1931).

138. Wannier, G. H. "The Structure of Electronic Excitation Levels in Insulating Crystals". *Physical Review* **52,** 191–197 (1937).

139. Fox, M. *Optical properties of solids* 2nd ed. (Oxford and New York, 2010).

140. Yang, X. L., Guo, S. H., Chan, F. T., Wong, K. W. & Ching, W. Y. "Analytic solution of a two-dimensional hydrogen atom. I. Nonrelativistic theory". *Physical review. A, Atomic, molecular, and optical physics* **43,** 1186–1196 (1991).

141. Cheiwchanchamnangij, T. & Lambrecht, W. R. L. "Quasiparticle band structure calculation of monolayer, bilayer, and bulk MoS_2". *Physical Review B* **85,** 205302 (2012).

142. Qiu, D. Y., Da Jornada, F. H. & Louie, S. G. "Optical spectrum of MoS_2: many-body effects and diversity of exciton states". *Physical review letters* **111,** 216805 (2013).

143. He, K., Kumar, N., Zhao, L., Wang, Z., Mak, K. F., Zhao, H. & Shan, J. "Tightly bound excitons in monolayer WSe_2". *Physical review letters* **113,** 026803 (2014).

144. Wang, G., Marie, X., Gerber, I., Amand, T., Lagarde, D., Bouet, L., Vidal, M., Balocchi, A. & Urbaszek, B. "Giant Enhancement of the Optical Second-Harmonic Emission of WSe_2 Monolayers by Laser Excitation at Exciton Resonances". *Phys. Rev. Lett.* **114,** 097403 (2015).

145. Taniguchi, T. & Watanabe, K. “Synthesis of high-purity boron nitride single crystals under high pressure by using Ba–BN solvent”. *Journal of Crystal Growth* **303,** 525–529 (2007).

146. Ajayi, O. A., Ardelean, J. V., Shepard, G. D., Wang, J., Antony, A., Taniguchi, T., Watanabe, K., Heinz, T. F., Strauf, S., Zhu, X.-Y. & Hone, J. C. “Approaching the intrinsic photoluminescence linewidth in transition metal dichalcogenide monolayers”. *2D Materials* **4,** 031011 (2017).

147. Cadiz, F. *et al.* “Excitonic Linewidth Approaching the Homogeneous Limit in MoS_2 -Based van der Waals Heterostructures”. *Physical Review X* **7,** 021026 (2017).

148. Chow, C. M., Yu, H., Jones, A. M., Yan, J., Mandrus, D. G., Taniguchi, T., Watanabe, K., Yao, W. & Xu, X. “Unusual Exciton-Phonon Interactions at van der Waals Engineered Interfaces”. *Nano letters* **17,** 1194–1199 (2017).

149. Jin, C., Kim, J., Suh, J., Shi, Z., Chen, B., Fan, X., Kam, M., Watanabe, K., Taniguchi, T., Tongay, S., Zettl, A., Wu, J. & Wang, F. “Interlayer electron–phonon coupling in WSe_2/hBN heterostructures”. *Nature Physics* **13,** 127–131 (2017).

150. Manca, M., Glazov, M. M., Robert, C., Cadiz, F., Taniguchi, T., Watanabe, K., Courtade, E., Amand, T., Renucci, P., Marie, X., Wang, G. & Urbaszek, B. “Enabling valley selective exciton scattering in monolayer WSe_2 through upconversion”. *Nature Communications* **8,** 14927 (2017).

151. Tran, K., Singh, A., Seifert, J., Wang, Y., Hao, K., Huang, J.-K., Li, L.-J., Taniguchi, T., Watanabe, K. & Li, X. “Disorder-dependent valley properties in monolayer WSe_2”. *Physical Review B* **96,** 041302 (2017).

152. Wang, Z., Zhao, L., Mak, K. F. & Shan, J. "Probing the Spin-Polarized Electronic Band Structure in Monolayer Transition Metal Dichalcogenides by Optical Spectroscopy". *Nano letters* **17,** 740–746 (2017).

153. Wang, G., Chernikov, A., Glazov, M. M., Heinz, T. F., Marie, X., Amand, T. & Urbaszek, B. "Colloquium : Excitons in atomically thin transition metal dichalcogenides". *Reviews of Modern Physics* **90,** 021001 (2018).

154. Liu, G.-B., Di Xiao, Yao, Y., Xu, X. & Yao, W. "Electronic structures and theoretical modelling of two-dimensional group-VIB transition metal dichalcogenides". *Chemical Society Reviews* **44,** 2643–2663 (2015).

155. Mak, K. F. & Shan, J. "Photonics and optoelectronics of 2D semiconductor transition metal dichalcogenides". *Nature Photonics* **10,** 216–226 (2016).

156. Ross, J. S., Wu, S., Yu, H., Ghimire, N. J., Jones, A. M., Aivazian, G., Yan, J., Mandrus, D. G., Di Xiao, Yao, W. & Xu, X. "Electrical control of neutral and charged excitons in a monolayer semiconductor". *Nature Communications* **4,** 1474 (2013).

157. Molina-Sánchez, A., Sangalli, D., Hummer, K., Marini, A. & Wirtz, L. "Effect of spin-orbit interaction on the optical spectra of single-layer, double-layer, and bulk MoS_2". *Physical Review B* **88,** 045412 (2013).

158. Kośmider, K., González, J. W. & Fernández-Rossier, J. "Large spin splitting in the conduction band of transition metal dichalcogenide monolayers". *Physical Review B* **88,** 245436 (2013).

159. Zeng, H., Dai, J., Yao, W., Di Xiao & Cui, X. "Valley polarization in MoS_2 monolayers by optical pumping". *Nature Nanotechnology* **7,** 490–493 (2012).

160. Mak, K. F., He, K., Shan, J. & Heinz, T. F. "Control of valley polarization in monolayer MoS_2 by optical helicity". *Nature Nanotechnology* **7,** 494–498 (2012).

161. Di Xiao, Liu, G.-B., Feng, W., Xu, X. & Yao, W. "Coupled spin and valley physics in monolayers of MoS_2 and other group-VI dichalcogenides". *Physical review letters* **108,** 196802 (2012).

162. Glazov, M. M., Ivchenko, E. L., Wang, G., Amand, T., Marie, X., Urbaszek, B. & Liu, B. L. "Spin and valley dynamics of excitons in transition metal dichalcogenide monolayers". *physica status solidi (b)* **252,** 2349–2362 (2015).

163. Dery, H. & Song, Y. "Polarization analysis of excitons in monolayer and bilayer transition-metal dichalcogenides". *Physical Review B* **92,** 125431 (2015).

164. Qiu, D. Y., Cao, T. & Louie, S. G. "Nonanalyticity, Valley Quantum Phases, and Lightlike Exciton Dispersion in Monolayer Transition Metal Dichalcogenides: Theory and First-Principles Calculations". *Physical review letters* **115,** 176801 (2015).

165. Liu, G.-B., Shan, W.-Y., Yao, Y., Yao, W. & Di Xiao. "Three-band tight-binding model for monolayers of group-VIB transition metal dichalcogenides". *Physical Review B* **88,** 085433 (2013).

166. Echeverry, J. P., Urbaszek, B., Amand, T., Marie, X. & Gerber, I. C. "Splitting between bright and dark excitons in transition metal dichalcogenide monolayers". *Physical Review B* **93,** 121107 (2016).

167. Zhang, X.-X., You, Y., Zhao, S. Y. F. & Heinz, T. F. "Experimental Evidence for Dark Excitons in Monolayer WSe_2". *Physical review letters* **115,** 257403 (2015).

168. Withers, F. *et al.* "WSe_2 Light-Emitting Tunneling Transistors with Enhanced Brightness at Room Temperature". *Nano letters* **15,** 8223–8228 (2015).

169. Wang, G., Robert, C., Suslu, A., Chen, B., Yang, S., Alamdari, S., Gerber, I. C., Amand, T., Marie, X., Tongay, S. & Urbaszek, B. "Spin-orbit engineering in transition metal dichalcogenide alloy monolayers". *Nature Communications* **6,** 10110 (2015).

170. Arora, A., Koperski, M., Nogajewski, K., Marcus, J., Faugeras, C. & Potemski, M. "Excitonic resonances in thin films of WSe_2: from monolayer to bulk material". *Nanoscale* **7,** 10421–10429 (2015).

171. Molas, M. R., Faugeras, C., Slobodeniuk, A. O., Nogajewski, K., Bartos, M., Basko, D. M. & Potemski, M. "Brightening of dark excitons in monolayers of semiconducting transition metal dichalcogenides". *2D Materials* **4,** 021003 (2017).

172. Zhang, X.-X., Cao, T., Lu, Z., Lin, Y.-C., Zhang, F., Wang, Y., Li, Z., Hone, J. C., Robinson, J. A., Smirnov, D., Louie, S. G. & Heinz, T. F. "Magnetic brightening and control of dark excitons in monolayer WSe_2". *Nature Nanotechnology* **12,** 883–888 (2017).

173. Kapuściński, P., Delhomme, A., Vaclavkova, D., Slobodeniuk, A. O., Grzeszczyk, M., Bartos, M., Watanabe, K., Taniguchi, T., Faugeras, C. & Potemski, M. "Rydberg series of dark excitons and the conduction band spin-orbit splitting in monolayer WSe_2". *Communications Physics* **4,** 1–6 (2021).

174. Wang, G., Robert, C., Glazov, M. M., Cadiz, F., Courtade, E., Amand, T., Lagarde, D., Taniguchi, T., Watanabe, K., Urbaszek, B. & Marie, X. "In-Plane Propagation of Light in Transition Metal Dichalcogenide Monolayers: Optical Selection Rules". *Physical review letters* **119,** 047401 (2017).

175. Zhou, Y., Scuri, G., Wild, D. S., High, A. A., Dibos, A., Jauregui, L. A., Shu, C., de Greve, K., Pistunova, K., Joe, A. Y., Taniguchi, T., Watanabe, K., Kim, P., Lukin, M. D. & Park, H. "Probing dark excitons in

atomically thin semiconductors via near-field coupling to surface plasmon polaritons". *Nature Nanotechnology* **12,** 856–860 (2017).

176. Liu, E., van Baren, J., Lu, Z., Altaiary, M. M., Taniguchi, T., Watanabe, K., Smirnov, D. & Lui, C. H. "Gate Tunable Dark Trions in Monolayer WSe_2". *Physical review letters* **123,** 027401 (2019).

177. He, M., Rivera, P., van Tuan, D., Wilson, N. P., Yang, M., Taniguchi, T., Watanabe, K., Yan, J., Mandrus, D. G., Yu, H., Dery, H., Yao, W. & Xu, X. "Valley phonons and exciton complexes in a monolayer semiconductor". *Nature Communications* **11,** 618 (2020).

178. Zhang, Y., Tang, T.-T., Girit, C., Hao, Z., Martin, M. C., Zettl, A., Crommie, M. F., Shen, Y. R. & Wang, F. "Direct observation of a widely tunable bandgap in bilayer graphene". *Nature* **459,** 820–823 (2009).

179. Wang, Z., Chiu, Y.-H., Honz, K., Mak, K. F. & Shan, J. "Electrical Tuning of Interlayer Exciton Gases in WSe_2 Bilayers". *Nano letters* **18,** 137–143 (2018).

180. Shi, Q., Shih, E.-M., Rhodes, D., Kim, B., Barmak, K., Watanabe, K., Taniguchi, T., Papić, Z., Abanin, D. A., Hone, J. & Dean, C. R. "Bilayer WSe_2 as a natural platform for interlayer exciton condensates in the strong coupling limit". *Nature Nanotechnology* **17,** 577–582 (2022).

181. Lin, K.-Q., Ziegler, J. D., Semina, M. A., Mamedov, J. V., Watanabe, K., Taniguchi, T., Bange, S., Chernikov, A., Glazov, M. M. & Lupton, J. M. "High-lying valley-polarized trions in 2D semiconductors". *Nature Communications* **13,** 6980 (2022).

182. Poellmann, C., Steinleitner, P., Leierseder, U., Nagler, P., Plechinger, G., Porer, M., Bratschitsch, R., Schüller, C., Korn, T. & Huber, R. "Resonant internal quantum transitions and femtosecond radiative decay of excitons in monolayer WSe_2". *Nature Materials* **14,** 889–893 (2015).

183. Korn, T., Heydrich, S., Hirmer, M., Schmutzler, J. & Schüller, C. "Low-temperature photocarrier dynamics in monolayer MoS_2". *Applied Physics Letters* **99,** 102109 (2011).

184. Moody, G., Kavir Dass, C., Hao, K., Chen, C.-H., Li, L.-J., Singh, A., Tran, K., Clark, G., Xu, X., Berghäuser, G., Malic, E., Knorr, A. & Li, X. "Intrinsic homogeneous linewidth and broadening mechanisms of excitons in monolayer transition metal dichalcogenides". *Nature Communications* **6,** 8315 (2015).

185. Robert, C., Lagarde, D., Cadiz, F., Wang, G., Lassagne, B., Amand, T., Balocchi, A., Renucci, P., Tongay, S., Urbaszek, B. & Marie, X. "Exciton radiative lifetime in transition metal dichalcogenide monolayers". *Physical Review B* **93,** 205423 (2016).

186. Selig, M., Berghäuser, G., Raja, A., Nagler, P., Schüller, C., Heinz, T. F., Korn, T., Chernikov, A., Malic, E. & Knorr, A. "Excitonic linewidth and coherence lifetime in monolayer transition metal dichalcogenides". *Nature Communications* **7,** 13279 (2016).

187. Robert, C., Amand, T., Cadiz, F., Lagarde, D., Courtade, E., Manca, M., Taniguchi, T., Watanabe, K., Urbaszek, B. & Marie, X. "Fine structure and lifetime of dark excitons in transition metal dichalcogenide monolayers". *Physical Review B* **96,** 155423 (2017).

188. Jauregui, L. A. *et al.* "Electrical control of interlayer exciton dynamics in atomically thin heterostructures". *Science (New York, N.Y.)* **366,** 870–875 (2019).

189. Boyd, R. W. *Nonlinear optics* 3rd ed. (Amsterdam and Boston, 2008).

190. Lin, K.-Q., Bange, S. & Lupton, J. M. "Quantum interference in second-harmonic generation from monolayer WSe_2". *Nature Physics* **15,** 242–246 (2019).

191. Harris, S. E., Field, J. E. & Imamoglu, A. “Nonlinear optical processes using electromagnetically induced transparency”. *Physical review letters* **64,** 1107–1110 (1990).

192. Harris, S. E. “Electromagnetically Induced Transparency”. *Physics Today* **50,** 36–42 (1997).

193. Lukin, M. D. & Imamoğlu, A. “Controlling photons using electromagnetically induced transparency”. *Nature* **413,** 273–276 (2001).

194. Fleischhauer, M., Imamoglu, A. & Marangos, J. P. “Electromagnetically induced transparency: Optics in coherent media”. *Reviews of Modern Physics* **77,** 633–673 (2005).

195. Ham, B. S., Hemmer, P. R. & Shahriar, M. S. “Efficient electromagnetically induced transparency in a rare-earth doped crystal”. *Optics Communications* **144,** 227–230 (1997).

196. Wei, C. & Manson, N. B. “Observation of the dynamic Stark effect on electromagnetically induced transparency”. *Physical review. A, Atomic, molecular, and optical physics* **60,** 2540–2546 (1999).

197. Phillips, M. C., Wang, H., Rumyantsev, I., Kwong, N. H., Takayama, R. & Binder, R. “Electromagnetically induced transparency in semiconductors via biexciton coherence”. *Physical review letters* **91,** 183602 (2003).

198. Longdell, J. J., Fraval, E., Sellars, M. J. & Manson, N. B. “Stopped light with storage times greater than one second using electromagnetically induced transparency in a solid”. *Physical review letters* **95,** 063601 (2005).

199. Abdumalikov, A. A., Astafiev, O., Zagoskin, A. M., Pashkin, Y. A., Nakamura, Y. & Tsai, J. S. “Electromagnetically induced transparency on a single artificial atom”. *Physical review letters* **104,** 193601 (2010).

200. Lin, K.-Q., Martin, R., Bange, S. & Lupton, J. M. "Polymer Coatings Tune Electromagnetically Induced Transparency in Two-Dimensional Semiconductors". *ACS Photonics* **6,** 3115–3119 (2019).

201. Lin, K.-Q. *et al.* "Narrow-band high-lying excitons with negative-mass electrons in monolayer WSe_2". *Nature Communications* **12,** 5500 (2021).

202. Lin, K.-Q., Faria Junior, P. E., Bauer, J. M., Peng, B., Monserrat, B., Gmitra, M., Fabian, J., Bange, S. & Lupton, J. M. "Twist-angle engineering of excitonic quantum interference and optical nonlinearities in stacked 2D semiconductors". *Nature Communications* **12,** 1553 (2021).

203. Lin, K.-Q., Faria Junior, P. E., Hübner, R., Ziegler, J. D., Bauer, J. M., Buchner, F., Florian, M., Hofmann, F., Watanabe, K., Taniguchi, T., Fabian, J., Steinhoff, A., Chernikov, A., Bange, S. & Lupton, J. M. "Ultraviolet interlayer excitons in bilayer WSe_2". *Nature Nanotechnology* **19,** 196–201 (2024).

204. Taghizadeh, A. & Pedersen, T. G. "Nonlinear optical selection rules of excitons in monolayer transition metal dichalcogenides". *Physical Review B* **99,** 235433 (2019).

205. Lafeta, L., Corradi, A., Zhang, T., Kahn, E., Bilgin, I., Carvalho, B. R., Kar, S., Terrones, M. & Malard, L. M. "Second- and third-order optical susceptibilities across excitons states in 2D monolayer transition metal dichalcogenides". *2D Materials* **8,** 035010 (2021).

206. Autere, A., Jussila, H., Dai, Y., Wang, Y., Lipsanen, H. & Sun, Z. "Nonlinear Optics with 2D Layered Materials". *Advanced Materials* **30,** e1705963 (2018).

207. Liu, H., Li, Y., You, Y. S., Ghimire, S., Heinz, T. F. & Reis, D. A. "High-harmonic generation from an atomically thin semiconductor". *Nature Physics* **13,** 262–265 (2017).

208. You, J. W., Bongu, S. R., Bao, Q. & Panoiu, N. C. "Nonlinear optical properties and applications of 2D materials: theoretical and experimental aspects". *Nanophotonics* **8,** 63–97 (2019).

209. Yao, K., Yanev, E., Chuang, H.-J., Rosenberger, M. R., Xu, X., Darlington, T., McCreary, K. M., Hanbicki, A. T., Watanabe, K., Taniguchi, T., Jonker, B. T., Zhu, X., Basov, D. N., Hone, J. C. & Schuck, P. J. "Continuous Wave Sum Frequency Generation and Imaging of Monolayer and Heterobilayer Two-Dimensional Semiconductors". *ACS Nano* **14,** 708–714 (2020).

210. Autler, S. H. & Townes, C. H. "Stark Effect in Rapidly Varying Fields". *Physical Review* **100,** 703–722 (1955).

211. Fox, M. *Quantum optics. An introduction* (Oxford and New York, 2006).

212. Levanon, A., Dahan, A., Nagler, A., Lifshitz, E., Bahar, E., Mrejen, M. & Suchowski, H. "Pulse shaping of broadband adiabatic SHG from a Ti-sapphire oscillator". *Optics Letters* **42,** 2992–2995 (2017).

213. Meshulach, D. & Silberberg, Y. "Coherent quantum control of two-photon transitions by a femtosecond laser pulse". *Nature* **396,** 239–242 (1998).

214. Dudovich, N., Dayan, B., Gallagher, F. S. M. & Silberberg, Y. "Transform-Limited Pulses Are Not Optimal for Resonant Multiphoton Transitions". *Physical review letters* **86,** 47–50 (2001).

215. Nikogosyan, D. N. "Beta barium borate (BBO)". *Applied Physics A Solids and Surfaces* **52,** 359–368 (1991).

216. Demtröder, W. *Laserspektroskopie 1* (Berlin, Heidelberg, 2011).

217. Strickland, D. & Mourou, G. "Compression of amplified chirped optical pulses". *Optics Communications* **56,** 219–221 (1985).

218. Trebino, R. *Frequency-Resolved Optical Gating: The Measurement of Ultrashort Laser Pulses* (Boston, MA, 2000).

219. Newport. "Prism Compressor for Ultrashort Laser Pulses". *Application Note* **29,** 1–12 (2020).

220. Fork, R. L., Martinez, O. E. & Gordon, J. P. "Negative dispersion using pairs of prisms". *Optics letters* **9,** 150–152 (1984).

221. Lezama, I. G., Arora, A., Ubaldini, A., Barreteau, C., Giannini, E., Potemski, M. & Morpurgo, A. F. "Indirect-to-direct band gap crossover in few-layer $MoTe_2$". *Nano letters* **15,** 2336–2342 (2015).

222. Bauer, J. M., Chen, L., Wilhelm, P., Watanabe, K., Taniguchi, T., Bange, S., Lupton, J. M. & Lin, K.-Q. "Excitonic resonances control the temporal dynamics of nonlinear optical wave mixing in monolayer semiconductors". *Nature Photonics* **16,** 777–783 (2022).

223. Chen, Y.-H. *et al.* "Efficient light upconversion via resonant exciton-exciton annihilation of dark excitons in few-layer transition metal dichalcogenides". *Nature Communications* **16,** 2935 (2025).

224. Harris, S. E. "Lasers without inversion: Interference of lifetime-broadened resonances". *Physical review letters* **62,** 1033–1036 (1989).

225. Scully, M. O. & Fleischhauer, M. "Lasers without inversion". *Science* **263,** 337–338 (1994).

List of publications

1. Lin, K.-Q., Faria Junior, P. E., Hübner, R., Ziegler, J. D., Bauer, J. M., Buchner, F., Florian, M., Hofmann, F., Watanabe, K., Taniguchi, T., Fabian, J., Steinhoff, A., Chernikov, A., Bange, S. & Lupton, J. M. "Ultraviolet interlayer excitons in bilayer WSe_2". *Nature Nanotechnology* **19,** 196–201 (2024).

2. Bauer, J. M., Chen, L., Wilhelm, P., Watanabe, K., Taniguchi, T., Bange, S., Lupton, J. M. & Lin, K.-Q. "Excitonic resonances control the temporal dynamics of nonlinear optical wave mixing in monolayer semiconductors". *Nature Photonics* **16,** 777–783 (2022).

3. Bauriedl, L., Bäuml, C., Fuchs, L., Baumgartner, C., Paulik, N., Bauer, J. M., Lin, K.-Q., Lupton, J. M., Taniguchi, T., Watanabe, K., Strunk, C. & Paradiso, N. "Supercurrent diode effect and magnetochiral anisotropy in few-layer $NbSe_2$". *Nature Communications* **13,** 4266 (2022).

4. Lin, K.-Q., Faria Junior, P. E., Bauer, J. M., Peng, B., Monserrat, B., Gmitra, M., Fabian, J., Bange, S. & Lupton, J. M. "Twist-angle engineering of excitonic quantum interference and optical nonlinearities in stacked 2D semiconductors". *Nature Communications* **12,** 1553 (2021).

5. Lin, K.-Q., Holler, J., Bauer, J. M., Parzefall, P., Scheuck, M., Peng, B., Korn, T., Bange, S., Lupton, J. M. & Schüller, C. "Large-Scale

Mapping of Moiré Superlattices by Hyperspectral Raman Imaging". *Advanced Materials* **33,** e2008333 (2021).

6. Brem, S., Lin, K.-Q., Gillen, R., Bauer, J. M., Maultzsch, J., Lupton, J. M. & Malic, E. "Hybridized intervalley moiré excitons and flat bands in twisted WSe_2 bilayers". *Nanoscale* **12,** 11088–11094 (2020).

Words of gratitude

At last, I would like to thank following people for making this work possible over the last few years and contributed in making my journey a fun and memorable one:

My advisor, *John M. Lupton* for the possibility to work on this exciting topic, your continuous support and guidance throughout the project, and trusting me with great freedom in my work.

Kai-Qiang Lin for introducing me to the field of 2D materials and excitons, for numerous inspiring discussions, for your help with the experiments, handing over the setup, and unforgettable time in China.

Sebastian Bange for providing solutions. No matter the problem, you always had an idea how to fix it. Without you, the experiments in this complexity would not be possible. Thanks, for writing the simulations, used in this work, which of course are only numerical experiments, and for being my main theoretical support.

My TMDC partners *Philipp*, *Fabi* and *Philip*, for making our office a fun place to work (zero home office days), for many helpful discussions, the daily tea, help in the lab, and for being great friends.

My students *Daniel*, *Fabi*, *Lucia*, *Michl*, *Samuel*, for trusting my guidance, for your help in the lab, assistance in fabricating samples, your ideas, and for making work an enjoyable experience.

Philipp and *Lijue* for helping with rearranging the setup and providing

help with experiments.

Eva, *Felix*, *Sabi*, *Timo*, *Chris*, *Sonja* and the rest of the Lupton group for the great working atmosphere, sticking with me through the last years, coping with bad jokes, and all the fun we had together.

Philipp for helpful discussions, ultrafast proof-reading of the thesis, numberless runs, bike rides, eating sessions, and being the friend that will stick.

Andi, *Anna*, *Verena*, *Michi* for merging into our group, whenever fun was on the line.

My collegues in China, for the warm welcome, great time and showing me all the delicious food. Special thanks to *Luyao*, for being an excellent lab partner.

Sebastian Krug and *Eva Weiss*, for helping with technical and administrative issues, and always being there when needed.

Am aller wichtigsten meiner Familie, *Anni*, *Mama*, *Papa*, *Tona*, *Vroni*, für unbedingten Support in allen Lebenslagen, euer Vertrauen in mich und dass ihr immer für mich da seid, seit ich denken kann.